DETECTION OF MASS, GROWTH RATE, AND STIFFNESS OF SINGLE BREAST CANCER CELLS USING MICROMECHANICAL SENSORS

BY

ELISE ANNE CORBIN

DISSERTATION

Submitted in partial fulfillment of the requirements
for the degree of Doctor of Philosophy in Mechanical Engineering
in the Graduate College of the
University of Illinois at Urbana-Champaign, 2013

Urbana, Illinois

Doctoral Committee:

Professor William P. King, Chair
Professor Rashid Bashir, Director of Research
Associate Professor Amy J. Wagoner-Johnson
Associate Professor Supriya Prasanth
Associate Professor Hyunjoon Kong

Abstract

Cancer is an intricate disease that stems from a number of different mutations in a cell. These mutations often control the cellular growth and proliferation, a hallmark of cancer, and give rise to many altered biophysical properties. There exists a complex relationship between the behavior of a cell, its physical properties, and its surrounding environment. Knowledge gleaned from cellular biomechanics can lead to an improved understanding of disease progression and provide methods to target it. There are many studies that look at biophysical changes on a large population level, though there is much information that is lost by treating populations as homogeneous in properties and cell cycle phase. Biophysical studies on individual cells can link mechanics with function through coordination with the cell cycle, which is a fundamental physiological process that is crucial for understanding cellular physiology and metabolism. Development of more precise, reliable, and versatile measurement techniques will provide a greater understanding the physical properties of a cell and how they affect its behavior. Microelectromechanical systems (MEMS) technology can provide tools for manipulating, processing, and analyzing single cells, thus enabling detailed analyses of their biophysical properties.

Growth is a vital element of the cell cycle, and cell mass homeostasis ensures that the cell mass and cell cycle transitions are coordinately linked. An accurate measurement of growth throughout the cell cycle is fundamental to understanding mechanisms of cellular proliferation in cancer. Growth can be identified through many ways; however, cell mass has been unexplored until the recent development of cantilever-type MEMS devices for mass sensing through resonant frequency shift. Measuring the dependency of growth rate on cellular mass may help explain the coordination and regulation of the cell cycle. However, MEMS mass sensing devices still require further development and characterization in order to reliably investigate long-term cell growth over the duration of the cell cycle.

This dissertation focuses on the use of MEMS resonant pedestal sensors for measuring the mass and growth rate of single cancer cells. This work included characterization and improvement of the sensors to address current challenges in the measurement of long-term growth rate. The MEMS resonant pedestal sensors were first used to measure physical properties of biomaterials, including the micromechanical properties of hydrogels through verification of stiffness effect on mass measurements. Before studying live cells, modifications to the fabrication process were introduced to improve cell capture and retention. These include integration of an on-chip microfluidic system for delivery of fluids during mass measurements and the micro-patterning of sensor surfaces for select functionalization and passivation. These modifications enable long-term measurement of the changes in mass of normal and cancerous cells over time. This is the first investigation of the differences in growth rate between normal and cancer cells using MEMS resonant sensors.

to my family,

with love

Acknowledgments

"It always seems impossible until it's done." -Nelson Mandela

I know that he was not speaking about graduate school, but this quote represents my mentality throughout graduate school. This has been a long process which, when I look back, will make me proud. I will have no regrets because I gave it everything I had. No one will understand as clearly as I do what it took to get to this end.

I express my deepest gratitude to my advisors, Dr. William P. King and Dr. Rashid Bashir, for their guidance, support, and *patience*. Dr. King helped to inspire and encourage me throughout my Ph.D. studies and helped me choose a path that linked what I learned working in his lab with my broader interests by connecting me with Dr. Bashir.

I am also grateful to my committee members: Dr. Joon Kong, Dr. Amy Wagoner-Johnson, and Dr. Supriya Prasanth. They offered guidance and support and kindly accepted to review my dissertation.

Thanks to all of my group members for their guidance and special thanks to Dr. Jungchul Lee, Dr. Keunhan Park, Dr. Zhenting Dai, Dr. Patrick Fletcher, Dr. Larry Millet, Dr. Vincent Chan, and Dr. Brian Dorvel for their guidance. They helped me step back from problems to look at things in another light to sort through some of the more confusing data or challenging experimental issues. I am grateful to all my friends for their support and contributions to my work - and for providing lighter moments that helped to relieve the stress of graduate school.

One person in particular that I thank is someone who has been through so much with me, Curtis Johnson; he gave me the strength and courage to face my fears and the confidence to persist through these years.

Finally, I am especially grateful to my family for their eternal love and support. Thanks for being there, when I was losing faith in myself. And for enduring through this process with me, giving me confidence, and never losing your faith in me. Their care and support helped shape me into the person that I am today.

> **"Our deepest fear is not that we are inadequate. Our deepest fear is that we are powerful beyond measure. We ask ourselves, Who am I to be brilliant, gorgeous, talented, fabulous? Actually, who are you not to be? We were born to make manifest the glory of God that is within us. And as we let our own light shine, we unconsciously give other people permission to do the same." -Marianne Williamson**

Table of Contents

List of Tables

List of Figures

Chapter 1

Micromechanics of Cancer

1.1 Introduction

A complex relationship exists between the behavior of a cell and its physical properties. There is strong interest in understanding the mechanisms through which the physical properties of a cell influence growth, differentiation, cell cycle progression, and apoptosis. Nanobiomechanics, which is the measuring of material properties at the smallest length scale, is an emerging area of research that has the ability to evolve the study of human disease. This field has helped elucidate mechanisms of disease progression and provided additional tools in the fight against disease.

The body continuously makes abnormal cells and cancer is the uncontrolled proliferation of these abnormal cells. Cancer is the second largest cause of death in the United States of America (USA) with about 569,000 cancer deaths (23% of all deaths) in 2010, and is becoming more widespread with 1.52 million new diagnoses made in 2010 alone [1]. Figure 1.1 shows the top 5 leading causes of death in the USA. Early diagnosis increases the possibility of effective intervention; however, as the disease metastasizes, the treatment of the disease becomes significantly harder and the survival rate decreases dramatically. Metastases are the cause of 90% of human cancer deaths [2]. A more complete understanding of why certain cells cause cancer progression to metastasis can impact mortality and improve treatments for cancer patients.

Biophysical mechanical properties of cells, such as their mass and stiffness, are fundamental physiological properties and are regulated by environmental and genetic factors, which have implications in cell biology, tissue engineering, and the research of cancers and diseases [3–6]. Specifically, the mechanics of cellular growth and division are important for diagnostics and drug development, with the purpose of investigating and identifying drug targets to slow or stop the growth of cancer cells. However, the utilization of mechanical properties requires understanding of the cellular processes that drive them. In the case of cell growth, a key question is whether or not growth rate is a function of cell mass. The cell mass homeostasis ensures that the cell mass and cell cycle transitions are coordinately linked [7]. Any change in this homeostasis can lead to uncontrolled proliferation, a hallmark of cancer. Development of more precise, reliable, and versatile measurement techniques will provide significant benefits through a greater understanding of how the physical properties of a cell affect its behavior.

The ability to reliably investigate and understand these properties requires measurement devices that provide high sensitivity, high throughput, and adaptability to include multiple on-chip functionalities. Advances in microelectromechanical system (MEMS) technology offer the potential for single cells to be handled, manipulated and characterized. This has led to the development of cantilever array sensors, suspended micro-channel resonators, and pedestal array sensors for the purpose of measuring cell mass and growth rate. The work presented in this dissertation involves advances in MEMS technology to measure the biophysical properties of individual adherent cells. Being able to accurately measure the biophysical properties of cells will benefit efforts in cancer diagnosis and treatment, understanding cell-to-cell communication, and tissue engineering.

We have developed an improved MEMS resonator platform sensor that can be used to measure the biophysical properties of single adherent cells [8].

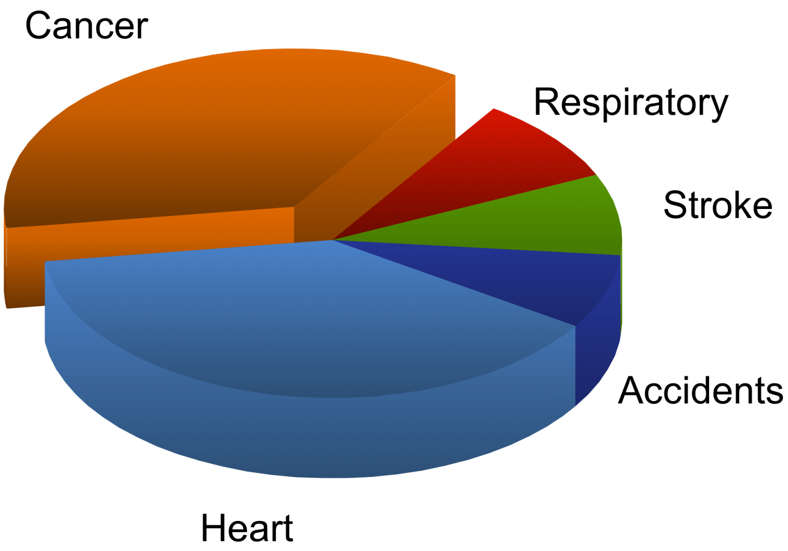

Figure 1.1: Top 5 Leading Causes of Death in the USA, where cancer is the second largest cause of death after Heart Disease. [Data from [9]]

1.2 Cell Mass and Growth Rate

Life begins with the cell and the cell is the fundamental element of growth. Growth is a normal part of life; however, growth rate is dependent on species. Although there is significant variation between individuals, the internal workings and organs of a person are proportional to the body. As organisms grow their size is maintained. Cell growth is the process of building mass to increase size. One of the great questions still to be understood is what regulates overall cell growth and coordination of growth with cell cycle progression.

For a cell to function properly, a cell must maintain homeostasis, or equilibrium state, over the cell cycle. This is the regulation of the internal system of the cell for proper function. Many diseases occur as a result of an imbalance of cell size homeostasis, which is linked to the coordination of the cell cycle [10].

The cell cycle is the period of time for cellular reproduction, including growth of the parent cell and its division into two daughter cells. Two distinct phases divide the cell cycle: interphase, the time period where the cell grows and acquires mass, and mitosis, the process where the cell divides. Interphase itself comprises three distinct segments: a gap, G1, where the cell grows in size, synthesis where DNA is replicated, and another gap, G2, for additional cell growth. Checkpoints exist after each gap to ensure the cell is prepared to enter either synthesis or mitosis [11, 12] .

1.2.1 Growth over the Cell Cycle

It is well-known that cell size distribution is maintained over many generations in culture; thus cells do not get increasingly larger or smaller [13]. However, over the course of a single cell cycle, a cell must grow to a particular size or mass prior to dividing. The question still remains: is there a pattern of cell mass increase and how does this vary from one division to the next? The fact that cells maintain size indicates some sort of coordination or link between cell growth and division. This link is unknown for most cells; however, one can speculate potential mechanisms. Figure 1.2 suggests four possible relationships between cell division and growth: growth influences cell division, cell division influences growth, growth and cell division rates are independent, and parallel coordination of growth and cell division [14].

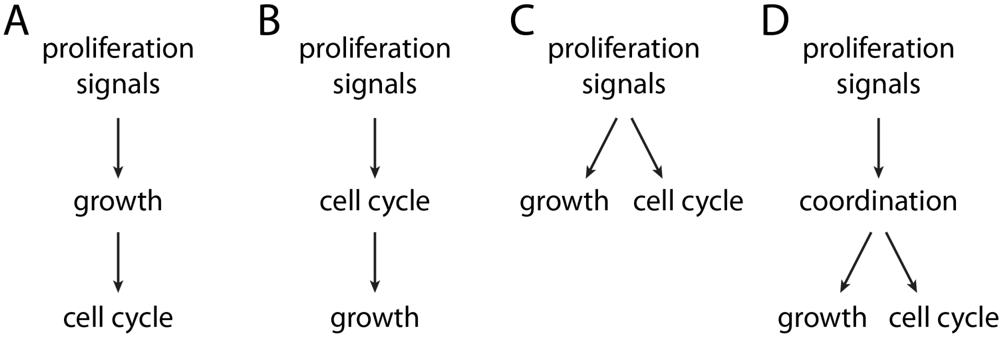

Figure 1.2: Four mechanisms between cell division and growth. (A) Cell division influences growth. (B) Growth influences cell division. (C) Growth and cell division are independent. (D) Parallel coordination of growth and cell division possibly controlled by a common upstream regulator. [Image adapted from [14]]

1.2.2 Growth Models

Much of the research on cell growth focuses on the temporal dynamics of growth rate. Variations in growth rate over the cell cycle may elucidate mechanisms underlying cell growth better than the magnitude of growth rate alone. There are two major models used to analyze the cell cycle: one based on an exponential increase and another based on a linear increase. Exponential growth rate for an individual cell is proportional to cell size mass, volume, or density during the cell cycle. Linear growth rate for an individual cell is constant meaning the cell increases size by the same amount regardless of its current size or state. Figure 1.3 presents examples of how cell mass would change in each of the two models. A biological basis proposed for each growth model that can help understand the mechanisms of cellular growth.

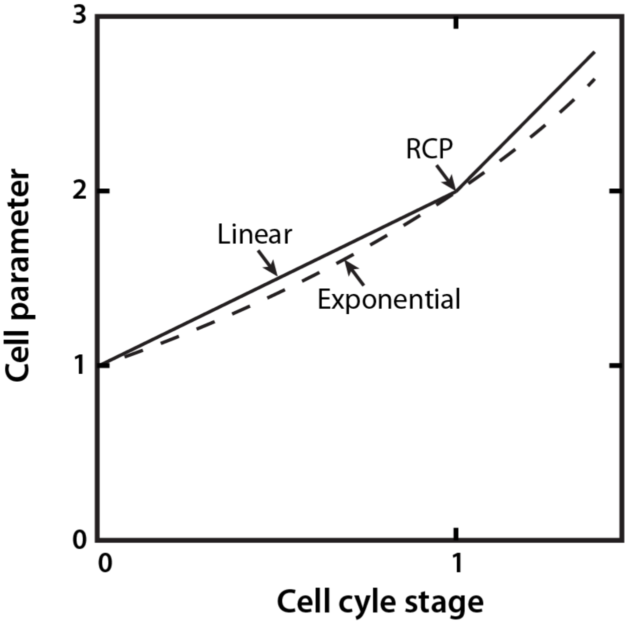

Figure 1.3: Exponential and linear models of growth. One daughter cell grows through the cell cycle and then divides to form two new daughter cells. As part of the linear growth curve there is a discontinuity in the curve called a rate change point (RCP). [Image adapted from [4]]

Protein synthesis a ribosomal mechanism that is essential for carrying out many catalytic functions in the body. The ribosome is a molecular machine that synthesizes proteins from amino acids through a translation process. The exponential growth rate is derived from the increasing amount of ribosomal machinery present in the cell that doubles along with size during the cell cycle. Since growth is dependent on the ribosomes, larger cells grow faster through more protein synthesis. However, cells should be in balanced growth where the bulk properties of cells remain unchanged for several generations, thus requiring additional cell size control mechanisms for cell size homeostasis over generations. If larger cells grow more rapidly than smaller ones, as in the exponential model, cell size variation in the population would increase in each generation. Because this does not occur, we know that if growth is exponential or, more generally, if it increases with cell size some mechanism must limit size variation in cells. Some cells, such as *Escherichia coli (E. coli)*, have been shown to exhibit an exponential growth rate [15].

The linear growth rate is limited by "gene dosage" or the amount of DNA available for transcription. Greater gene dosage can cause higher levels of gene product, if the gene is not subject to regulation from elsewhere in the body. In order to maintain homeostasis, cell size must double over the cycle, leading to an increase in growth rate and a discontinuity in the growth curve. This rate change point, or RCP, at the end of a cell division, shown in figure 1.3 [4]. It was shown by Conlon and Raff that rat Schwann cells, a variety of glial cell, do not require checkpoints to coordinate cell growth and cell cycle progression, leading to cells grow linearly [16]. The growth rate depends on the concentration of extracellular growth factors.

It is a complex problem to distinguish between different cell growth models with mathematical rigor. Distinguishing between exponential and linear growth would require highly precise measurements with a resolution of approximately 5% of the cell size, and equivalently high temporal sampling rate.

1.2.3 Limitations of Bulk Analysis

The earliest growth studies looked at the bulk growth of a population of cells, as opposed to a single cell. Bulk techniques for measuring cell growth are well-established and accepted methods, and are often chosen for their simplicity. Since a population of cells is studied in a single measurement, the inherent averaging of individual growth dynamics serves to reduce the effect of outliers, improving analysis. However, averaging is only appropriate for homogeneous populations of cells of uniform size that are synchronized in the cell cycle. Bulk studies of heterogeneous populations tend to obscure finer points of the growth dynamics, thus limiting their usefulness in many applications. Figure 1.4 shows an example of a time-dependent event within individual cells as well as the observed event when the entire population is measured. Its evident that the bulk technique can be misleading and interpreted as a gradual change; however, at the single-cell level the change is much faster but may be asynchronous through the population. Until recently, only bulk growth dynamics have been studied, since the investigation of single cells was not possible. However, the development of a number of mass measurement devices with high sensitivity has made the investigation of single cells possible. These technologies have begun to allow for the analysis of individual cells to better understand the coupling of growth dynamics with the cell cycle.

1.2.4 Volumetric Analysis

The most common method for investigating the growth of a single cell is by measuring its size or volume, often with a Coulter counter, a common and convenient device for counting and sizing particles in a suspension. As particles suspended in a conducting fluid pass through a Coulter counter the resistance between the electrodes changes and can be recorded. The amplitude of the recorded signal is directly proportional to the volume of the particle, though careful calibration is needed to accurately calculate volume from the signal [18].

Tzur *et al.* used a Coulter counter to measure mouse lymphocytic leukemia cells [7], and

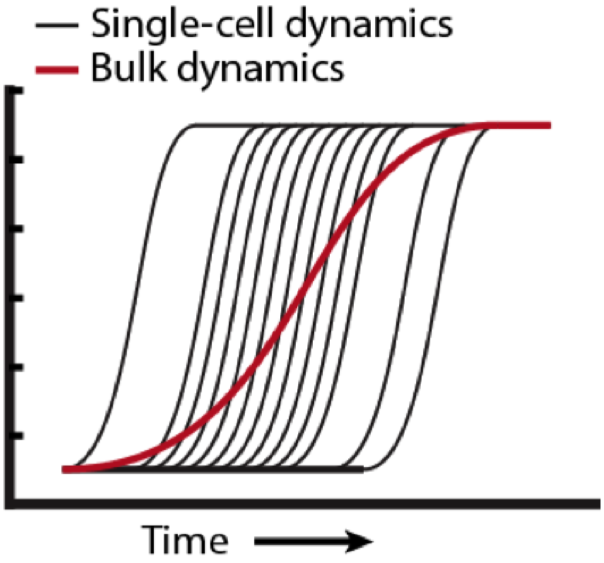

Figure 1.4: Example where the response of an individual cell can be misinterpreted by measuring the average value of a population of cell, or bulk dynamics. [Image adapted from [17]]

they found growth rate to be a function of cell size. For these cells there is an accelerative growth phase in G1, where the exponential rate constant is itself time-dependent. Following G1 there was a period of stable exponential growth during the rest of the cell cycle. These results indicate that the growth function across the cell cycle is neither a simple exponential nor a linear function, and it is size-dependent. Therefore, mammalian cells must possess a cell-autonomous intrinsic size regulator that couples cell growth to the cell cycle.

There are other methods that exist to measure the volume or size of a cell [15], though most are based on some form of optical microscopy. In 1932, Bayne-Jones and Adloph used optical measurements to capture the cell size growth of baker's yeast *Saccharomyces cerevisiae*. They measured the change in length, width, and total volume of yeast, and the growth formed an S-shaped curve in each generation [19]. Bayne-Jones and Adloph showed that the rate of growth of individual yeast cells ceases and resumes with the formation of each new bud, thus relating size increment to reproduction [19]. This observation is mirrored in a recent optical study of yeast volume, which showed growth rate as highly dependent on cell cycle phase [20]. They measured the relative rate of growth by aligning individual cells based on budding time and looking at the slope of the curve.

Advances in microscopy have led to another optical imaging technique called spatial light interference microscopy (SLIM) [15, 21, 22]. SLIM provides high spatial resolution and quantitative information by combining phase contrast microscopy with holography. Image contrast reflects the difference in refractive index of the material and the surroundings, which in turn can provide density. By assuming the refractive index of protein, Mir *et al.* illustrates the differences in dry mass growth rate among the G1, S, and G2 phases of the cell cycle of *E. coli*. They showed that *E. coli*, exhibit a mass-dependent growth rate that is approximately linear during G2, thus indicating an exponential growth pattern. This is also evidence that interactions of cells in culture play a role in individual cell growth.

Though volumetric analysis is an attractive option for measuring cell growth, volume itself is not the sole measure of cell size. The cell is a composite of many elements, including lipids, proteins, nucleic acids, cytoplasm, and other molecules. The components of a cell are altered during cell growth, though not necessarily in the same fashion or at the same time. With the composition of a cell constantly in flux, the material density changes, and volume alone may not a reliable measure for investigating cell growth over the cycle. Cell mass, on the other hand, will better reflect alterations in cellular composition, such as occurs in protein synthesis.

1.2.5 Direct Mass Measurement

One of the direct methods for measuring cell mass is the use of a microcantilever for mass sensing of a single cell. Microcantilevers were first introduced for use in atomic force microscopy (AFM) [23], but then since have been successfully applied to chemical and biological sensing applications [3, 24–26]. A microcantilever is an attractive idea for cell mass sensing in real time, owing largely to fast response times and the ability to operate in either liquid or gaseous environments. They also have extremely high mass sensitivity, and this sensitivity can be easily manipulated simply by modifying cantilever dimensions. Cantilever mass sensors operate on the principle of resonant frequency shift. The simple geometries of a cantilever make it easy to correlate the resonant frequency with an attached mass.

One solution to achieving the high sensitivity of a cantilever without damping effects of a surrounding fluid is to incorporate a microfluidic channel within a microcantilever structure, shown in figure 1.5. This device is referred to as a suspended microchannel resonator (SMR), which is a hollow microcantilever with an embedded fluidic microchannel. As individual cells travel through the microchannel of the device a shift in resonance frequency is observed, very similar to the traditional microcantilever operation. However, in the case of SMR, the cells are not adherent but suspended, requiring a control scheme to trap the cell from leaving the cantilever by constantly changing the direction of fluid flow. These sensors aim to measure the growth of single cells in terms of the buoyant mass, which is defined by the volume of the cell and the difference in density of the cell and the surrounding fluid. Manalis *et al.* have been able to trap small suspended cells for about 30 minutes at a time, though they have only been able to study bacteria and viruses due to size constraints [27–30].

Recently, a MEMS resonant mass sensor with four-beam springs and a large pedestal in the center has been designed to capture an adherent cell and overcomes the non-uniform mass sensitivity of the traditional cantilever beam. Park *et al.* were able to capture and measure human colon cancer (HT-29) cell mass and growth rate over 50+ hours with these sensors. Full details on sensor operation and mass measurement are presented in Chapter 2. These devices also detect mass through resonant shift, and are able to be operated in gaseous or aqueous environment. In order to overcome damping from surrounding fluid these devices must be driven magnetically to achieve a distinguishable resonance peak [8].

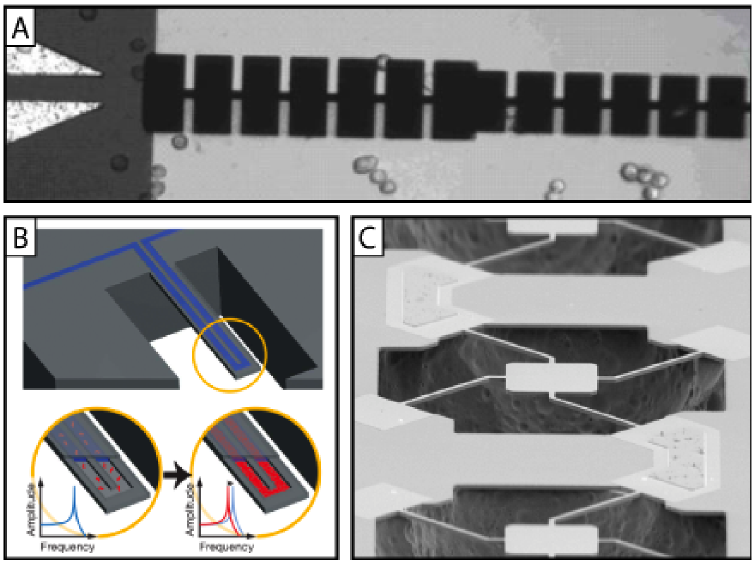

Figure 1.5: (A) Image of cantilever mass sensor array with dielectrophoresis (DEP) and fluid flow capabilities showing the capture of HeLa cells with positive DEP. [Image from [3]] (B) Schematic of the suspended microchannel resonator (SMR). The SMR has an embedded channel cross-sections for bacteria, yeast and mammalian L1210 mouse lymphoblasts.[Image from [27]] (C) Scanning electron micrograph (SEM) image of the pedestal resonant mass sensor, with four beam springs and a large pedestal region for cell capture. This design removes the non-uniformity of cantilevers.

1.3 Cell Biomechanics

1.3.1 Cellular Architecture

Cells can be classified into two main categories: prokaryotic and eukaryotic cells. A prokaryotic cell consists of a single compartment that is enclosed by a membrane, where the internal structure of the cell is simplistic with no defined nucleus, and are typical of bacteria, archaea, and other single-celled microorganisms. Human cells, on the other hand, are eukaryotic. Eukaryotic cells are far more complex systems involving a more well-defined internal structure with multiple subcellular components, including separate membrane bound nucleus and organelles, as seen in Figure 1.6. The nucleus is a major component of the cell containing the chromosomes and DNA that drive major metabolic activity such as gene transcription and replication [11]. Growth and progression through the cell cycle is regulated by the nucleus.

The material structure of the cell is largely defined by the cytoskeleton. The cytoskeleton acts as cellular scaffolding to prevent the plasma membrane from collapsing to its lowest energy system, a sphere. However, the cytoskeleton has many other functional purposes including cellular locomotion, internal transport, cell-cell linkages, and cell-ECM linkages. The cytoskeleton is made up of three major types of filaments: actin microfilaments, microtubules, and intermediate filaments, all of which play a significant role in the mechanical properties of a cell [31–33]. The cell structure is also affected strongly by environmental factors such as substrate stiffness, which in turn change the functionality of the cell. Even small environmental modifications can affect the cellular function and regulation [11].

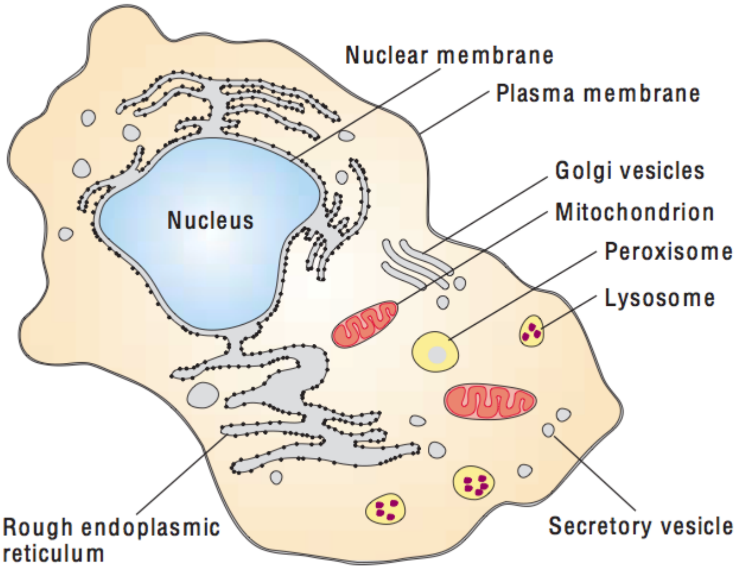

Figure 1.6: Schematic eukaryotic cell cross-section showing the membrane bound organelles and a segregated nucleus with a double bound membrane, contains the chromosomes and DNA. [Image from [11]]

1.3.2 Viscoelastic Properties of Cells

The structural and physical properties of cells allow the cell to withstand the physiological environment in which they live. Deviations from these properties will influence biological function and behavior, such as growth, differentiation, spreading, and migration as well as the structural health of the cell. Given these wide-ranging implications, quantification of these mechanical properties has been an active area of research. Continuum mechanics provides the basis of these measurements; therefore, the properties of the cell are expressed in terms of classical mechanics terms such as elastic modulus and shear modulus. There are various classical models to describe the properties of the cells; however, most models reflect that cells exhibit both fluid-like and solid-like behavior. When both behaviors are exhibited, this is described as viscoelasticity and includes a non-zero viscosity and a complex elastic modulus. Therefore, when a constant force or deformation is applied, the cell will either creep or relax over time. These properties affect the mechanical interactions.

Measuring the elastic modulus of the cell has been proven to be extremely challenging since the reported values vary over a few orders of magnitude. There are multiple factors that have to be considered to account for the cell being soft, thin, and submerged in fluid. Traditionally, mechanical models of materials are constructed by combining idealized springs and dashpot elements. These constitutive models can be experimentally used to describe the response of the cell based on experimental data. The basic models of viscoelasticity used to describe a cell are Maxwell, Kelvin-Voigt, and standard linear solid [34]. All of the models are defined by the response they give when a stress or strain is applied.

The Maxwell model consists of a spring and dashpot in series, shown in figure 1.7A. If the body is placed under a constant strain, the stress will gradually relax. However, if the body is placed under a constant stress, the strain has multiple components: (i) the instantaneous elastic component (referring to the spring) and (ii) the time-dependent viscous component that grows as long as the stress is applied. A limitation of the model is that it gives an inaccurate creep prediction [34].

Rearranging the Maxwell model generates the Kelvin-Voigt model, which consists of a spring and dashpot in parallel, shown in figure 1.7B. A Kelvin-Voigt body placed under a constant stress will deform at a decreasing rate approaching the steady-state strain. Once the constant stress is removed the material will gradually relax to the original shape. This

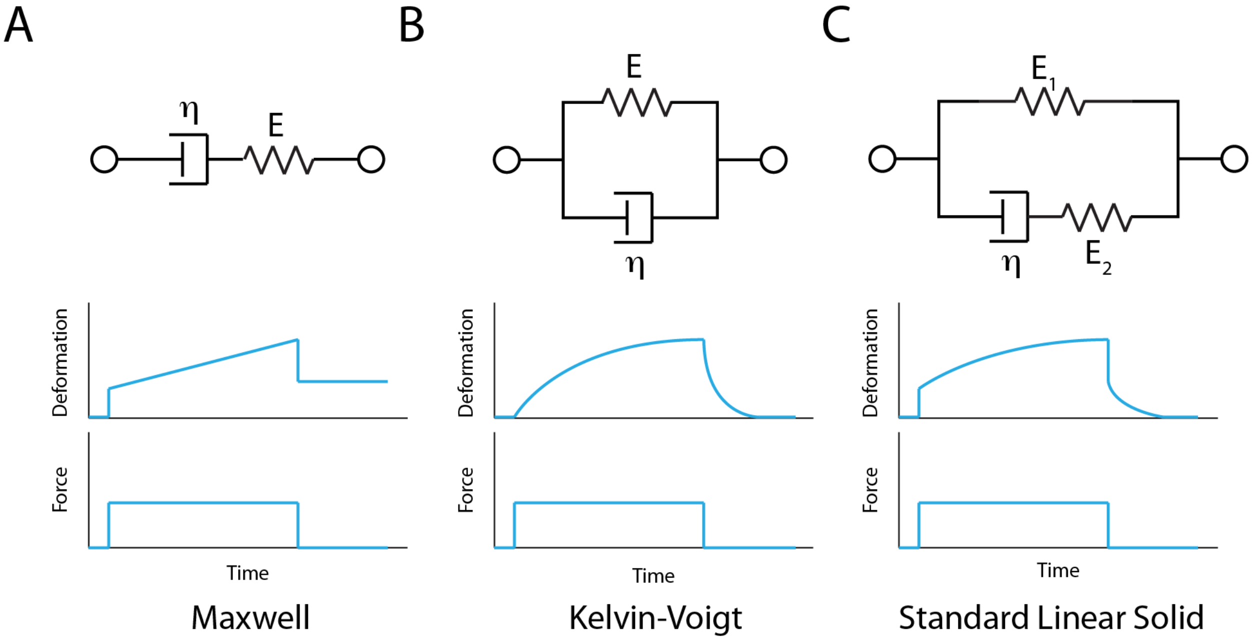

Figure 1.7: Schematics of generalized mechanical model analogies of linear viscoelastic behavior: (A) Maxwell, (B) Kelvin-Voigt, and (C) Standard Linear Solid [34].

model provides an accurate creep prediction of the strain, though it is much less accurate with relaxation [34].

The standard linear solid combines the concepts of both Maxwell and Kelvin-Voigt materials. In this model, a spring and one dashpot in series with a second spring in parallel, shown in figure 1.7C. Although the standard linear solid model is considered more accurate in predicting the proper response, it is more complicated to estimate all parameters [34].

1.3.3 Mechanical Measurement Techniques

In order to measure the mechanical properties of the cell, either a known force or a stress must be applied to the cell and the resulting deformation has to be accurately measured. Many methods have been developed for measuring cell mechanics, and there are a handful of methods that have been widely adopted. Figure 1.8 shows the most common techniques that have been used to probe cells, including micropipette aspiration, optical tweezers, magnetic twisting cytometry, and atomic force microscopy (AFM) [35–37].

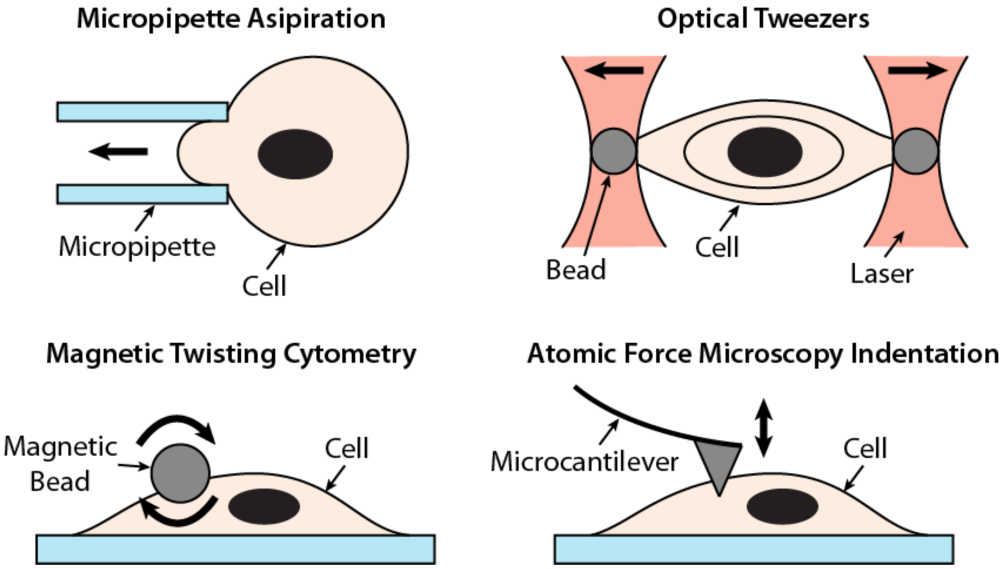

Figure 1.8: Experimental mechanical measurement techniques for measuring mechanical properties on the cellular level (A) micropipette aspiration (B) optical tweezers (C) magnetic twisting cytometry (D) atomic force microscopy indentation.

Micropipette aspiration works by applying a suction pressure to a cell in suspension by means of a glass micropipette, causing the cell to be slightly aspirated into the pipette (figure 1.8A). By measuring the length of aspiration, and comparing with the known suction force, cellular elastic properties can be determined. There have been many studiesusing micropipette aspiration performed on neutrophils, chondrocytes, endothelial cells and fibroblasts in suspension [38–48].

The optical tweezer device uses a focus laser beam to apply attractive or replusive forces to microscopic objects through the refractive index mismatch of the object and surrounding medium. This method traps and moves organelles or microbeads attached to or internalized by the cell at the focal point of the laser beam (figure 1.8B). By monitoring the deformation and applied force, the cell properties are calculated. Optical tweezers have been used extensively on many cell types, including human erythrocytes and red blood cells [49, 50].

Magnetic twisting cytometry uses ligand coated ferromagnetic microbeads to a apply small twisting forces to an adherent cell bound to the cell surface. Once the beads are attached to the cell, an oscillating magnetic field is applied causing the bead to twist or torque on the cell. By using a model of cell deformation you can estimate the cell elastic modulus of the cell through relationship between the applied torque and resulting bead rotation and translation(figure 1.8C) [51]. While this is a commonly used technology it is most appropriate for probing the cell cell membrane.

AFM has become one of the most frequently used tools for sensing and actuating on the nanometer scale and is a prominent tool in biological sciences for probing cells. The elastic modulus of cells and biological tissues are extracted through force-distance curves, where a microcantilever probe is pushed into the surface to a set force then is retracted (figure 1.8D). Typically, AFM techniques use a sharp tip; however, for soft materials or cells, a spherical tip is more commonly used because it allows for greater indentation without puncturing the cell membrane. Then a material model for tissue stiffness is used with Hertzian mechanics to fit the curve and extract the elastic modulus of the cell. There have been many studies using AFM to probe the stiffness of a wide variety of cells, biomolecules, and biomaterials [5, 52–55], and the methods will be more completely described in Chapter 2.

1.4 Cancer

1.4.1 Biological Characteristics of Cancer Cells

There are genetic changes in cancer that alter fundamental properties of cells, and some of these changes can be used to identify the disease [11, 12]. Cancer cells acquire a drive to proliferate that does not require an external growth signal. They fail to sense signals that restrict cell division and continue to live when they should die. They often change their attachment to surrounding cells or the extracellular matrix, breaking loose to divide more rapidly. A cancer cell may, up to a point, resemble a particular type of normal, rapidly dividing cell, but the cancer cell and its progeny will exhibit inappropriate immortality. To grow to more than a small size (generally 1-2 mm^3), tumors must obtain a blood supply, and they often do so by signaling to induce the growth of blood vessels into the tumor [56]. As cancer progresses, tumors become an abnormal organ, increasingly well-adapted to growth and invasion of surrounding tissues through metastasis. Figure 1.9 shows a schematic describing many of the known characteristics of cancer [11].

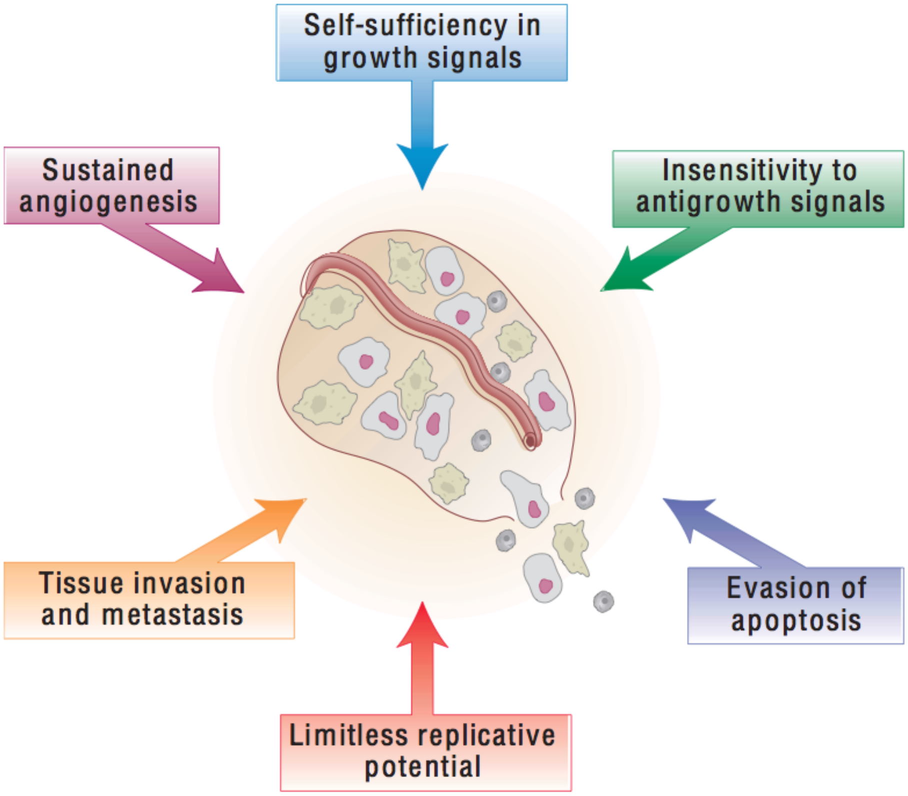

Figure 1.9: Overview of changes in cells that cause cancer. Cancer has six fundamental cellular hallmarks shown in this schematic. [Image from [11]]

Metastasis is a process that involves the spreading of cancer cells from a primary tumor to other sites in the body leading to the formation of new tumors at those sites [57]. This is a critical event in cancer, an figure 1.10 shows the basics process of metastasis [57]. From a primary vascularized tumor, a cell detaches, generally through a change in adhesion molecules. The detached cells then pass through the nearby tissue and enter the blood stream. These cells then pass through the vascular system, a few cells will eventually adhere to the vessel walls and exit the blood stream. Once the cells escape the blood stream they travel into the surrounding tissue and can begin to form a secondary tumor [57].

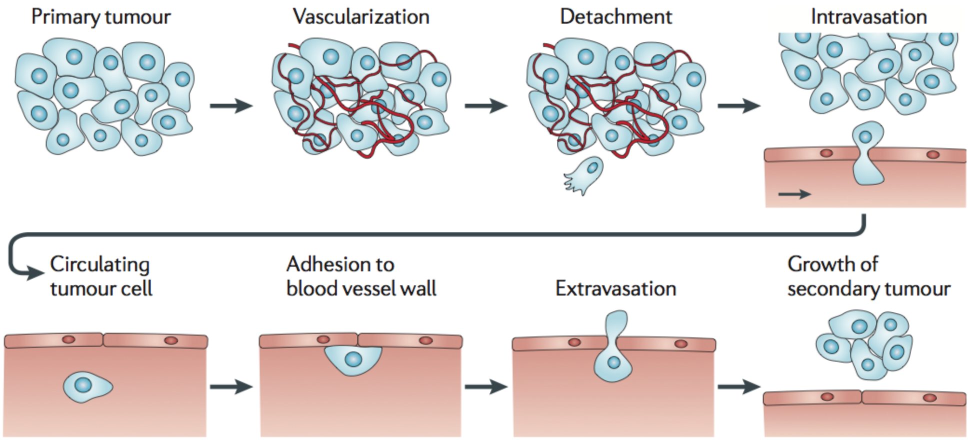

Figure 1.10: Overview of metastasis. Starting from the primary tumor, the tumor then with vascularize, then certain cells with detach and make there way into the blood stream, the cancer cell will then attach to the blood vessel wall generally close to a certain type of tissue, the cancer cell will make its way back out of the blood stream and begin to form a new tumor. [Image from [57]]

Many structural changes are observable in cancer cells as compared to normal cells. Although these changes can be used to characterize the type or stage of cancer, it is still difficult to determine the relationship between these different morphologies and malignant phenotype. Some of the detectable structural characteristics of cancer cells include cytoskeletal alterations, reduced cell adhesion, and nuclear shape changes. The biophysical properties of cancer cells, including cellular viscoelasticity, will reflect these structural differences and may provide additional information for detection and staging of cancer.

1.4.2 Growth and Proliferation in Metastasis

Cancer is caused by mutations that affect the cell circuitry including signaling patterns that control growth and the cell cycle progression [58]. Growth and division are highly regulated processes triggered by signaling; however, when the mechanism controlling these processes is faulty or damaged, as in cancer, growth and division can become unregulated.

An example of a signal pathway commonly damaged in cancer is the tumor suppressor protein 53 (p53). It has been shown extensively that the p53 gene, which regulates the cell cycle and prevents tumor generation, is damaged in many types of cancer. Damage to p53 removes the checkpoint in the cell cycle that promotes arrest in G1 and G2 when DNA damage is detected. The p53 G1 checkpoint ensures that damaged DNA is not replicated and passed on to daughter cells, while the G2 checkpoint prevents the cell from entering mitosis. Also, the p53 gene is the most common pro-apoptotic mechanism lost in human cancer, which leads to endless reproduction without death [2, 12, 59].

Another example of pathway damage in cancer is target of rapamycin (TOR). Figure 1.11 shows TOR as a central hub where growth factors and other signaling pathways converge to regulate cell growth. It has been shown that cell size can be used as an indirect measure of TOR activity, as cell size increases with TOR activity. It is known that the TOR pathway is upregulated in many human cancers, which aids in the increased growth and proliferation of cancer cells [60].

Growth characteristics are often used to describe the different grades of cancer. Grade 1 cancer cells grow slowly and give little symptoms that they are cancerous. Grade 2 cancer cells start to deviate from the norm in appearance and grow at a faster rate. Grade 3 cancer cells are in the final stage grow very rapidly. Other than fast growing cell being targeted by radiation therapy, there is no evidentiary support that cancers cells grow faster than normal cells. *In vitro* studies show that doubling times are actually longer for malignant cancer cells. Buehring and Williams showed that malignant breast cells divided more slowly than normal cells and population doubling time was more heterogeneous with malignant cells than normal cells [61]. However, further studies on the single cell level are needed to confirm this finding.

Investigating a single cancer cell and determining whether that cell has a shorter G1 and S, G2, or M remaining the same as a normal cell. If it is a shorter S phase, how would that impact the overall percent of cell cycle time?

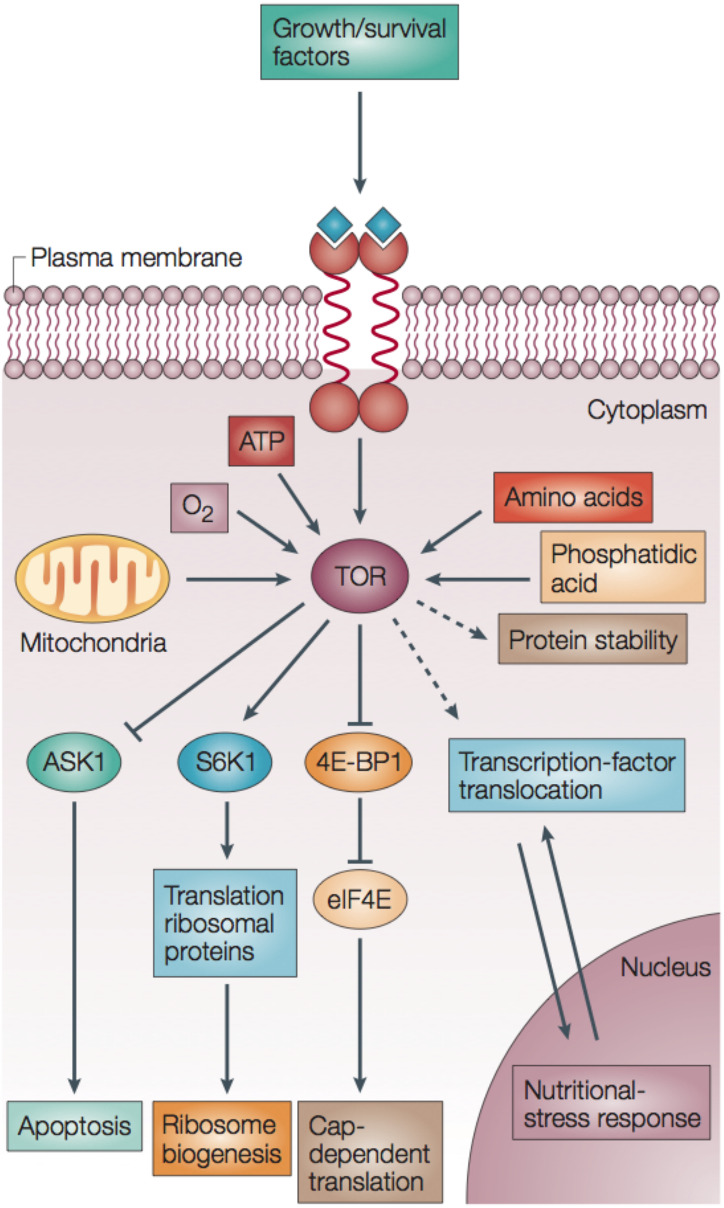

Figure 1.11: Target of rapamycin is a central regulator of cell growth and proliferation in response to environmental and nutritional conditions. [Image from [60]]

Some research groups have already begun to investigate cancer cell growth rates. Park *et al.* analyzed immortal human cervical cancer (HeLa) cells, using a microcantilever array sensor with the use of dielectrophoresis (DEP) to capture the cells on the surface of the cantilevers. They were able to measure the change in mass based on the frequency shift in two different cells: one with a mass of 1.01 ng and another with a mass of 3.57 ng. They also measured the cell volumes as 2349 μm^3 and 3857 μm^3 through imaging techniques, which equated to masses of 2.48 ng and 4.09 ng, assuming a density of $\approx 1.04 g/cm^3$ for HeLa cells that was found using a colloidal silica density gradient. These values are taken without regard to the changes in density over the cycle of the cell, which may explain the discrepancy between the measured mass and the estimated mass [3].

Park *et al.* also analyzed single human colon adenocarcinoma cells (HT-29) with a pedestal sensor and found that the average growth rate increases linearly and they grow on average 3.25% of mass every hour, which equates to a mass doubling time of about 22 hours [8]. Then they extended the analysis beyond single adherent cells per pedestal to incorporate sensors with multiples cells and found the mean population growth rate to be 3.98% per hour [8]. While this work helped to shed light on how cell mass increases in time, it also demonstrated one of the fundamental problems plaguing mass sensing that arises from multiple cells. As explained in a previous section you cannot extract a single cell event when you have captured multiple cells on the same sensor.

1.4.3 Mechanical Interaction with the Cellular Environment

As discussed earlier the cellular architecture of a cell plays a vital role in the "balance of forces" [62]. Studies have revealed that all living cells are in controlled mechanical tension through cytoskeletal filaments that both generate and resist mechanical loads or deformations. The cytoskeletal filaments will orient enzymes and substrates involved in biochemical reactions that mediate critical cellular functions. Thus, as a cell responds to a mechanical load its cytoskeletal structure is deformed, ultimately altering the chemical activity that modulates the cell behavior such as cell growth, differentiation, motility, and apoptosis. Therefore, cell stiffness, or how it responds physically to an external force is an indicator of cellular function.

A change in cell stiffness has been recently identified as a characteristic of cancer cells and an important parameter that affects the way they metastasize [5]. Cross *et al.* show that cancerous cells can be distinguished from normal ones even when they show similar shapes [5], since cancer cells are 1.4 to 1.8 times softer than the normal counterpart. Another study comparing different breast cell lines found similar results [52], and it has been shown that cell stiffness is a biomarker of the degree of metastatic potential.

Discher *et al.* have investigated how cell stiffness is influenced by the properties of the anchorage substrate [63]. Due to the large variability in solid stiffness, the behavior of cells on soft materials is a characteristic of phenotypes, specifically how cells grow on soft agar is a tool for cancer identification. Molecular pathways are influenced by adhesion and the feedback of the matrix stiffness on the cell state has important implications on growth, differentiation, and disease [63]. Tilghman *et al.* showed how cancer cell lines respond to polyacrylamide gels ranging in various stiffnesses [64]. They classified the findings into two categories: "rigidity dependent" and "rigidity independent," and measured the growth of these cells lines on stiffnesses ranging from 150 Pa to 4.8 kPa. This study begins to show that the stiffer matrices were more conducive to proliferation of cells, while showing overall that cancer proliferation is highly rigidity dependent [64]. This behavior is also seen in neuron growth. The experiment explored differential growth rates as a function of substrate stiffness, and found that growth is greatest when the axon stiffness is mechanically matched to the substrate (Figure 1.12) [65].

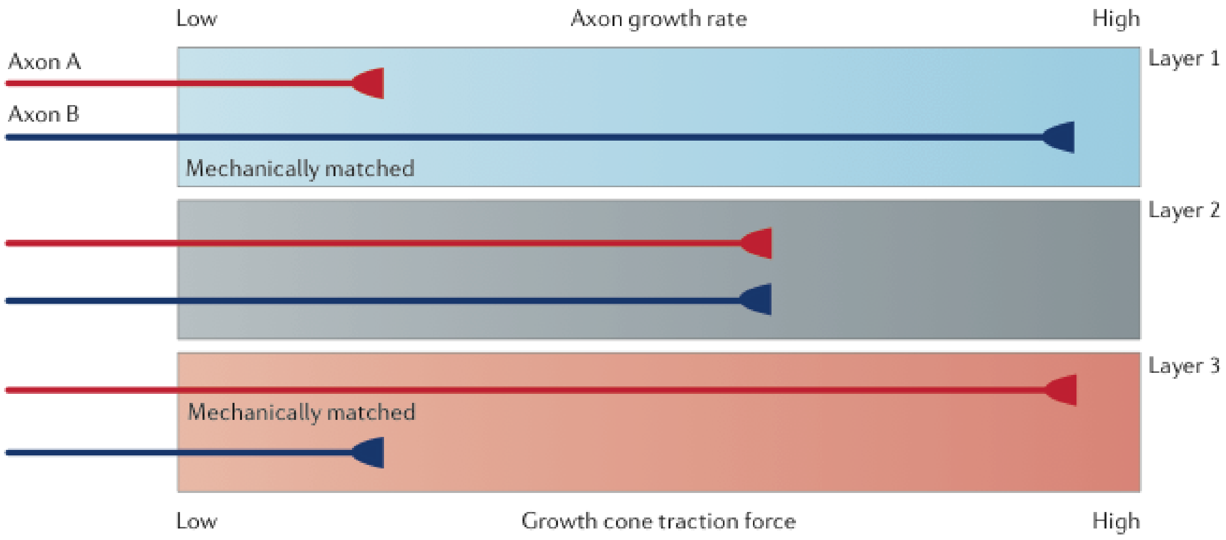

Figure 1.12: Functional implications of mechanical force transduction between synaptic compartments. [Image from [65]]

1.5 Dissertation Objectives

Previous studies have only been able to study aggregate populations of cells, making it impossible to determine patterns of individual cell growth. Using our sensors we have recently measured the cell mass and growth of adherent human colon cancer cells, showing that cell mass and growth can be measured for single cells. However, our previous work has shown that there are several technology limitations that inhibit application of microcantilever to mass measurement and analysis, including insufficient cell capture efficiency, media perfusion for long term growth, cell adhesion and cell movement/spreading. This work aims to address several issues that are introduced when measuring adherent cells through the use of new technological changes to the microcantilever sensors. The microcantilever pedestal sensors are designed, fabricated, characterized, and used to explore and investigate the biological question of whether cellular growth rate is dependent on the mass of the individual cell for cancer versus normal cells.

Chapter 2 focuses on the methods in cell micromechanics, with specific emphasis on the methods that we will consistently use throughout this thesis. First, I will review the principles of frequency shift in cantilever resonant sensors for mass measurements and how this relates to pedestal sensor. This includes the procedure for measuring the mass of a single cell. I then cover the necessary AFM for measuring the viscoelasticity of soft materials and cells. Here I review the models that can be used to extract the mechanical properties, as well as Hertzian contact mechanics for indentation experiments.

Chapter 3 focuses the use of resonant mass sensors for material characterization through the patterning of hydrogels on MEMS pedestal sensors. The mass and swelling of these hydrogel microstructures are characterized at a previously unavailable scale. The sensors are also used to measure the influence of fluids of similar and greater density on mass measurements to better understand sensor performance.

The hydrogel work is continued in Chapter 4 which focuses on the influence of cell stiffness on mass measurements. The elastic and viscous behavior of soft materials, including cells cause a shift in sensor resonant frequency. This chapter demonstrates the use of inverting a two-degree-of-freedom model of sensor and material dynamics to extract the stiffness of hydrogels on the microscale.

A modification of the current pedestal design is described in Chapter 5. The design replaces the "pit" underneath the sensor with a pore, or channel, on the back-side of the chip that can allow fluid flow. This will resolve some limitations of the current sensor array by measuring cell capture efficiency and an addition of a microfluidic chamber will add new functionality for delivering fluid to cells during the measurement. This microfluidic chamber is especially useful in studying neurons, which need specific growth factors, and I present some initial growth measurements.

Another major limitation of the sensor is being able to confine cells for long periods of time. Chapter 6 presents a technique for selective micro-patterning of proteins on the suspended pedestal sensor area through high-resolution photolithography. This is followed by a backfilling of pluronic, a tri-block co-polymer, for passivation of the chip surface to resist protein or cell adhesion. This enables the confinement of cells on the patterned collagen area on the resonant sensor for long-term growth measurements.

Chapter 7 presents initial measurements of the mass and growth rate of normal and cancer cells. The measurement of the growth dynamics of normal and cancer cells with varying degrees of metastasis, are compared withthe physical characteristics of benign versus malignant cells. This comparison will elucidate and provide new information on any difference in growth dynamics with metastatic potential of malignant cells.A change in cell stiffness has been recently identified as a characteristic of cancer cells and an important parameter that affects the way they metastasize. It is known that cancer cells are consistently softer than normal cells. Various cancer types display a common stiffness. Chapter 7 includes mechanical analysis of both cancerous and normal cells using atomic force microscopy through a technique similar to the one used to study hydrogels. Also, we measure the mass of fixed cells and compare the results with the mass of the same cells before fixation.

Finally, Chapter 8 concludes with a summary of the dissertation and a discussion of potential future research directions. There are still many improvements that can be made to this sensor and system, includes the addition of fluorescent labels as biomarkers to identify the different stages of the cell cycle to better elucidate the mechanisms of mass change more accurately and thoroughly through analysis. Another area considered is the use of the mass sensor for drug studies, such as the effect chemotherapeutics on mass growth rate. Finally, since it has been shown that a change in contact area drastically changes the mass reading there is there is an opportunity to study cell adhesion and how it is affected by the cell cycle.

1.6 References

[1] A. Jemal, R. Siegel, J. Xu, and E. Ward. Cancer Statistics, 2010. *CA: A Cancer Journal for Clinicians*, 60(5):277–300, 2010.

[2] P. Mehlen and A. Puisieux. Metastasis: a question of life or death. *Nature Reviews Cancer*, 6(6):449–458, 2006.

[3] K. Park, J. Jang, D. Irimia, J. Sturgis, J. Lee, J. P. Robinson, M. Toner, and R. Bashir. 'Living cantilever arrays' for characterization of mass of single live cells in fluids. *Lab On A Chip*, 8(7):1034–1041, 2008.

[4] J. M. Mitchison. Growth during the cell cycle. *International Review Cytology*, 226:165–258, 2003.

[5] S. E. Cross, Y. S. Jin, J. Rao, and J. K. Gimzewski. Nanomechanical analysis of cells from cancer patients. *Nature Nanotechnology*, 2(12):780–783, 2007.

[6] F. Chowdhury, S. Na, D. Li, Y. C. Poh, T. S. Tanaka, F. Wang, and N. Wang. Material properties of the cell dictate stress-induced spreading and differentiation in embryonic stem cells. *Nature Materials*, 9(1):82–88, 2010.

[7] A. Tzur, R. Kafri, V. S. LeBleu, G. Lahav, and M. W. Kirschner. Cell growth and size homeostasis in proliferating animal cells. *Science*, 325(5937):167–171, 2009.

[8] K. Park, L. J. Millet, N. Kim, H. Li, X. Jin, G. Popescu, N. R. Aluru, K. Hsia, and R. Bashir. Measurement of adherent cell mass and growth. *Proceedings of the National Academy of Sciences USA*, 107(48):20691–20696, 2010.

[9] M. Heron. Deaths: Leading causes for 2009. Technical report, Center for Disease Control, 2009.

[10] Z. Qu, W. R. MacLellan, and J. N. Weiss. Dynamics of the cell cycle: checkpoints, sizers, and timers. *Biophysical journal*, 85(6):3600–3611, 2003.

[11] H. Lodish, A. Berk, S. L. Zipursky, P. Matsudaira, D. Baltimore, and J. Darnell. *Molecular Cell Biology, 5th Edition.* Wiley Online Library, 2000.

[12] B. Alberts. *Essential Cell Biology: An introducton to the Molecular Biology of the Cell*, volume 2. Garland, 1997.

[13] S. Cooper. Control and maintenance of mammalian cell size. *BMC Cell Biology*, 5(1):35, 2004.

[14] P. Jorgensen and M. Tyers. How cells coordinate growth and division. *Current Biology*, 14(23):R1014–R1027, 2004.

[15] M. Mir, Z. Wang, Z. Shen, M. Bednarz, R. Bashir, I. Golding, S. G. Prasanth, and G. Popescu. Optical measurement of cycle-dependent cell growth. *Proceedings of the National Academy of Sciences USA*, 108(32):13124–13129, 2011.

[16] I. Conlon and M. Raff. Differences in the way a mammalian cell and yeast cells coordinate cell growth and cell-cycle progression. *Journal of Biology*, 2(1):7, 2003.

[17] D. D. Carlo and L. P. Lee. Dynamic single-cell analysis for quantitative biology. *Analytical Chemistry*, 78(23):7918–7925, 2006.

[18] A. K. Bryan, A. Engler, A. Gulati, and S. R. Manalis. Continuous and long-term volume measurements with a commercial coulter counter. *PLoS ONE*, 7, 2012.

[19] S. Bayne-Jones and E. F. Adolph. Growth in size of micro-organisms measured from motion pictures i. yeast, saccharomyces cerevisiae. *Journal of Cellular and Comparative Physiology*, 1(3):387–407, 1932.

[20] F. Ferrezuelo, N. Colomina, A. Palmisano, E. Garí, C. Gallego, A. Csikász-Nagy, and M. Aldea. The critical size is set at a single-cell level by growth rate to attain homeostasis and adaptation. *Nature Communications*, 3:1012, 2012.

[21] Z. Wang, L. Millet, M. Mir, H. Ding, S. Unarunotai, J. Rogers, M. U. Gillette, and G. Popescu. Spatial light interference microscopy (SLIM). *Optics Express*, 19(2):1016–1026, 2011.

[22] G. Popescu, Y. K. Park, N. Lue, C. Best-Popescu, L. Deflores, R. R. Dasari, M. S. Feld, and K. Badizadegan. Optical imaging of cell mass and growth dynamics. *American Journal of Physiology-Cell Physiology*, 295(2):C538–C544, 2008.

[23] G. Binnig, C. F. Quate, and C. Gerber. Atomic force microscope. *Physical Review Letters*, 56(9):930–933, 1986.

[24] R. Raiteri, G. Nelles, H. Butt, W. Knoll, and P. Skládal. Sensing of biological substances based on the bending of microfabricated cantilevers. *Sensors and Actuators B*, 61(1-3):213–217, 1999.

[25] J. Fritz, M. K. Baller, H. P. Lang, H. Rothuizen, P. Vettiger, E. Meyer, H. Güntherodt, C. Gerber, and J. K. Gimzewski. Translating biomolecular recognition into nanomechanics. *Science*, 288(5464):316–318, 2000.

[26] J. D. Adams, B. Rogers, L. Manning, Z. Hu, T. Thundat, H. Cavazos, and S. C. Minne. Piezoelectric self-sensing of adsorption-induced microcantilever bending. *Sensors and Actuators A: Physical*, 121(2):457–461, 2005.

[27] T. P. Burg, M. Godin, S. M. Knudsen, W. Shen, G. Carlson, J. S. Foster, K. Babcock, and S. R. Manalis. Weighing of biomolecules, single cells and single nanoparticles in fluid. *Nature*, 446(7139):1066–1069, 2007.

[28] Y. Weng, F. F. Delgado, S. Son, T. P. Burg, S. C. Wasserman, and S. R. Manalis. Mass sensors with mechanical traps for weighing single cells in different fluids. *Lab On A Chip*, 11(24):4174–4180, 2011.

[29] A. K. Bryan, A. Goranov, A. Amon, and S. R. Manalis. Measurement of mass, density, and volume during the cell cycle of yeast. *Proceedings of the National Academy of Sciences USA*, 107(3):999–1004, 2010.

[30] W. H. Grover, A. K. Bryan, M. Diez-Silva, S. Suresh, J. M. Higgins, and S. R. Manalis. Measuring single-cell density. *Proceedings of the National Academy of Sciences USA*, 108(27):10992–10996, 2011.

[31] D. E. Ingber. Tensegrity and mechanotransduction. *Journal of Bodywork and Movement Therapies, volume=12, number=3, pages=198–200, year=2008, publisher=Elsevier.*

[32] D. E. Ingber. Cellular mechanotransduction: putting all the pieces together again. *The FASEB journal*, 20(7):811–827, 2006.

[33] K. E. Kasza, A. C. Rowat, J. Liu, T. E. Angelini, C. P. Brangwynne, G. H. Koenderink, and D. A. Weitz. The cell as a material. *Current Opinion in Cell Biology*, 19(1):101–107, 2007.

[34] Y. C. Fung. *Biomechanics: Mechanical Properties of Living Tissues.* Springer-Verlag, New York City, NY, 1981.

[35] G. Y. H. Lee and C. T. Lim. Biomechanics approaches to studying human diseases. *Trends in biotechnology*, 25(3):111–118, 2007.

[36] C. T. Lim, E. H. Zhou, and S. T. Quek. Mechanical models for living cells - a review. *Journal of Biomechanics*, 39(2):195–216, 2006.

[37] C. T. Lim, E. H. Zhou, A. Li, S. R. K. Vedula, and H. X. Fu. Experimental techniques for single cell and single molecule biomechanics. *Materials Science and Engineering: C*, 26(8):1278–1288, 2006.

[38] G. W. Schmid-Schönbein, K. L. Sung, H. Tözeren, R. Skalak, and S. Chien. Passive mechanical properties of human leukocytes. *Biophysical Journal*, 36(1):243–256, 1981.

[39] E. Evans and B. Kukan. Passive material behavior of granulocytes based on large deformation and recovery after deformation tests. *Blood*, 64(5):1028–1035, 1984.

[40] E. Evans and A. Yeung. Apparent viscosity and cortical tension of blood granulocytes determined by micropipet aspiration. *Biophysical Journal*, 56(1):151–160, 1989.

[41] M. Sato, D. P. Theret, L. T. Wheeler, N. Ohshima, and R. M. Nerem. Application of the micropipette technique to the measurement of cultured porcine aortic endothelial cell viscoelastic properties. *Journal of Biomechanical Engineering*, 112(3):263, 1990.

[42] K. A. Ward, W. Li, S. Zimmer, and T. Davis. Viscoelastic properties of transformed cells: role in tumor cell progression and metastasis formation. *Biorheology*, 28(3-4):301, 1991.

[43] M. Sato, N. Ohshima, and R. M. Nerem. Viscoelastic properties of cultured porcine aortic endothelial cells exposed to shear stress. *Journal of Biomechanics*, 29(4):461–467, 1996.

[44] M. A. Tsai, R. S. Frank, and R. E. Waugh. Passive mechanical behavior of human neutrophils: power-law fluid. *Biophysical Journal*, 65(5):2078–2088, 1993.

[45] W. R. Trickey, G. M. Lee, and F. Guilak. Viscoelastic properties of chondrocytes from normal and osteoarthritic human cartilage. *Journal of Orthopaedic Research*, 18(6):891–898, 2000.

[46] W. R. Trickey, T. P. Vail, and F. Guilak. The role of the cytoskeleton in the viscoelastic properties of human articular chondrocytes. *Journal of Orthopaedic Research*, 22(1):131–139, 2006.

[47] O. Thoumine and A. Ott. Comparison of the mechanical properties of normal and transformed fibroblasts. *Biorheology*, 34(4):309–326, 1997.

[48] O. Thoumine, O. Cardoso, and J.J. Meister. Changes in the mechanical properties of fibroblasts during spreading: a micromanipulation study. *European Biophysics Journal*, 28(3):222–234, 1999.

[49] S. Henon, G. Lenormand, A. Richert, and F. Gallet. A new determination of the shear modulus of the human erythrocyte membrane using optical tweezers. *Biophysical Journal*, 76(2):1145–1151, 1999.

[50] K. Svoboda, C. F. Schmidt, D. Branton, and S. M. Block. Conformation and elasticity of the isolated red blood cell membrane skeleton. *Biophysical journal*, 63(3):784–793, 1992.

[51] N. Wang, J. P. Butler, and D. E. lngber. Mechanotransduction across the cell surface and through the cytoskeleton. *Science*, 260:21, 1993.

[52] Q. S. Li, G. Y. H. Lee, C. N. Ong, and C. T. Lim. AFM indentation study of breast cancer cells. *Biochemical and Biophysical Research Communications*, 374(4):609–613, 2008.

[53] T. G. Kuznetsova, M. N. Starodubtseva, N. I. Yegorenkov, S. A. Chizhik, and R. I. Zhdanov. Atomic force microscopy probing of cell elasticity. *Micron*, 38(8):824–833, 2007.

[54] N. E. Kurland, Z. Drira, and V. K. Yadavalli. Measurement of nanomechanical properties of biomolecules using atomic force microscopy. *Micron*, 43(2):116–128, 2012.

[55] A. M. Kloxin, C. J. Kloxin, C. N. Bowman, and K. S. Anseth. Mechanical properties of cellularly responsive hydrogels and their experimental determination. *Advanced Materials*, 22(31):3484–3494, 2010.

[56] S. R. McDougall, A. R. A. Anderson, and M. A. J. Chaplain. Mathematical modelling of dynamic adaptive tumour-induced angiogenesis: clinical implications and therapeutic targeting strategies. *Journal of Theoretical Biology*, 241(3):564–589, 2006.

[57] D. Wirtz, K. Konstantopoulos, and P. C. Searson. The physics of cancer: the role of physical interactions and mechanical forces in metastasis. *Nature Reviews Cancer*, 11(7):512–522, 2011.

[58] K. Collins, T. Jacks, and N. P. Pavletich. The cell cycle and cancer. *Proceedings of the National Academy of Sciences USA*, 94(7):2776–2778, 1997.

[59] S. Suresh. Biomechanics and biophysics of cancer cells. *Acta Materialia*, 55(12):3989–4014, 2007.

[60] M. A. Bjornsti and P. J. Houghton. The TOR pathway: a target for cancer therapy. *Nature Reviews Cancer*, 4(5):335–348, 2004.

[61] G. C. Buehring and R. R. Williams. Growth rates of normal and abnormal human mammary epithelia in cell culture. *Cancer Research*, 36(10):3742–3747, 1976.

[62] M. E. Chicurel, C. S. Chen, and D. E. Ingber. Cellular control lies in the balance of forces. *Current Opinion in Cell Biology*, 10(2):232–239, 1998.

[63] D. E. Discher, P. Janmey, and Y. Wang. Tissue cells feel and respond to the stiffness of their substrate. *Science*, 310(5751):1139–1143, 2005.

[64] R. W. Tilghman, C. R. Cowan, J. D. Mih, Y. Koryakina, D. Gioeli, J. K. Slack-Davis, B. R. Blackman, D. J. Tschumperlin, and J. T. Parsons. Matrix rigidity regulates cancer cell growth and cellular phenotype. *PLoS One*, 5(9):e12905, 2010.

[65] W. J. Tyler. The mechanobiology of brain function. *Nature Reviews Neuroscience*, 13(12):867–878, 2012.

Chapter 2

Methods in Cell Micromechanics

There are numerous techniques used to investigate the physical properties of cells on the microscale. This dissertation focuses on the use of micromechanical sensors to measure these properties, specifically mass and stiffness, and this chapter will review the principles behind the techniques employed and the measurement procedures. First, I review the principles of cantilever resonant sensors for cell mass measurements, and then discuss the specific experimental process and many important considerations for extracting mass from resonant frequency shift. I also present methods for extracting mechanical properties of cells with atomic force microscopy. The governing equations for determining elastic modulus and viscosity from microindentation with cantilever probes are also discussed. These methods allow for biophysical studies of individual cells, and will be used throughout this dissertation.

2.1 MEMS Resonant Mass Sensors

One device for directly measuring the mass of individual cells mass is the microcantilever [1–5]. Microcantilevers are most widely used in AFM due to the high sensitivity of their deflection to changes in force. Signal transduction in cantilever sensors operates in one of two ways: detection of static deformation or shift in resonant frequency [2, 6]. The use of microcantilevers for mass sensing has developed based on the idea of resonant frequency shift, since the resonant frequency is greatly affected by addition of mass at the free end of the cantilever. These devices are also advantageous as they can be operated in air or submerged in a liquid, which is necessary for studying biologics. These can further be fabricated in an array, as seen in Figure 2.1, to provide high measurement throughout. In the following sections I will describe the principles of resonant frequency shift, characteristics of the specific device used in this dissertation, and the method for estimating mass.

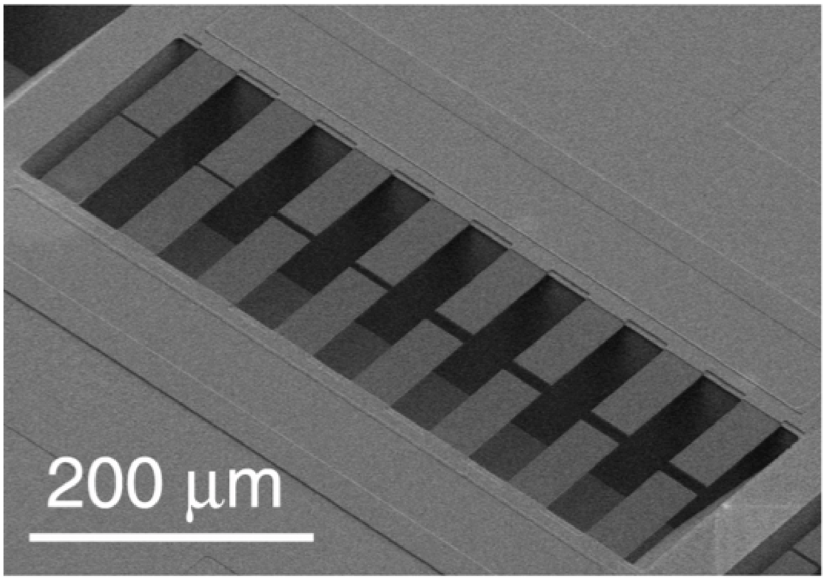

Figure 2.1: SEM image of cantilever arrays showing 120 µm × 100 µm cantilevers.

2.1.1 Frequency Shift Operation

The simple geometries of a cantilever make it easy to calculate the effective spring constant and device resonant frequency. In mass sensing, where an object of interest is adhered to the end of the device, the shift in the resonant frequency is used to extract the adhered mass. This is because the resonant frequency of the device is inversely proportional to the square root of the total mass. If the mass is placed directly on the free end of the cantilever the mass may be directly calculated from resonance frequency shift and the known spring constant of the device.

Figure 2.2 presents an example of measured resonant frequency and the shift when a mass is added. If the cantilever is represented through a lumped model with a mass, m,

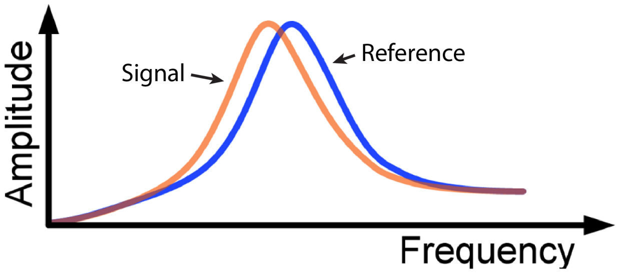

Figure 2.2: This is an example of the frequency response of a sensor. The peak on the right (blue) is the frequency data for the cantilever without a cell. After a cell is captured, the resonant frequency shifts to a lower frequency resulting in the peak on the left (orange). Comparing the frequency shift a mass can be extracted.

and is subjected to a harmonic excitation force, $Fe^{i\omega t}$, we can write the differential equation describing the cantilever deflection, y, in terms of time, t (equation (2.1)) [7].

$$m^* \frac{d^2y}{dt^2} + c\frac{dy}{dt} + ky = Fe^{i\omega t} \tag{2.1}$$

where $m^* = 0.24m$ is the effective mass, which accounts for the canitlever mass distribution; c is the damping coefficient; k is the spring constant; F is the amplitude of the excitiation; and ω is the angular frequency of the excitation [8]. This system has a resonant frequency, f_0, which is described by equation 2.2.

$$f_0 = 2\pi\omega_0 = \frac{1}{2\pi}\sqrt{\frac{k}{m^*}} \tag{2.2}$$

From equation 2.2, equation 2.3 can be derived to calculate the change in mass, Δm from a resonant frequency shift, Δf.

$$\Delta m = \frac{k}{4\pi^2}\left[\frac{1}{(f_0 + \Delta f)^2} - \frac{1}{f_0^2}\right] \tag{2.3}$$

Microcantilevers can have extremely high mass sensitivity, which makes them desirable for mass sensing, and this sensitivity can be easily manipulated simply by scaling down cantilever dimensions. Small changes in cantilever length and thickness lead to large differences in stiffness, and thus spring constant, as shown in equation 2.4. For a rectangular cantilever with length L, width w, thickness t, and Young's modulus E, the spring constant k of the device is evaluated as:

$$k = \frac{3EI}{L^3} = \frac{Ew}{4}\left(\frac{t}{L}\right)^3 \tag{2.4}$$

where $I = wt^3/12$ is the moment of inertia of the cross-section with respect to the bending axis. By combining and manipulating the above equations, it is possible to tune the response of the microcantilever for accurate sensing of cell mass of a single cell attached at the end of the cantilever.

Since the sensitivity of a microcantilever sensor is determined by minute changes in frequency, another important variable that needs to be considered is being able to resolve the frequency. This depends on the quality factor, Q, of the resonant peak. For mechanical systems the quality factor defines resonant peak and shape, and it is high influenced by the viscous damping. From equation 2.1 the quality factor is derived and shown in equation 2.5.

$$Q = \frac{\sqrt{km^*}}{c} \tag{2.5}$$

If you consider the case where a cantilever is transitioned from air to water, Q decreases with increased damping. This causes the width of the resonant peak to increase and makes accurate measurement more challenging. Increasing quality factor by making the resonant peak becomes narrower and sharper leads to higher measurement sensitivity from the ability to resolve smaller resonant frequency shifts. This can be achieved through modifications to device design, materials, and damping environment. However, this optimization often requires tradeoffs with other functionalities that must be appropriately considered.

2.1.2 Pedestal Sensor

Microcantilevers are attractive for mass sensing because of the potential for measurements with high sensitivity and high throughput. However, it is well-known that the cantilever beam structure has a non-uniform mass sensitivity and that calculation of mass depends strongly on placement of the object on the sensor. This is challenging in mass sensing of biological targets that must first be captured on the devices. Difficulty in estimating mass placement ultimately limits the accuracy of mass measurements made with the cantilever structure [1, 9]. To overcome this limitation, a MEMS resonant platform sensor has been designed to eliminate spatially dependent and non-uniform mass sensitivity [1], and can be used to measure the mass and long-term growth rate of single adherent cells.

A four beam-spring sensor structure, seen in Figure 2.3, was designed to minimize the variation of the displacement amplitude across the vibrating platform. The sensor is a square pedestal (60×60 µm^2) suspended over a 50 µm pit by four beams acting as springs ($l =$ 80 µm, $w = 4$ µm). This unique structure, through both modeling and experimental data, exhibited a maximum 4% difference in mass sensitivity at any position on the pedestal. Just like other cantilever sensors, it operates in a first resonance mode for mass sensing, which is a vertical displacement vibration with resonant frequencies of approximately 160 kHz in air and 60 kHz in liquid. One key concern when measuring cells is providing the proper micro-environment, which, for cells, means that the sensor must remain in liquid. This can provide problems of its own, because as you scale down, damping by liquid can drastically affect the resonant frequency measurement. Actuation in liquid also required a strong external force, and the sensor is actuated by passing an actuation current through the sensor in a static magnetic field to generate a Lorentz force [1, 10].

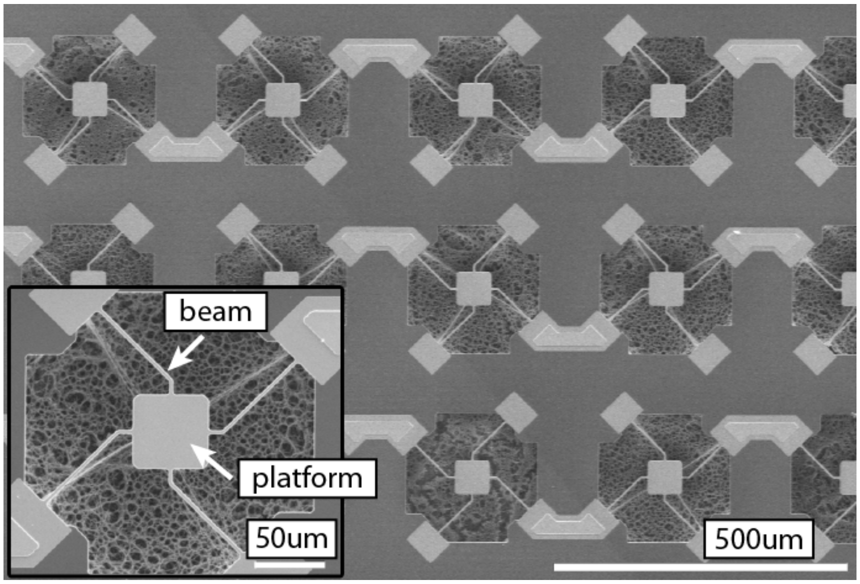

Figure 2.3: SEM images showing a sensor array, an individual sensor is shown in the inset. The beam springs and the platform area are also indicated. The uniform mass sensitivity area of the sensor is on the platform area, if a cell or mass is captured on one of the springs the mass measurement is no longer accurate.

2.1.3 Experimental Setup and Cell Mass Measurements

Figure 2.4 shows a laser Doppler vibrometer (LDV) system that, in conjunction with a feedback system and a lock-in amplifier, measures the velocity of the vibrating MEMS sensor platform to ultimately determine the resonant frequency of the device. This is achieved by monitoring the difference in phase between applied actuation current and sensor vibration. The excitation frequency is updated based on this phase until converging upon the resonant frequency. This procedure is used to estimate the resonant frequency of the devices in a series of different states to extract the mass of the adhered cell.

Specifically, three separate resonant frequency measurements are used in estimating the mass of an object: in air, in liquid, and in liquid with adhered load. The in-air measurement serves as a dry calibration of the empty resonator sensors to determine the effective spring constant of the device through the relationship in equation 2.6.

$$\omega = 2\pi f = \sqrt{\frac{k}{m}} \tag{2.6}$$

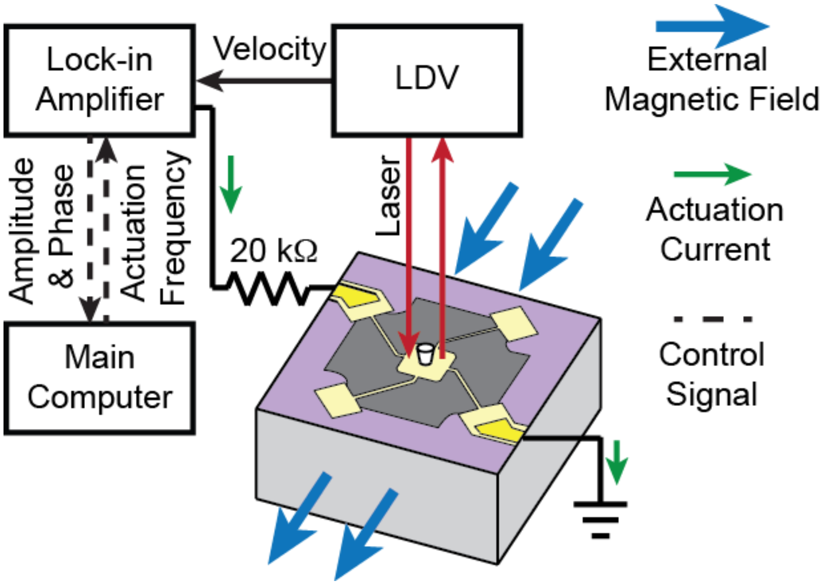

Figure 2.4: Overview of mass measurement with the sensor. Our measurement uses electromagnetic actuation and a laser Doppler vibrometer (LDV) system to measure the velocity of the vibrating platform in conjunction with a feedback loop and a lock-in amplifier to iteratively determine the resonant frequency.

The mass of each device, m, is known to be 110 ng due to high precision fabrication process. This generally yields a spring constant, k, of approximately 19.4 N/m. The spring constant calculated in equation 2.7 holds for both gaseous and aqueous environments,

$$k_{wet} = k_{dry} = m(2\pi f)^2 \tag{2.7}$$

where k_{wet} is the spring constant of the device in fluid and k_{dry} is the spring constant of the device in air.

The second resonant frequency is measured with the empty devices submerged in the surrounding fluid necessary for maintaining cell viability during the experiment. While the spring constant is unchanged, the location of the resonant peak is shifted to approximately 60 kHz. This shift is due to increased hydrodynamic loading on the sensor. The viscosity of the surrounding fluid results in an additional force opposing the vibration of the sensor, and appears as an added mass that decreases the resonant frequency. Since cell mass is also measured in liquid, this is the appropriate reference frequency.

Finally, cells are added to chip and allowed to settle and attach to the sensor platforms for at least two hours before measurement. This is so that the cells can properly adhere and reach the equilibrium temperature (37 °C). The resonant frequency the loaded sensor is now measured in the same fashion. The mass is the extracted from the shift in frequency relative to the in-liquid reference frequency. This extraction is described by equations 2.8, 2.9, and 2.10:

$$m_{platform} = \frac{k_{wet}}{(2\pi f_{wet_{empty}})^2} \tag{2.8}$$

$$m_{cell+platform} = \frac{k_{wet}}{(2\pi f_{wet})^2} \tag{2.9}$$

$$m_{cell} = m_{cell+platform} - m_{platform} = \frac{k_{wet}}{4\pi^2}\left(f_{wet}^{-2} - f_{wet_{empty}}^{-2}\right) \tag{2.10}$$

where $m_{platform}$ is the mass of the empty device, $m_{cell+platform}$ is the device mass and the cell mass together, m_{cell} is the mass of the cell, f_{wet} is the frequency of the platform and cell in fluid, $f_{wet_{empty}}$ is the reference frequency of the platform in fluid.

Mass measurements can be taken over time to observe how cells grow, however the apparent mass seen by empty sensors needs to be monitored as well. Over time the sensors exhibit a negative drift in resonant frequency of approximately 100-200 Hz/day. This drift is compensated for by simultaneously measuring empty neighboring sensors. Correcting for field drift effects in the apparent mass measurement involves estimating the equivalent mass change from field drift as measured by the empty sensors and subtracting from the cell mass measured from loaded sensors.

2.2 Microindentation with Atomic Force Microscopy

AFM is one of the most frequently used tools for sensing and actuating on the nanometer scale, and is widely adopted for mechanical property estimates through microindentation. The typical AFM system consists of a microcantilever probe with a sharp tip on the free end that is brought into contact with the surface. The high sensitivity of the cantilever deflection to applied force on the surface allows it to detect small variations in the surface topology. Figure 2.5 illustrates the working mechanism of AFM, which includes monitoring of both vertical position and cantilever deflection [11]. Typically, the scheme for determining the vertical deflection is optical through a laser reflected off the back of a microcantilever probe and into a set of position sensitive photodiodes. This sensitivity also makes it an excellent tool for microindentation and the probing of cells [12–16], DNA [17–19], bacteria [20–22], and biomolecules [23, 24]. Extracting mechanical properties from indentation data requires modeling of the material and the interaction with the cantilever, and the necessary equations are derived in the following sections.

2.2.1 Force-Distance Curves

Indentation measurements for extracting elastic modulus information with AFM uses force-distance curves to capture how the force that the cantilever tip applies to the surface leads to indentation. Force in AFM indentation is actually the deflection of the cantilever, which has been converted to applied force using the known spring constant of the device. This is plotted against the extension of the z-direction piezo that controls the position of the cantilever base [25]. The typical indentation experiment includes the approach of the cantilever, contact with the surface and indentation, and then retraction of the tip from the surface. These different steps are outlined in figure 2.6, which shows a schematic of how the force of the cantilever tip applied to the surface varies with distance.

Before extracting elastic modulus there are a number of pre-calibrations that must be

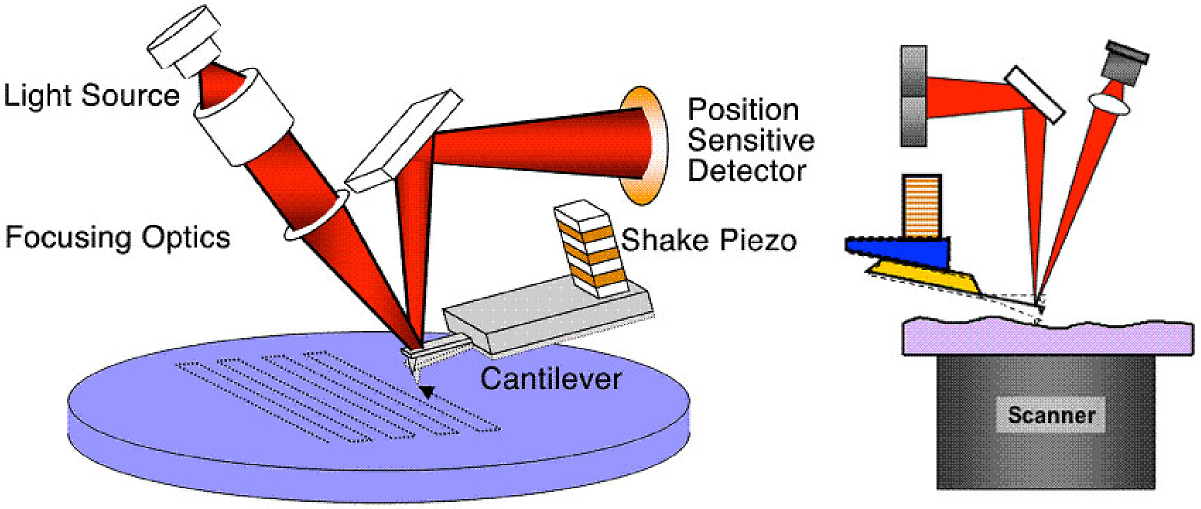

Figure 2.5: Schematic of the basic operation of the AFM. The cantilever is brought into contact with the surface and the xy motion stage traverses the probe across the surface. As the AFM cantilever probes the surface the tip follows the contours of the surface, the deflection of the cantilever is detected with a laser beam that is focused to beam to the head of the cantilever and refracts into a photodetecter. [Image from [11]]

taken into account. The spring constant of the cantilever must first be confirmed through calibration on a hard surface, generally quartz or silicon. A single indentation curve is taken and we can extract the slope of the deflection line in term of volts from the AFM that is then converted to nN/nm by calibrating the thermal vibrations of the cantilever probe. Once this is completed in the proper media force-distance curves may be acquired [25]. However, measurements in liquid require devices and experimental parameters that result in stable behavior of the cantilever. Devices that are too soft or media that is too viscous will result in forces on the device not reflective of the material of interest, especially if the approach velocity is too high.

Converting the force-distance curve into a stress-strain relationship requires modeling of how the cantilever tip geometry influences indentation. Typically, AFM techniques use a sharp tip, however, for soft materials or cells a spherical tip is more common. This allows for a more uniform deformation of the cell that results in a better representation of average

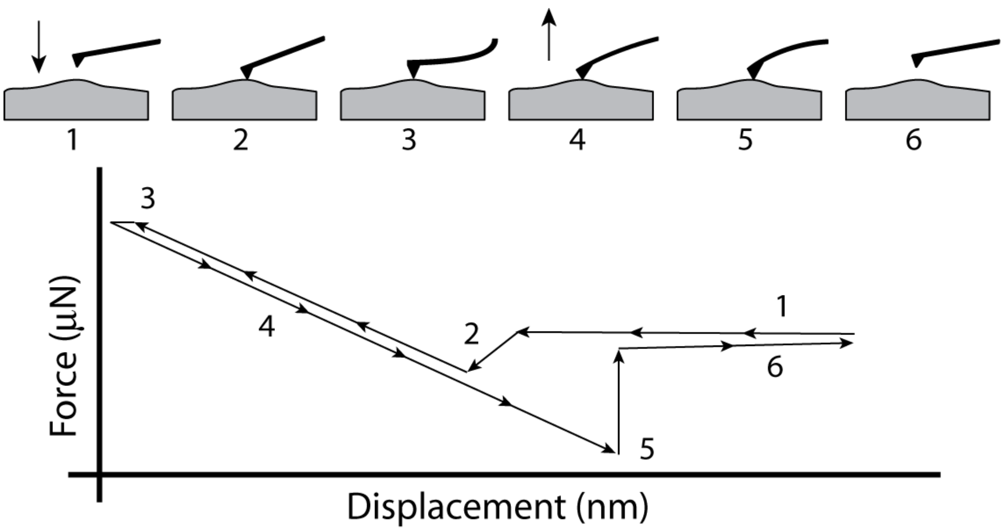

Figure 2.6: Schematic of a force-distance curve. Force-distance curves measures the mechanical interaction force between a tip and a sample one can observe a cycle as follows: (1) the tip is far away from the surface with no interaction with the surface. As the tip approaches the surface and comes into contact (1) to (2), the cantilever tip it enters the range of attractive surface forces and deflects downwards. From points (2) to (4): the tip is in contact with the surface and the cantilever pushes into the surface while the cantilever deflects upward. At point (4) the tip is retracting from the surface; however, the tip may remain in contact with the surface because of adhesion until the spring force of the cantilever overcomes the adhesion to the surface (5). The tip should then return to the initial position far away from the surface (6).[Image adapted from [26]]

material properties. Spherical tips will also not puncture the cell membrane. The spherical tip interaction is modeled through Hertzian contact mechanics to extract material properties from the force-distance curve.

2.2.2 Hertzian Contact Mechanics

Hertzian contact theory is derived from the classical mechanics problem of non-adhesive contacts. Specifically, Hertz solved the problem of the interaction between two curved elastic bodies of differing radii, which he later expanded to solve contact mechanics of other simple geometries. For this application we use the solution for contact between a sphere and a half-space (shown in figure 2.7), where R is the radius of the indenter probe and

d is the indentation displacement. This creates a contact area of radius, a, described by equation 2.11.

$$a = \sqrt{Rd} \tag{2.11}$$

This area can then be used to relate the applied force on the material can to the indentation displacement through equation 2.12.

$$F = \frac{4}{3} E_C R^{\frac{1}{2}} d^{\frac{3}{2}} \tag{2.12}$$

where F is the magnitude of the loading force and E_C is the effective elastic modulus of the material. However, this effective elastic modulus also includes the elastic properties of the spherical indenter, which must be separated from the elasticity of the sample material using equation 2.13.

$$\frac{1}{E_C} = \frac{1 - \nu_1^2}{E_1} + \frac{1 - \nu_2^2}{E_2} \tag{2.13}$$

where E_1 and E_2 are the elastic moduli of the surface and the spherical particle, and ν_1 and ν_2 are the Poisson ratios of the two materials. There are a number of parameters that need to be considered when determining the elastic modulus by AFM. Careful attention should be made to indentation velocity, data sampling rate, determination of contact point, and indentation depth [27]. Li et al. have shown the importance of considering the indentation velocity by varying the indentation velocity and showing the changes in the elastic modulus extraction [12]. Viscous material damping creates an opposing force relative to the indentation velocity and increases the apparent elastic modulus.

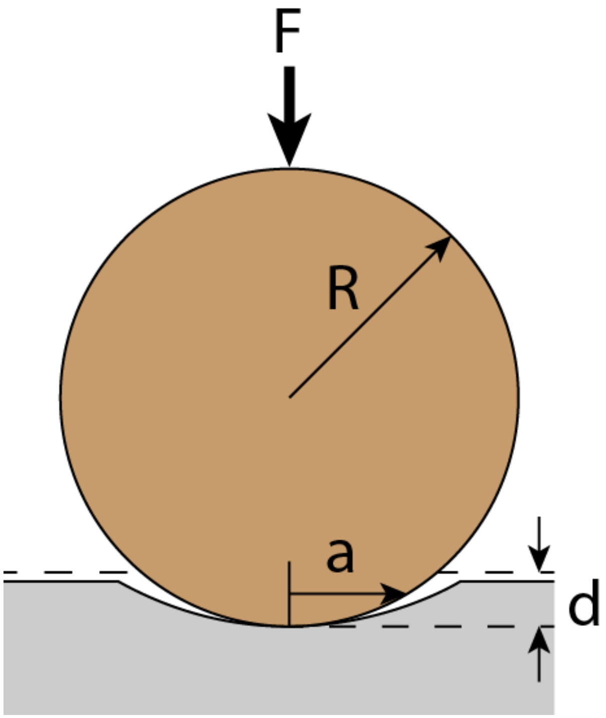

Figure 2.7: Schematic of a sphere on a flat surface following Hertz theory. The Hertzian contact theory can be used to find contact areas and indentation depths for simple geometries. F is the loading force, a is the contact radius, d is the penetration depth, and R is the radius of the sphere.

2.2.3 Viscoelastic Materials

Many biological materials, including cells, exhibit viscous behavior and have a non-zero damping component of their continuum mechanics model. Therefore, time dependent deformation behavior, such as creep or relaxation, must be accounted for when profiling the mechanical properties of a cell. Creep indentation measurements can also be taken with AFM using the same cantilever with spherical indenter tip as is used to estimate the elastic modulus. In this case, an instantaneous step load is applied to the cantilever probe, generating a strong material resistance from viscosity. The resulting force applied from the cantilever is then held constant through a feedback loop on the cantilever deflection, as shown in figure 2.8. While the force is held constant, the material continues to deform and the linear variable differential transformer (LVDT) signal of the AFM was monitored for ten

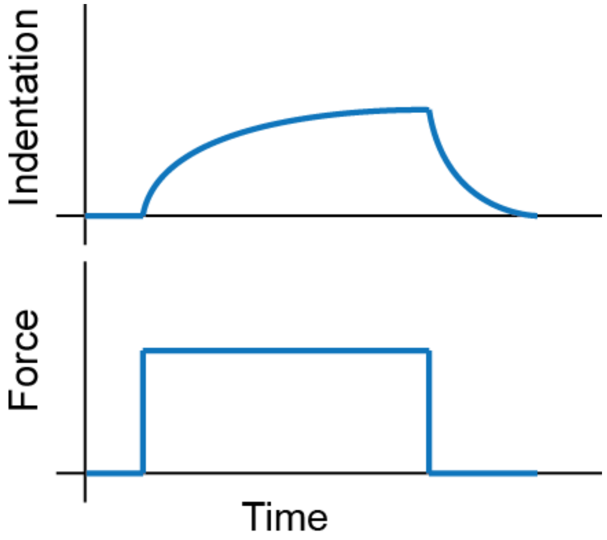

Figure 2.8: Applied step force and indentation as functions of time over a short period for a Kelvin-Voigt viscoelastic material. At a initial time, a viscoelastic material is loaded with a constant force that is maintained for a short period of time. The material responds to the set force by deforming that increases indentation until a set time when the force is released and the deformation relaxes back to its initial state.

seconds to collect a creep curve. Based on the Kelvin-Voigt model, we can derive the creep response in equation 2.14.

$$I(t) = \frac{F_0}{k}\left[1 - e^{-t\frac{k}{\eta}}\right] \tag{2.14}$$

where $I(t)$ is the indentation depth as a function of time t, defined as the difference between of the Z-sensor (LVDT) and cantilever deflection, which is held constant. F_0 is the magnitude of the loading force, k is the spring constant of the material, and η is the viscosity of the material. Finally, exponential fitting of the indentation curve returned the material viscosity.

2.3 References

[1] K. Park, L. J. Millet, N. Kim, H. Li, X. Jin, G. Popescu, N. R. Aluru, K. Hsia, and R. Bashir. Measurement of adherent cell mass and growth. *Proceedings of The National Academy of Sciences USA*, 107(48):20691–20696, 2010.

[2] K. Park, J. Jang, D. Irimia, J. Sturgis, J. Lee, J. P. Robinson, M. Toner, and R. Bashir.

‘Living cantilever arrays’ for characterization of mass of single live cells in fluids. *Lab On A Chip*, 8(7):1034–1041, 2008.

[3] Y. Weng, F. F. Delgado, S. Son, T. P. Burg, S. C. Wasserman, and S. R. Manalis. Mass sensors with mechanical traps for weighing single cells in different fluids. *Lab On A Chip*, 11(24):4174–4180, 2011.

[4] A. K. Bryan, A. Goranov, A. Amon, and S. R. Manalis. Measurement of mass, density, and volume during the cell cycle of yeast. *Proceedings of the National Academy of Sciences USA*, 107(3):999–1004, 2010.

[5] W. H. Grover, A. K. Bryan, M. Diez-Silva, S. Suresh, J. M. Higgins, and S. R. Manalis. Measuring single-cell density. *Proceedings of the National Academy of Sciences USA*, 108(27):10992–10996, 2011.

[6] N. V. Lavrik, M. J. Sepaniak, and P. G. Datskos. Cantilever transducers as a platform for chemical and biological sensors. *Review of Scientific Instruments*, 75(7):2229, 2004.

[7] W. T. Thompson and M. D. Dahleh. *Theory of Vibration with Applications: Prentice-Hall*. Englewood Cliffs, NJ, 5th ed. edition, 1998.

[8] G. Y. Chen, R. J. Warmack, T. Thundat, D. P. Allison, and A. Huang. Resonance response of scanning force microscopy cantilevers. *Review of Scientific Instruments*, 65(8):2532–2537, 1994.

[9] S. Dohn, R. Sandberg, W. Svendsen, and A. Boisen. Enhanced functionality of cantilever based mass sensors using higher modes. *Applied Physics Letters*, 86(23):233501, 2005.

[10] K. Park and R. Bashir. MEMS-based resonant sensor with uniform mass sensitivity. *15th International Conference on Solid-State Sensors, Actuators and Microsystems*.

[11] N. Geisse. AFM and combined optical techniques. Technical report, Asylum Research.

[12] Q. S. Li, G. Y. H. Lee, C. N. Ong, and C. T. Lim. AFM indentation study of breast cancer cells. *Biochemical and Biophysical Research Communications*, 374(4):609–613, 2008.

[13] J. L. Hutter, J. Chen, W. K. Wan, S. Uniyal, M. Leabu, and B. M. C. Chan. Atomic force microscopy investigation of the dependence of cellular elastic moduli on glutaraldehyde fixation. *Journal Of Microscopy-Oxford*, 219:61–68, 2005.

[14] W. Xu, R. Mezencev, B. Kim, L. Wang, J. McDonald, and T. Sulchek. Cell stiffness is a biomarker of the metastatic potential of ovarian cancer cells. *PloS one*, 7(10):e46609, 2012.

[15] S. E. Cross, Y. Jin, J. Rao, and J. K. Gimzewski. Nanomechanical analysis of cells from cancer patients. *Nature Nanotechnology*, 2(12):780–783, 2007.

[16] E. A-Hassan, W. F. Heinz, M. D. Antonik, N. P. DCosta, S. Nageswaran, C. Schoenenberger, and J. H. Hoh. Relative microelastic mapping of living cells by atomic force microscopy. *Biophysical Journal*, 74(3):1564–1578, 1998.

[17] H. G. Hansma, D. E. Laney, M. Bezanilla, R. L. Sinsheimer, and P. K. Hansma. Applications for atomic force microscopy of DNA. *Biophysical Journal*, 68(5):1672, 1995.

[18] H. G. Hansma, R. L. Sinsheimer, M. Li, and P. K. Hansma. Atomic force microscopy of single-and double-stranded dna. *Nucleic Acids Research*, 20(14):3585–3590, 1992.

[19] M. J. Allen, E. M. Bradbury, and R. Balhorn. Afm analysis of dna-protamine complexes bound to mica. *Nucleic Acids Research*, 25(11):2221–2226, 1997.

[20] M. J. Doktycz, C. J. Sullivan, P. R. Hoyt, D. A. Pelletier, S. Wu, and D. P. Allison. AFM imaging of bacteria in liquid media immobilized on gelatin coated mica surfaces. *Ultramicroscopy*, 97(1):209–216, 2003.

[21] V. Vadillo-Rodriguez, S. R. Schooling, and J. R. Dutcher. In situ characterization of differences in the viscoelastic response of individual Gram-negative and Gram-positive bacterial cells. *Journal of Bacteriology*, 191(17):5518–5525, 2009.

[22] V. Dupres, F. D. Menozzi, C. Locht, B. H. Clare, N. L. Abbott, S. Cuenot, C. Bompard, D. Raze, and Y. F. Dufrêne. Nanoscale mapping and functional analysis of individual adhesins on living bacteria. *Nature Methods*, 2(7):515–520, 2005.

[23] N. E. Kurland, Z. Drira, and V. K. Yadavalli. Measurement of nanomechanical properties of biomolecules using atomic force microscopy. *Micron*, 43(2):116–128, 2012.

[24] H. G. Hansma. Atomic force microscopy of biomolecules. *Journal of Vacuum Science & Technology B: Microelectronics and Nanometer Structures*, 14(2):1390–1394, 1996.

[25] B. Cappella and G. Dietler. Force-distance curves by atomic force microscopy. *Surface Science Reports*, 34(1-3):1–104, 1999.

[26] L. J. Harding, M. Reading, and D. Q. M. Craig. The development of heated tip force-distance measurements as a novel approach to site-specific characterization of pharmaceutical materials. *Journal of Pharmaceutical Sciences*, 97(7):2768–2779, 2008.

[27] A. J. Engler, F. Rehfeldt, S. Sen, and D. E. Discher. Microtissue elasticity: measurements by atomic force microscopy and its influence on cell differentiation. *Methods in Cell Biology*, 83:521–545, 2007.

Chapter 3

Characterization of Mass and Swelling of Hydrogel Microstructures using MEMS Resonant Mass Sensor Arrays

The use of hydrogels for biomedical engineering, and for the development of biologically inspired cellular systems at the microscale, is advancing at a rapid pace. Microelectromechanical system (MEMS) resonant mass sensors enable the mass measurement of a range of materials. The integration of hydrogels onto MEMS resonant mass sensors is demonstrated, and these sensors are used to characterize the hydrogel mass and swelling characteristics. The mass values obtained from resonant frequency measurements of poly(ethylene glycol)diacrylate (PEGDA) microstructures match well with the values independently verified through volume measurements. The sensors are also used to measure the influence of fluids of similar and greater density on the mass measurements of microstructures. The data show a size-dependent increase in gel mass when fluid density is increased. Lastly, volume comparisons of bulk hydrogels with a range polymer concentration (5% to 100% (v/v)) show a non-linear swelling trend.

3.1 Introduction

Hydrogels are versatile materials used for biological and bio-medical applications [1, 2], namely: drug delivery [3–5], cell encapsulation [6], cell migration [7], tissue engineering [8], and artificial cellular systems [9]. New methods are emerging for fabricating hydrogel-based cellular systems at the size-scale of cell populations and ultimately individual cells; thus, tools are needed to characterize material properties of microscale hydrogels.

Microelectromechanical system (MEMS) resonant mass sensors have been used for mass measurements of a range of substances, including viruses [10, 11], bacteria [12, 13], cells [14–18], biochemicals [18], and liquids and gases [19]. In addition to mass measurement of biological and chemical substances, materials characterization can also be performed through the use of MEMS mass sensors. For example, the physical characteristics of polymer coatings can be measured with cantilevers due to changes in electrostatic, steric, osmotic, or solvation forces that accompany physical changes in the polymer coatings [20].

The most commonly used MEMS resonant mass sensors are cantilever structures, though the conventional cantilever sensors can exhibit >100% non-uniform mass sensitivity, since the location of the object to be measured relative to the free end determines the mass sensitivity [21]. We have recently developed an array of MEMS resonant mass sensors that solve the mass uniformity challenge inherent in cantilever sensors [15, 22]. Our sensors consist of resonating platforms suspended by four angled beam springs, and achieve at least 96% uniformity of mass sensitivity across any point on the measurement platform. Operating in first resonance mode,the platform is driven with a Lorentz force and vibrates vertically in both air (∼160 kHz) and liquid (∼60 kHz). Our sensors have recently been used for direct measurements of cell mass and growth of adherent human cancer cells, showing that cell mass and growth can be measured for single cells [15, 22]. Not only is the stabilization provided by the beam springs essential for restricting the resonance mode and enabling spatial uniformity in mass sensitivity, but the spring-platform structure is sufficiently robust to permit additional material fabrication protocols (such as surface functionalization, cell attachment, and photolithography) between measurements. These advantages provide measurement capabilities for studies on materials beyond what the traditional cantilever mass sensor could enable. This also allows for hydrogel structures to be studied using these sensors. It is difficult to attach pre-fabricated hydrogels individually to the surface of each suspended sensor, and thus the gels must be fabricated directly onto the devices.

The goal of this work is to demonstrate that material microstructures, specifically hydrogels, can be integrated with MEMS resonant mass sensors for materials characterization. Here, we use photolithography to fabricate poly(ethylene glycol)diacrylate (PEGDA) hydrogel microstructures onto the surface of the square resonant sensors. We estimate the mass of hydrogel structures using the sensors and verify the measurement using scanning electron microscopy (SEM) to determine the volume and combining the volume with the density of the hydrogels. We also show that hydrogels can be fabricated to a range of sizes and can be measured under various fluidic conditions to provide insight on material characteristics of hydrogels under changing fluidic environments.

3.2 Materials and Methods

3.2.1 MEMS Resonant Mass Sensors

The fabrication of the MEMS resonant mass sensor array has been previously reported and is only summarized here [15]. The mass sensor array is formed from a silicon-on-insulator wafer with device layer (2.0 µm) and a buried oxide layer (0.3 µm). A silicon dioxide layer is used as an electrical insulation layer. Chrome and gold layers are deposited, patterned, and etched to form the springs and platforms. Electrical leads and bonding pads are formed with additional chrome and gold layers. Xenon difluoride (XeF_2) etching is used to form a "pit" beneath the platform and springs to release the sensor platform. The device is cleaned and a silicon dioxide layer is deposited for insulation; the final oxide is selectively removed from the bonding pad area for wire-bonding. After chip fabrication, the chip is attached to a custom printed circuit board and wire-bonded.

3.2.2 Mass Measurement

The mass of the hydrogel was obtained from the difference of the resonant frequencies of the empty sensor and the sensor with gel. The measurement of the resonant frequency

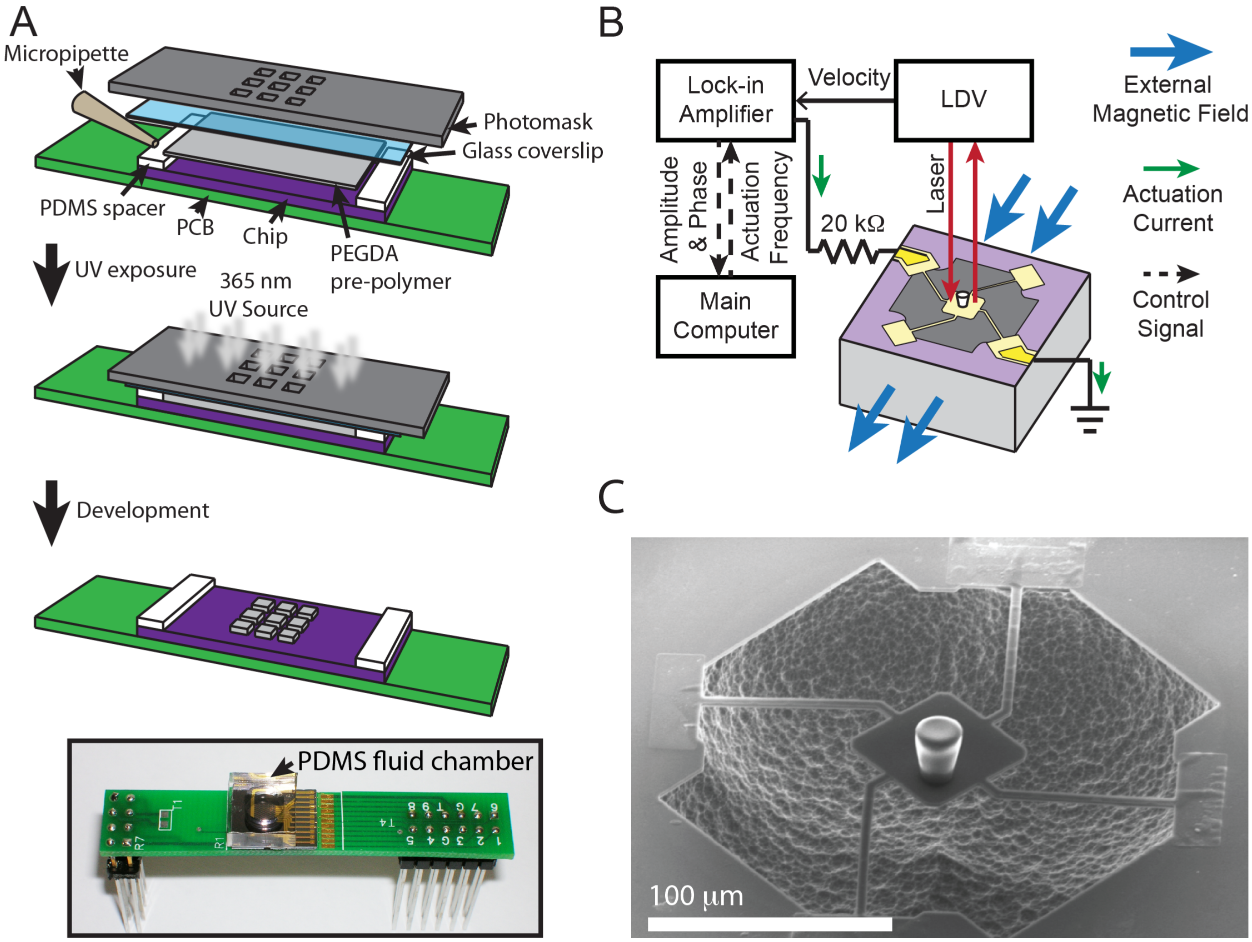

Figure 3.1: Experimental setup and measurement overview. (A) Process overview of photolithographic fabrication of PEGDA-DMPA gel structures onto the MEMS resonant mass sensors (sensor platforms not shown). PEGDA-DMPA pre-polymer and PDMS spacers were sandwiched between the chip (with mass sensors) and coverslip. The chip-coverslip assembly was aligned, brought into contact with the photomask, exposed with 365 nm UV light, developed, and rinsed with DI water. Following lithography, the gels remain immersed in water in a PDMS chamber during measurements; a fully assembled chip is shown. For scale, the printed circuit board (PCB) measures 6.3 cm (length, l), 1.1 cm (width, w). (B) Schematic representation of the measurement set up for measuring the resonant frequency of MEMS resonant mass sensors with laser Doppler vibrometery (LDV). (C) Scanning electron microscopy (SEM) image shows the MEMS mass sensor with a PEGDA-DMPA hydrogel structure fabricated through photolithography onto the suspended platform. For scale, the square platform measures 60×60 µm^2.

was fully automated as shown in Figure 3.1. Briefly, Lorentz force is induced by flowing actuation current through the sensor in a static magnetic field for electromagnetic actuation and laser Doppler vibrometry (LDV; OFV 3001 vibrometer controller and OFV 512 fiber interferometer, Polytec Inc.) is used to measure the resulting velocity of the vibrating platform. The resonant frequency was estimated by comparing the phase of the sensor velocity and that of the actuation cur- rent. Since the spring constant of the sensor structure does not change, the mass of the patterned hydrogel can be solely determined from the resonant frequency, and a series of resonant frequency measurements enables monitoring the mass change [15].

Precise extraction of the sample mass requires resonant frequencies to be measured for each sensor in three different scenarios, a) empty sensors in air, b) empty sensors in fluid pre-lithography, and c) sensors with gels post-lithography. The resonant frequency of each sensor of the array is first measured in air to extract the spring constant, k, in the following equation: $m_{gel} = \frac{k}{4\pi^2}(f_{wetgel}^{-2} - f_{wetempty}^{-2})$. Then, the resonant frequency of each sensor is measured in fluid before and after hydrogel fabrication, which are $f_{wetempty}$ and f_{wetgel}, respectively. The measured resonant frequency shift is determined and ultimately converted to the mass of the gel, mgel on each of the individual sensors. To obtain the final mass of the microstructures without influences of frequency drift, mass readings of adjacent empty sensors are subtracted from the initial mass results [15].

The mass of hydrated 100% PEGDA-(2,2'-dimethoxy-2-phenylaxetophenone) DMPA hydrogel microstructures in fluids of various densities was determined by: a) first measuring the gels in deionized (DI) water (0.99 g/cm^3) after reaching equilibrium, b) followed by a fluid rinse with, and a change to, the density matched solution (73% glucose, 1.13 g/cm^3) similar to the density of 100% PEGDA-DMPA (1.124 g/cm^3). c) The gels were then rinsed with and measured in the higher-density solution (80% glucose, 1.23 g/cm^3), d) followed by rinsing with, then incubation in, DI water prior (>24 h) to a second mass measurement in DI water. e) Lastly, the gels were dried and measured in air to permit the calculation of the mass swelling ratio (Q_m) for determining the Q-factor for comparison to bulk discs.

3.2.3 Surface Chemistry

Surface chemistry was performed in order to functionalize the sensor array with methacrylate groups so as to promote hydrogel microstructure adherence during photolithography. The arrays were cleaned with oxygen plasma (1 min) (Diener Electronic; Ebhausen, Germany). Immediately after cleaning, the sensors were then methacrylated by applying 3-acryloxypropyl trimethoxysilane (5-10 µL) (Gelest, Inc.; Morrisville, PA, USA) directly onto the sensor array and then heated (70 °C, 30-60 min) in a closed Petri dish. Samples were then gently rinsed with acetone and methanol, dried, and used for photolithography within a few days.

To form thin fluidic layers of hydrogel pre-polymer and facilitate the retention of standing isolated hydrogel structures, silanized coverslip fragments were placed on polydimethylsiloxane (PDMS) spacers. Silanized coverslip fragments (approx. 1 cm × 1 cm, #1 thickness) used in the lithography process were prepared by first cleaning the glass with oxygen plasma for 1 min followed by direct exposure to dimethyl(3,3,3, (trifluoropropyl)chlorosilane (10-15 µL) at room temperature (22 to 24 °C) in a vacuum chamber (at least 1-2 h). Coverslips were rinsed with ethanol and dried with a nitrogen stream.

3.2.4 PEGDA-DMPA Hydrogel Solutions

The PEGDA-DMPA hydrogel solution comprises a poly(ethylene glycol)diacrylate (PEGDA; molecular weight, MW 575) and a photoinitiator, 2,2'-dimethoxy-2-phenylaxetophenone (DMPA). Stock solutions of 10-20 mg DMPA per mL PEGDA were prepared and allowed to mix (1-4 h) before use. In this study, hydrogels were microfabricated from undiluted stock PEGDA-DMPA solutions (100% PEGDA- DMPA). To ultimately calculate hydrogel mass from volume measurements, the density of hydrogel pre-polymer was calculated by measuring the mass of defined volumes of PEGDA-DMPA pre-polymer deposited onto weigh boats on an analytical balance. Lower percent gel formulations are 100% PEGDA-DMPA diluted with water. All PEGDA-DMPA pre-polymer preparations were performed under yellow lighting conditions; reagents are stored with protection from light.

3.2.5 Photolithography

Figure 3.1A shows an overview of the photolithography process for PEGDA hydrogel structures on the MEMS sensor array. Hydrogel microstructures were patterned from the PEGDA-DMPA pre-polymer solution described above. The solution acts as a negatively toned photoresist; regions exposed to UV light undergo a free radical polymerization reaction and become insoluble in the developer (DI water). To control the approximate structure thickness, PDMS thin-films were used as spacers (10-50 µm thick) to hold the glass coverslip above the sensor chip. The PEGDA-DMPA pre-polymer solution (3-5 µL) was applied directly to the chip with a pipette and gently covered by a silanized coverslip fragment. In this process, capillary action distributes the solution across the chip and any excess solution can be wicked away with a Kimwipe to ensure a tight coverslip fit due to the surface tension of the pre-polymer. The photomask was aligned to the sensor array in the mask aligner, brought into hard contact with the coverslip, and exposed to 9.4 mW cm^{-2} of 365 nm UV radiation (1-3 min), a time predetermined by iterative exposures. Finally, the coverslip-chip-PCB assembly was removed from the aligner and developed by perfusing DI water through the fluid-filled gap between the coverslip and the chip surface, until the pre-polymer is removed or the cover slip detaches.

3.2.6 Volume Calculations of Microstructures

Volume calculations of hydrogel structures used dimensions obtained from SEM images. To estimate volumetric mass of hydrogel structures, the air-dried 100% PEDGA hydrogel structures were imaged with a scanning electron microscope (SEM) in the Beckman ITG microscopy suite (University of Illinois Urbana-Champaign). Side profile and top view images were acquired in high-vacuum mode with 1 kV accelerating voltage, spot size 2.1 nm, and 2000× magnification.

Dimensions for the area (A) of the hydrogel top, the gel height (h'), the top width (w_{top}), and the gel bottom width (w_{bottom}) were used to calculate the volume of a frustum for estimating structure volume, as shown in Figure 3.2. Due to the presence of a 16° tilt for side profile images, h is the corrected h' using a cosine function ($h = h' cos 16°$). The equation for the frustum volume calculation is $V = \frac{1}{3}\pi \left(r_{eff}^2 + r_{eff} + R_{eff}^2\right) h$, where R_{eff} is the effective top radius and is obtained using $R_{eff} = \sqrt{(A/\pi)}$ assuming the area of a circle, and r_{eff} is the effective bottom radius and is obtained using $r_{eff} = R_{eff}/(w_{top}/w_{bottom})$. Because these dimensions are from SEM images of dry gel structures, the volume calculations are adjusted to account for swelling of the mass of the hydrated structures (see Experimental Section for hydrogel swelling). To obtain the estimated PEGDA hydrogel mass, the calculated volumes (V_h) are multiplied by the hydrogel density (ρ) of 1.124 g/cm^3.

3.2.7 Measuring Hydrogel Swelling

To calculate the hydrated mass of hydrogel microstructures from SEM images, the swelling of 100% PEGDA-DMPA hydrogels was characterized to produce a swelling offset. Swelling of PEGDA-DMPA microstructures is measured differently from bulk discs. The swelling offset is obtained for each microstructure; the diameter of each hydrated gel structure measured with confocal microscopy is divided by the diameter of the same air-dried structure (obtained from the SEM images). The swelling offsets are imposed on the dry volume data to give the hydrated volume (V_h) estimate. Confocal microscopy of 16 structures reveals the hydrated structures being between 1.14- and 1.26-fold greater (average = 1.19) than the same dried structure imaged in the SEM. The measured swelling offset is used for estimating the mass of PEGDA-DMPA microstructures.

To measure swelling of bulk PEGDA-DMPA hydrogel structures independent of the MEMS measurements and photolithography of gel microstructures, bulk hydrogel discs are fabricated by dispensing pre-polymer (200 μL) into the detached cap of a microcentrifuge tube (1.5 mL). The bulk PEGDA-DMPA hydrogel discs are photopolymerized with 365 nm UV light, removed from the molding structure, weighed, and immediately immersed in DI water to achieve equilibrium (24-30 h) prior to processing.

Two separate methods are used in this work to describe changes to the hydrogels as a result of hydration and dehydration. First, the degree of swelling (Q-factor) calculations are performed by factoring the densities of the polymer and water, and the calculated mass swelling ratio. The mass swelling ratio Q_m is measured from the initial and final gel mass of hydrated and completely dehydrated structures, for microstructures the hydrated and dehydrated masses were measured with the MEMS sensors [6]. Lastly, the volume of the swollen gel (V_S) is estimated using $V_S = (v_i(d_s/d_i)) - v_i$ where v_i is the initial gel volume (200 μL), d_s is the diameter of the swollen hydrated gel, and d_i is the diameter of the initial gel. The PEGDA-DMPA hydrogel bulk disc diameters are measured immediately after photopolymerization and again after hydration using microscopy and a quartz micrometer.

3.3 Results and Discussion

Figure 3.1A shows the PEGDA-DMPA polymer fabrication process, a diagram of the measurement system, and a SEM image of a hydrogel microstructure fabricated on the MEMS resonant mass sensor. Table 3.1 shows raw data of photolithographically defined microstructures; the data is representative of the microstructure size range.

MEMS resonant mass sensor arrays are fabricated and calibrated for the mass sensing procedure by in-air and in-liquid resonant frequency measurements [15], prior to fabricating the hydrogel structures. In order to measure the mass of the hydrogels, a PDMS fluidic chamber is assembled on the chip to keep the gel and sensors hydrated (Figure 3.1A) during measurements. Laser Doppler vibometry (LDV) is used to measure the resonant frequency of the sensor with gel (Figure 3.1B), and the images of the sensor and hydrogel were captured

Top Area [µm^2]	Effective Top Radius [µm]	Effective Bottom Radius [µm]	Adjusted Height	Aspect Ratio	Swelling Offset	Est Frustrum Volume [cm^3]
485.8	12.4	6.9	50.5	2.5	1.19	1.52e-8
600.2	13.8	8.5	53.8	2.3	1.19	2.15e-8
150.6	6.9	2.4	45.9	4.8	1.19	3.40e-8
388.4	11.1	4.6	56.9	3.5	1.19	1.17e-8
298.2	9.7	3.4	55.1	4.1	1.19	8.05e-9

Table 3.1: Raw data representative of photolithographically defined 100% PEGDA-DMPA microstructures and the corresponding estimated frustum volumes.

for visual verification. Figure 3.1C shows an electron micrograph of a hydrogel frustum fabricated on the MEMS sensor using photolithography.

By calculating the mass using volume and density measurements [15], we can compare the relationship between the measured mass obtained from the sensor and the theoretical mass; this allows us to determine potential effects of measuring tall structures and structures with a high center of mass. For example, in our previous work on measuring cell mass and growth of adherent cells, "missing mass events" occurred as cells balled up and partially detached from the sensor surface during mitosis [15].

As shown in Figure 3.2, inverted conical frustums have a high center of mass and low surface area of attachment relative to the mass distribution throughout the microstructure. Volume calculations of hydrogel structures used dimensions obtained from SEM images. Dimensions for the area (A) of the hydrogel top, the gel height (h'), the top width (w_{top}), and the gel bottom width (w_{bottom}) were used to calculate the volume of a frustum for estimating structure volume (Figure 3.2). Because these dimensions are from SEM images of dry gel structures, the volume calculations are adjusted to account for swelling of the mass of the hydrated structures (see section on hydrogel swelling). To obtain the estimated PEGDA-DMPA hydrogel mass, the calculated volumes (V_h) are multiplied by the hydrogel density (ρ) of 1.124 g/cm^3.

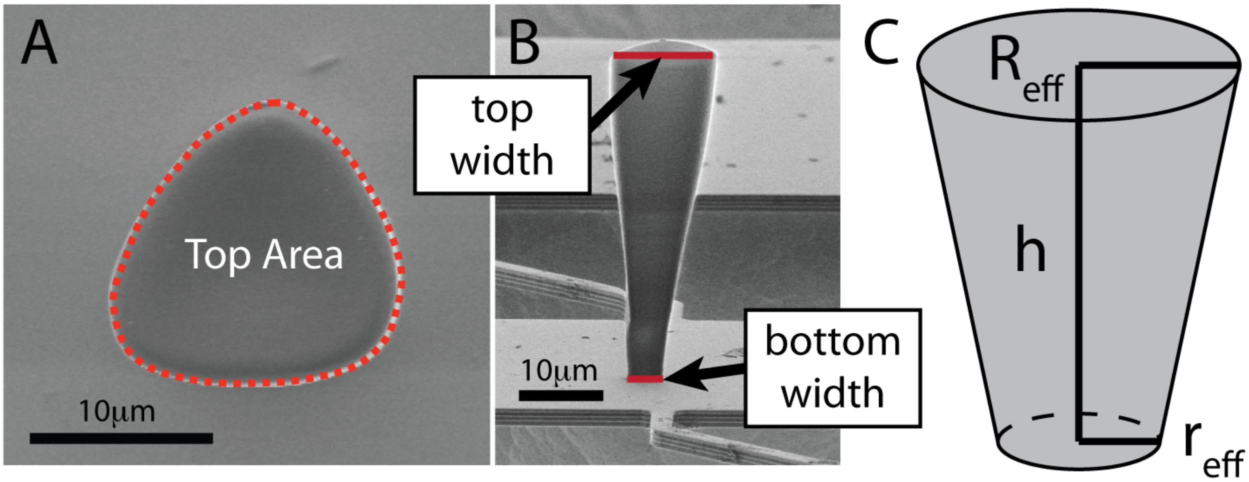

Figure 3.2: Source of measures for calculating gel volume. (A),(B) SEM images of the top and side views of a PEGDA-DMPA hydrogel structure for calculating gel volume and mass. (C) Schematic of an inverted frustum and the dimensions required for calculating the volume of the hydrogel structure to estimate the mass of the hydrogel independent of the LDV-based mass measurements.

Figure 3.3 shows the results of measured and calculated mass values for hydrogel microstructures. Here, we demonstrate that micrometer-scale hydrogel substrates can be integrated with MEMS resonant mass sensors for resolving mass and swelling of stiff (1.61.8 MPa) [23] PEGDA-DMPA hydrogel structures using our MEMS resonant mass sensors. Figure 3.3A shows the range of mass values of hydrated gels measured in water with the LDV system for each sensor number on the chip, and Figure 3.3B shows 4 gel structures on sensors for the corresponding measured and theoretical mass data shown in Figure 3.3C.

Our results show that the relationship between measured and estimated masses are linear, with an average slope of 1.07 and a good data fit ($R^2 = 0.97$). Deviations of data points from the linear trend line can be explained by small imperfections (e.g., sidewalls visible in Figure 3.2B) in fabricated structures which contribute to small differences in the volume-mass estimate. Previous models show that as the Young's modulus and viscosity of a sample increases to ~100 kPa, the measured mass of the sample on the resonant mass sensor is equal to the actual mass of the sample [15]. Here, our results are in agreement with that model.

Volume changes are important material considerations for determining swelling and can

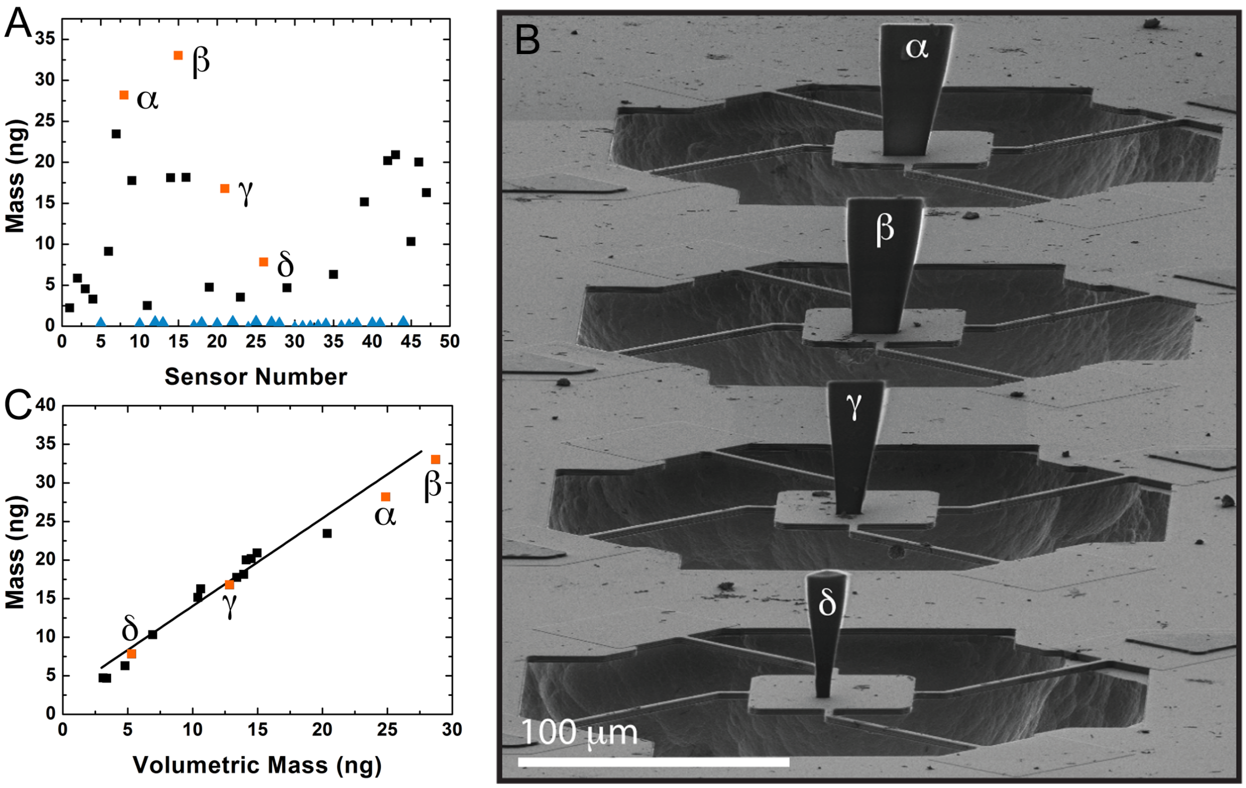

Figure 3.3: Measured and calculated mass of 100% PEGDA-DMPA microstructures. (A) Mass values obtained from 46 sensors for hydrogel structures (squares) and empty sensors (gray triangles). Each data point represents an individual structure or empty sensor. (B) SEM image of 4 sensors with PEGDA-DMPA microstructures fabricated on the sensor surface through photolithography, corresponding mass values for these structures is shown in the accompanying graphs. (C) "Mass (ng)" values obtained from MEMS sensors for PEGDA-DMPA hydrogels are plotted against the "Volumetric Mass (ng)" of the same structures. The volumetric mass of the same structure is independently derived by measuring the structure volume from SEM images and multiplying the volume by density (mass = density × volume). Slope of the solid line for all data points is 1.07 with an R^2 of 0.97, showing a high degree of agreement between calculated and measured masses. (A)-(C)) Open squares marked with Greek letters are for corresponding data points, demonstrating mass values for a range of hydrogel sizes.

influence mass readings for gels in our system. For example, to produce the estimated mass of hydrated PEGDA-DMPA structures, we used confocal microscopy of the hydrated gels structures and SEM images of the same gel to apply a swelling offset to the dry dimensions.

Material swelling is a key factor to consider when working with hydrogel constructs. A common term used to quantitatively describe the swelling of hydrogel materials is the “mass swelling ratio” or the Q_m [6, 24–26]. Q_m is an accurate measure of the maximum change in water content between hydrated and dehydrated gels, because Q_m is a ratio of the hydrated and dry mass values. The Q-factor is another mass-dependent measure of the degree of swelling that takes into account the density of the polymer and hydrating solution; the Q-factor equation (Equation 3.1) incorporates Q_m and accounts for the material and fluid densities but it does not report a change in volume for the gel. Thus, both Q_m and the Q-factor are mass-dependent measures and do not report a change in volume.

$$Q = v_2^{-1} = \rho \left(\frac{Q_m}{\rho_S} + \frac{1}{\rho_P} \right) \tag{3.1}$$

For comparison, we determined the degree of swelling (Q-factor) in water for both the 100% PEGDA-DMPA microstructures and bulk discs using our sensors and conventional methods, respectively. Figure 3.4A shows the Q-factor of bulk structures for a range of concentrations; the data shows a strong agreement between the Q-factor of 100% PEGDA-DMPA bulk discs and microstructures (Figure 3.4A, inset). These results demonstrate that our MEMS mass sensors are suitable tools for measuring gel mass and determining mass swelling ratios for materials characterization of microstructures. In addition, the data presented here for stiff structures is in agreement with the previously published analytical model for mass measurement of viscoelastic materials [15].

Swelling and mass changes of PEGDA-DMPA hydrogels. (A) The Q-factor calculated for a range of PEGDA-DMPA concentrations based on the initial hydrated and final dehydrated mass values for bulk discs (solid black circles). Inset: Comparison of Q-factor measures for 100% PEGDA-DMPA hydrogels from bulk discs (black circle) and for microstructures fabricated with photolithography (open circles, 5 individual gels). Mass of hydrated and dried microstructures was measured using MEMS resonant sensors. (B) The MEMS-measured mass values for 100% PEGDA-DMPA hydrogel structures, covering a range of structure sizes, show corresponding increases with increasing density of the surrounding fluid. (C)

The percent change of apparent mass values of data for 100% PEGDA-DMPA gels (B) in higher density fluids is statistically significant from the initial and final mass measurement in water. Fluid density is 0.99 g/cm^3 for water (24 °C), 1.13 g/cm^3 for 73% glucose in DI water, and 1.23 g/cm^3 for 80% glucose in DI water. The mass change for water is a comparison of the initial and final measurement in water before and after changing the fluid density for 73% and 80% glucose. (D) Normalized apparent mass for the 100% PEGDA-DMPA hydrogel data of (C) shows that smaller structures show a greater normalized mass change than larger structures. (E) Image of a bulk hydrogel disc used to calculate the Q-factor in (A) and the volume change of swelling in (F). (F) Volume increase of bulk hydrogel discs for a range of PEGDA-DMPA concentrations after 30 h of water incubation. Hydration produces substantial increases in gel volume from pre-hydration volume (200 mm^3 for all bulk gels) for 5%, 50% and 100% gels. Average hydrated volumes are 212.5 mm^3 for 5% gels, 214.0 mm^3 for 50% gels, and 227.8 mm^3 for 100% gels.

Our previous cellular data and our current hydrogel data are at the ends of a wide range of material stiffness values (4.1 to 1600+ kPa), thus to more accurately validate models of viscoelastic materials in the mass-spring-damper system, data sets distributed throughout the range of stiffness values will be the focus of future investigations. These data-sets should include a variety of polymer concentrations to achieve a range of material stiffness values. Photolithography of lower percent, highly aqueous, hydrogel pre-polymers produces poorly defined, amorphous gels (data not shown) due to the complexities of internal light reflection and refraction inherent with photolithography. Therefore, the deposition of soft, highly aqueous hydrogels on our sensors will need to be achieved through other means; for example, electrohydrodynamic jetting.

With the ability to accurately measure the mass of stiff hydrogels and perform mass characterization measures (Q_m and Q-factor) with our sensor arrays, we measured the change in mass for PEGDA-DMPA hydrogels in aqueous solutions of increased fluid density to determine how the differences between the gel and immersion media densities influence

Dry Frequency	Wet Frequency Empty [kHz]			Wet Frequency with Gel [kHz]		
in Air [kHz]	DI water	73% Glc	80% Glc	DI water	73% Glc	80% Glc
162.197	64.354	54.068	52.663	58.910	50.289	48.936
142.585	56.045	46.479	45.193	54.949	45.730	44.361
138.829	54.795	45.439	44.129	48.511	41.189	48.972
140.531	55.391	45.834	44.549	50.568	42.802	48.602
140.764	55.518	45.918	44.687	55.202	45.969	48.633

Table 3.2: Raw frequency data from LDV measurements of 100% PEGDA-DMPA microstructures provides mass values for Figure 3.4B-D. Microstructures are within the mass and size range shown in Figure 3.3.

the measured mass. The results for hydrogels attached to MEMS resonant sensors show an increase in apparent mass for an increased fluid density of the surrounding solution. Figure 3.4B shows a density-dependent increase in hydrogel mass values for 5 separate gel structures as measured in the following sequence of aqueous fluids with respective densities; water (0.99 g/cm^3), 73% glucose in water (1.13 g/cm^3), and 80% glucose in water (1.23 g/cm^3). Table 3.2 shows the corresponding resonant frequencies for 73% glucose; 1.13 g/cm^3 is a density-matched solution similar to that of the hydrogel (1.124 g/cm^3). Figure 3.4C shows a statistically significant change in the apparent mass values for gels measured in matched and higher density solutions when compared to the initial measurement of the hydrogels in water. For comparison, the average differences between the final water-based hydrogel measurements to the initial water-based measurement are also shown as "water."

Given the density-dependent increase in swelling for 100% gels, the mass increase data from Figure 3.4B is normalized and plotted in Figure 3.4D to determine if an increase in the hydrodynamic loading is responsible for the mass increase. We expect that the hydrodynamic loading of the increasing density and viscosity of the surrounding fluid plays a role in the fluid density-dependent change in mass values, but how much of an effect has yet to be resolved completely. [27]

Figure 3.4D shows the normalized gel mass across the range of fluid densities; the shape and gray-scale-coded data labels enable a comparison of mass increase according to gel size in the corresponding Figure 3.4B. With larger structures there is a smaller relative change in mass from the initial structure for increasing solution densities, whereas the smaller structures are more affected by the change in fluid density. This result is in contrast to expected effects if hydrodynamic loading is the dominant influence for the mass change.

The total mass of the sensor with the gel is the sum of the gel mass, sensor mass and hydrodynamic loading of the fluid. The hydrodynamic loading increases with higher fluid density and viscosity. In addition, as the gel increases in volume, the gel-on-sensor structure has an increased surface area, which will influence the platform-sample acceleration and directly increase the induced mass. Thus, larger structures would have a greater induced mass over smaller structures if hydrodynamic loading was the dominant contributor to the size-dependent change. This suggests that the difference in gel mass attributed to the increasing solution density is not entirely due to hydrodynamic loading, but that some other factor influences these results.

Gels are water permeable and known to swell upon hydration, thus two other possible contributions include disproportionate changes in volume or density. For the former, a change in volume occurs during structure swelling, the completeness of swelling may influence the size-dependent change in mass reading. The Q-factor data suggest a small change in the swelling of 100% PEGDA-DMPA gels, but this measure does not report a change in structure size. To better determine how swelling changes the structure size of 100% PEGDA-DMPA microstructures, we measured the volume change of bulk PEGDA-DMPA discs between pre- and post-hydration states. Figure 3.4E is a representative image of the bulk discs used to determine the Q-factor of a range of gel formulations in Figure 3.4A and the volume increase for swelling of 100% PEGDA-DMPA gels shown in Figure 3.4F.

Figure 3.4F shows the change of hydrogel volume for bulk hydrogel discs that occurs between photopolymerization and 30 h of hydration in DI water; results are averages of

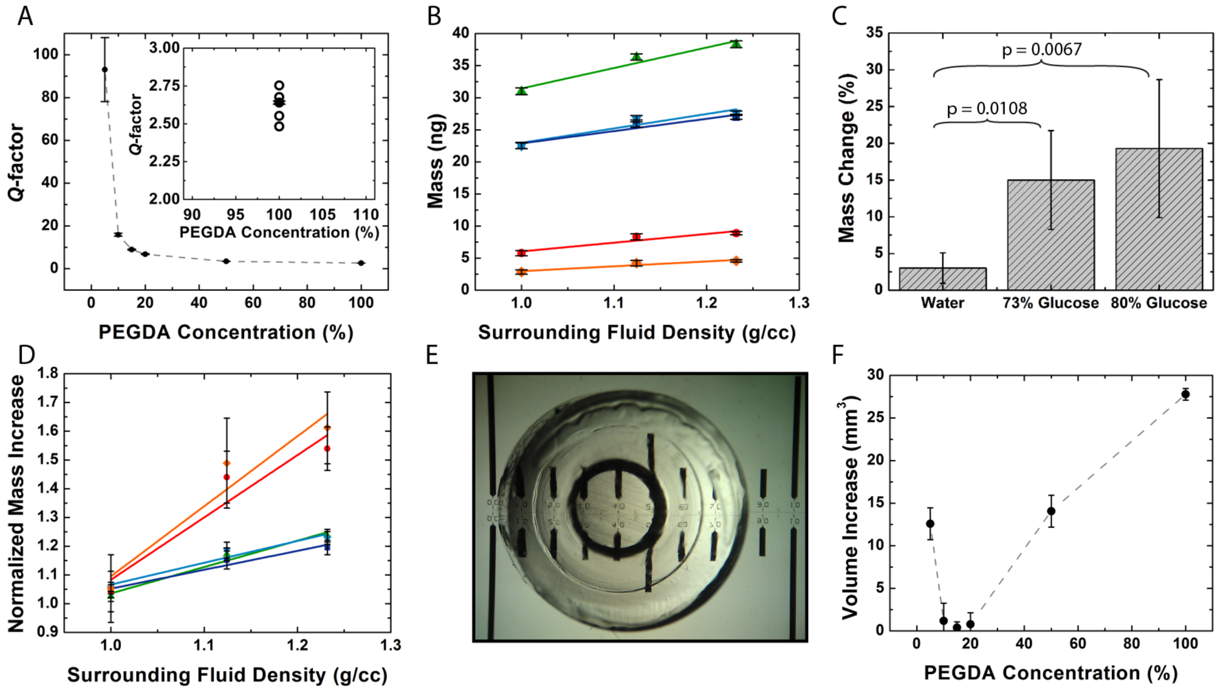

Figure 3.4: Swelling and mass changes of PEGDA-DMPA hydrogels. (A) The *Q*-factor (a mass-based measure for degree of swelling) calculated for a range of PEGDA-DMPA concentrations, the data is based on the initial hydrated and final dehydrated mass values for bulk discs (solid black circles). Inset: Comparison of *Q*-factor measures for 100% PEGDA-DMPA hydrogels from bulk discs (black circle) and for microstructures fabricated with photolithography (open circles, 5 individual gels). (B) The MEMS-measured mass values for 100% PEGDA-DMPA hydrogel structures, covering a range of structure sizes, show corresponding increases with increasing density of the surrounding fluid. (C) The percent change of apparent mass values of data for 100% PEGDA-DMPA gels (B) in higher density fluids is statistically significant from the initial and final mass measurement in water. Fluid density is 0.99 g/cm^3 for water (24 °C), 1.13 g/cm^3 for 73% glucose in DI water, and 1.23 g/cm^3 for 80% glucose in DI water. The mass change for water is a comparison of the initial and final measurement in water before and after changing the fluid density for 73% and 80% glucose. (D) Normalized apparent mass for the 100% PEGDA-DMPA hydrogel data of (C) shows that smaller structures exhibit a greater normalized mass change than larger structures. The data sets are normalized values from the same sample structures for graph (B), three separate measures each point, mean ± SD. (E) Image of a bulk hydrogel disc used to calculate the *Q*-factor in (A) and the volume change of swelling in (F). (F) Volume increase of bulk hydrogel discs for a range of PEGDA-DMPA concentrations after 30 h of water incubation. Hydration produces substantial increases in gel volume from pre-hydration volume (200 mm^3 for all bulk gels) for 5%, 50% and 100% gels. Average hydrated volumes are 212.5 mm^3 for 5% gels, 214.0 mm^3 for 50% gels, and 227.8 mm^3 for 100% gels.

three separate hydrogel discs for each data point for a total of 18 discs. As a result, higher gel concentrations (50% and 100%) show greater swelling compared to lower percent gels, with the exception of the 5% gel. It is clearly evident from volume swelling measures that stiff 100% PEGDA-DMPA structures exhibit the greatest volume increase compared to softer gels of decreased PEGDA-DMPA composition (Figure 3.4F). The change in gel volume for bulk hydrogel discs provides an added perspective to the mass-based Q-factor. This large amount of swelling could be explained by the increased osmotic pressures of high percent gels. Although the 100% PEGDA-DMPA gel has a greater stiffness than lower percent PEGDA-DMPA gel compositions, the material stiffness does not override the polymer's capacity to swell. Data for the 5% gels suggest that the polymer network is weak enough to give way to the osmotic pressure to yield a robust change in the gel dimensions, and the 15% gel appears to be balanced by the osmotic pressure and the polymer stiffness (Figure 3.4F).

A size-dependent change in microstructure density could explain the size-dependent mass change in fluids of increasing density. A change in the microstructure density is the combination of a number of influences. 1) Surface-area-to-volume ratio: Smaller structures have a greater surface-area-to-volume ratio than larger structures. From Fick's first law of diffusion, assuming that the structures are exactly the same except for their size, then you would expect the diffusion through the smaller structure to occur more rapidly, which explains why there is a change in the mass values after the changing the fluid density. Basically, the diffusion flux, J, is related to dC/dx, where dC is the concentration change and dx is the distance of diffusion. The smaller sample should have the larger dC/dx. 2) Polymer pore size: As the polymer swells the polymer pore size changes, pore size and distribution will influence the rate of diffusion throughout the polymer structure and the time required for the gel to reach equilibrium with the surrounding fluid. If gel swelling is neither uniform nor complete, then larger structures may not have uniform pore sizes or glucose distribution compared to smaller structures, alternatively the structure may take longer to achieve equilibrium.

Taken together, it is possible that smaller PEGDA-DMPA gel microstructures could achieve a greater density and mass of the more dense media (i.e., increased glucose) through diffusion by achieving equilibrium with the surrounding fluid prior to their larger counterparts. To further answer this out-standing question and validate these possibilities, hydrogel microstructures of various compositions should be measured to observe the size-dependent change for gels that show different percent swelling increases according to the range of gel compositions.

3.4 Conclusion

We conclude that micrometer-scale hydrogel structures can be affixed to MEMS resonant sensors to measure the gel mass for microstructure materials characterization. Our results show a quantitative method for measuring mass and swelling of hydrogel microstructures, from which we conclude that gel size and stiffness influence the swelling and diffusion of substances into the gel. Furthermore, increased mass values obtained by elevating fluid densities of immersion media are observed. Our data suggests that a confluence of multiple factors contribute to this observation. Future work will focus on resolving these complexities and on characterizing hydrogels of different viscoelastic properties to validate and expand models of mass-spring-damper systems for measuring soft materials and biological samples with resonant sensors. Due to the high refractivity of aqueous solutions, methods other than photolithography (e.g., electro-hydrodynamic jetting) must be implemented for depositing hydrogels of all gel compositions (5%-100%) onto the platform sensor to answer these questions.

3.5 References

[1] J. J. Schmidt, J. Jeong, and H. Kong. The interplay between cell adhesion cues and curvature of cell adherent alginate microgels in multipotent stem cell culture. *Tissue Engineering Part A*, 17(21-22):2687–2694, 2011.

[2] Y. Liang, J. Jeong, R. J. DeVolder, C. Cha, F. Wang, Y. W. Tong, and H. Kong. A cell-instructive hydrogel to regulate malignancy of 3D tumor spheroids with matrix rigidity. *Biomaterials*, 2011.

[3] T. R. Hoare and D. S. Kohane. Hydrogels in drug delivery: progress and challenges. *Polymer*, 49(8):1993–2007, 2008.

[4] Y. M. Kolambkar, K. M. Dupont, J. D. Boerckel, N. Huebsch, D. J. Mooney, D. W. Hutmacher, and R. E. Guldberg. An alginate-based hybrid system for growth factor delivery in the functional repair of large bone defects. *Biomaterials*, 32(1):65, 2011.

[5] X. Zhao, J. Kim, C. A. Cezar, N. Huebsch, K. Lee, K. Bouhadir, and D. J. Mooney. Active scaffolds for on-demand drug and cell delivery. *Proceedings of the National Academy of Sciences USA*, 108(1):67–72, 2011.

[6] V. Chan, P. Zorlutuna, J. H. Jeong, H. Kong, and R. Bashir. Three-dimensional photopatterning of hydrogels using stereolithography for long-term cell encapsulation. *Lab On A Chip*, 10(16):2062, 2010.

[7] P. Tayalia, E. Mazur, and D. J. Mooney. Controlled architectural and chemotactic studies of 3D cell migration. *Biomaterials*, 32(10):2634–2641, 2011.

[8] G. D. Nicodemus and S. J. Bryant. Cell Encapsulation in Biodegradable Hydrogels for Tissue Engineering Applications. *Tissue Engineering Part B: Reviews*, 14(2):149–165, June 2008.

[9] V. Chan, J. H. Jeong, P. Bajaj, M Collens, T. Saif, H. Kong, and R. Bashir. Multimaterial bio-fabrication of hydrogel cantilevers and actuators with stereolithography. *Lab On A Chip*, 12(1):88, 2011.

[10] A. Gupta, D. Akin, and R. Bashir. Detection of bacterial cells and antibodies using surface micromachined thin silicon cantilever resonators. *Journal of Vacuum Science & Technology B*, 22(6):2785–2791, 2004.

[11] A. Gupta, J. P. Denton, H. McNally, and R. Bashir. Novel fabrication method for surface micromachined thin single-crystal silicon cantilever beams. *Journal of Microelectromechanical Systems*, 12(2):185–192, 2003.

[12] A. Gupta, H. Lia, R. Gomezc, W. J. Changd, Y. M. Kood, H. Changa, G. Andreadakisa, D. Akina, and R. Bashir. BioMEMS to bionanotechnology: state of the art in integrated biochips and future prospects. In *Proc. of SPIE Vol*, volume 5593, page 341, 2004.

[13] A. Gupta, J. P. Denton, H. McNally, and R. Bashir. Novel fabrication method for surface micromachined thin single-crystal silicon cantilever beams. *Journal of Microelectromechanical Systems*, 12(2):185–192, 2003.

[14] K. Park, J. Jang, D. Irimia, J. Sturgis, J. Lee, J. P. Robinson, M. Toner, and R. Bashir. 'Living cantilever arrays' for characterization of mass of single live cells in fluids. *Lab On A Chip*, 8(7):1034–1041, 2008.

[15] K. Park, L. J. Millet, N. Kim, H. Li, X. Jin, G. Popescu, N. R. Aluru, K. Hsia, and R. Bashir. Measurement of adherent cell mass and growth. *Proceedings of the National Academy of Sciences USA*, 107(48):20691–20696, 2010.

[16] M. Godin, F. F. Delgado, S. Son, W. H. Grover, A. K. Bryan, A. Tzur, P. Jorgensen, K. Payer, A. D. Grossman, M. W. Kirschner, and S. R. Manalis. Using buoyant mass to measure the growth of single cells. *Nature Methods*, 7(5):387–390, May 2010.

[17] A. K. Bryan, A. Goranov, A. Amon, and S. R. Manalis. Measurement of mass, density, and volume during the cell cycle of yeast. *Proceedings of the National Academy of Sciences USA*, 107(3):999–1004, January 2010.

[18] T. P. Burg, M. Godin, S. M. Knudsen, W. Shen, G. Carlson, J. S. Foster, K. Babcock, and S. R. Manalis. Weighing of biomolecules, single cells and single nanoparticles in fluid. *Nature*, 446(7139):1066–1069, 2007.

[19] N. V. Lavrik, M. J. Sepaniak, and P. G. Datskos. Cantilever transducers as a platform for chemical and biological sensors. *Review of Scientific Instruments*, 75(7):2229, 2004.

[20] J. N. Israelachvili. *Intermolecular and surface forces: revised third edition*. Academic Press, 2011.

[21] S. Dohn, R. Sandberg, W. Svendsen, and A. Boisen. Enhanced functionality of cantilever based mass sensors using higher modes. *Applied Physics Letters*, 86(23):233501, 2005.

[22] K. Park, L. Millet, N. Kim, H. Li, K. Hsia, N. R. Aluru, and R. Bashir. MEMS mass sensors with uniform sensitivity for monitoring cellular apoptosis. In *Solid-State Sensors, Actuators and Microsystems Conference (TRANSDUCERS), 2011 16th International*, pages 759–762. IEEE, 2011.

[23] Z. Drira. Investigation of the mechanical properties of poly (ethylene glycol) diacrylate by nanoindentation using atomic force microscopy. 2009.

[24] J. A. Beamish, J. Zhu, K. Kottke-Marchant, and R. E. Marchant. The effects of monoacrylated poly (ethylene glycol) on the properties of poly (ethylene glycol) diacrylate hydrogels used for tissue engineering. *Journal of Biomedical Materials Research Part A*, 92(2):441–450, 2010.

[25] S. J. Bryant, K. L. Durand, and K. S. Anseth. Manipulations in hydrogel chemistry control photoencapsulated chondrocyte behavior and their extracellular matrix production. *Journal of Biomedical Materials Research Part A*, 67(4):1430–1436, 2003.

[26] J. L. Young and A. J. Engler. Hydrogels with time-dependent material properties enhance cardiomyocyte differentiation *in vitro*. *Biomaterials*, 32(4):1002–1009, 2011.

[27] S. Basak, A. Raman, and S. V. Garimella. Hydrodynamic loading of microcantilevers vibrating in viscous fluids. *Journal of Applied Physics*, 99(11):114906–114906, 2006.

Chapter 4

Examining the Micromechanical Properties of Hydrogels Using MEMS Resonant Sensors

Hydrogels have gained wide usage in a range of biomedical applications because of their biocompatibility and the ability to finely tune their properties, including viscoelasticity. The use of hydrogels on the microscale is increasingly important for the development of drug delivery techniques and cellular microenvironments, though the ability to accurately characterize their micromechanical properties is limited. Here we demonstrate the use of microelectromechanical systems (MEMS) resonant sensors to estimate the properties of poly(ethylene glycol) diacrylate (PEGDA) microstructures over a range of concentrations. These microstructures are integrated on the sensors by deposition using electrohydrodynamic jet printing. Estimated properties agree well with independent measurements made using indentation with atomic force microscopy.

4.1 Introduction

Hydrogels are critically important to many biomedical applications [1] including drug delivery [2] and tissue engineering [3] due to their biocompatibility and mechanical properties. Hydrogel stiffness can be controlled to mimic a desired tissue microenvironment, enabling hydrogel tissue scaffolds that have mechanical behavior similar to that of extracellular matrix [4]. There is, however, a lack of understanding of the micromechanical behavior of hydrogels and a need for suitable methods to probe this behavior [5, 6]. In particular, it is difficult to make quantitative in situ mechanical property measurements because the elastic and viscous properties of hydrogels can vary over several orders of magnitude depending on composition, concentration, and swelling [7, 8]. A deeper understanding of how to control and measure hydrogel mechanical properties is required in order to engineer cellular microenvironments.

Hydrogels are used for both macroscopic [9] and microscopic cellular environments [10]. Therapeutic vascularization techniques for regenerative medicine rely on macroscopic templates of hydrogels with micro-patterns and embedded angiogenic factors [9, 11]. 3D cell encapsulation with hydrogels can guide cellular processes such as differentiation [10]. Hydrogels have also been developed for layering on the inner surface of blood vessels to control timed drug release for intravascular localized drug delivery [12]. At the macroscale, the mechanical properties of hydrogels can be measured using dynamic mechanical analysis,[5] oscillatory shear rheometry [13], and elastography [14]. Much less work has been published on the mechanical properties of hydrogels at the micrometer scale. Atomic force microscopy (AFM) measurements can obtain the hardness of soft biological materials, but data interpretation is difficult due to the complex geometry of the AFM tip [15]. A quartz crystal microbalance (QCM) can estimate the viscoelasticity of materials in an aqueous environment, but samples are limited to uniform thin films with macroscopic diameters that depend on QCM electrode size. Ideally, micrometer scale hydrogel mechanical property measurements would include: measurements on microscopic amounts of hydrogel; the measurement of both elastic and viscous properties, both of which can vary significantly with hydrogel composition; hydrogel characterization in a liquid environment; and hydrogels that have been integrated on a microscopic lab-on-chip platform.

We propose to measure the viscoelastic properties of hydrogels using microelectromechanical system (MEMS) resonant sensors. These sensors have traditionally enabled mass measurement of a range of biomaterials, such as viruses [16], bacteria [17], cells [18–20], biochemicals [19], and polymers [21]. Resonant sensors rely on the technique of measuring frequency shift, where the difference in resonant frequency between an unloaded sensor and a sensor loaded with a sample reflects the adhered mass. However, if the material is soft, such as with hydrogels, it introduces a complicated coupled-oscillator effect where the material will oscillate relative to the sensor, and the measured resonant frequency depends on the viscoelasticity of the material in addition to its mass. The coupled-oscillator effect can be described by a two degree-of-freedom (2DOF) dynamic system, which is used to estimate the viscoelasticity of soft materials through apparent mass measurements with the MEMS resonant sensor.

This paper describes the measurement of the elastic and viscous properties of nanogram-scale samples of poly(ethylene glycol) diacrylate (PEGDA) hydrogel samples (MW 575 g·mol^{-1}) that have been integrated onto a MEMS resonant sensor. Because it is difficult to attach pre-fabricated hydrogels individually to the surface of each suspended sensor the gels must be fabricated directly onto the devices. Here we use electrohydrodynamic jet (e-jet) printing [22], which uses high electric fields to pattern liquids onto grounded substrates, for integrating hydrogels onto our fully suspended MEMS resonant sensor. The mechanical properties of cross-linked PEGDA hydrogel structures are tunable by varying the polymer concentration [23], and the properties of samples prepared with 5-20% hydrogel concentration are investigated in this paper.

4.2 Experimental Section

4.2.1 Hydrogel preparation

PEGDA (MW 575 g·mol^{-1}) and 2,2-dimethoxy-2-phenylacetophenone (DMPA), a photoinitiator, were combined in the ratio of 10 mg DMPA per mL PEGDA to form a stock solution, and the photoinitator was allowed to dissolve for 4 hours before use. Lower concentrations were obtained by diluting stock solutions in DI water. Concentrations indicate a volume/volume ratio of stock solution to diluted total. All solution preparation and storage took place in the absence of UV light.

Prior to initiating microstructure deposition, the surface was methacrylated following a previously established protocol [24]. Chips were cleaned under oxygen plasma for 2 minutes, then treated in small groups in a 500 mL glass jar. 250 µL of 3-acryloxypropyl trimethoxysilane was pipetted around the base of the jar, after which the jar was sealed and placed in an oven at 80 °C for at least 4 hours. During baking, the silane vaporizes and deposits on the surface, forming pendant methacrylate groups to promote hydrogel adherence [24]. Samples were then gently rinsed with acetone and methanol, allowed to air dry, and used within 24 hours. The pre-polymer solution was then deposited on the sensors using e-jet printing. After deposition the droplets undergo a free radical polymerization reaction stimulated by 9 $W \cdot cm^{-2}$ UV curing spot lamp and become insoluble in the developer [25].

4.2.2 Mechanical Property Characterization

An MFP-3D Asylum Research (Santa Barbara, CA) AFM was used to characterize mechanical properties using thin film hydrogel samples (70 µm thickness). We used a silicon nitride cantilever with a spring constant of 0.06 $N \cdot m^{-1}$ and a 2.5 µm silica spherical indenter to extract force-indentation curves. The elastic modulus of the hydrogel was then extracted from the region of elastic deformation using the Hertz model:

$$F = \frac{4}{3} E_C R^{\frac{1}{2}} d^{\frac{3}{2}} \tag{4.1}$$

where F is the magnitude of the loading force, E_C is the effective elastic modulus, R is the radius of the indenter probe, and d is the indentation displacement. However, the effective elastic modulus also includes the elastic effects of the spherical indenter, which must be separated from the elasticity of the sample material using the following equation:

$$\frac{1}{E_C} = \frac{1 - \nu_{gel}^2}{E_{gel}} + \frac{1 - \nu_{glass}^2}{E_{glass}} \tag{4.2}$$

where E_{gel} and E_{glass} are the elastic moduli of the hydrogel and the glass spherical particle, and ν_{gel} and ν_{glass} are the Poisson ratios of the two materials. The material properties of the spherical particle are 68 GPa and 0.19, as characterized previously by Asylum Research, and we assumed a ν_{gel} of 0.45, as suggested by previous work for hydrogel incompressibility [26].

Creep indentation measurements with AFM used the same cantilever and indenter tip. A step load was applied to the cantilever probe and the resulting force applied from the cantilever to the sample was held constant through a feedback loop on the cantilever deflection. While the force was held constant, the linear variable differential transformer (LVDT) signal of the AFM was monitored for ten seconds to collect a creep curve. Based on the Kelvin-Voigt model, we can derive the following response equation:

$$I(t) = \frac{F_0}{k}\left[1 - e^{-t\frac{k}{\eta}}\right] \tag{4.3}$$

where $I(t)$ is the indentation as a function of time t, defined as the difference between of the Z-sensor (LVDT) and cantilever deflection, which is held constant. F_0 is the magnitude of the loading force, k is the spring constant of the material, and η is the viscosity of the material. Exponential fitting of the indentation curve returned the material viscosity. All AFM experiments were performed at a room temperature of 22 °C.

4.2.3 Confocal Microscopy

We used confocal microscopy to determine volumes and calculate the volumetric mass of the hydrogel microstructures. PEGDA hydrogel microstructures were labeled with fluorescein isothiocyanate-conjugated poly-L-lysine in DI water (50-100 µg mL^{-1}, >12 hours). Prior to imaging, the MEMS sensors with hydrogels were rinsed and immersed in DI water. Confocal image stacks (Z-stacks) were acquired with a Zeiss 710 laser scanning confocal microscope using an Argon laser (488 nm) and a Plan-Apochromat 20x/0.8 objective (Carl Zeiss Microscopy GmbH; Jena, Germany). To ensure that the Z-stacks represented the gel dimensions accurately in three-dimensions, XYZ voxel size (X=0.244 µm, Y=0.244 µm, Z=1.0 µm) was set based on Nyquist criteria (two pixels per actual unit resolution in XYZ).

4.2.4 Apparent mass measurements with resonant sensor

For each sensor, three different resonant frequencies were measured. The resonant frequency in air was measured to extract the spring constant of each individual sensor and to compensate for minute sensor to sensor differences that may exist from chip fabrication. The resonant frequency (reference frequency for mass measurements) of each sensor in DI water was measured. Then, the gels were deposited on the sensor array and the resonant frequencies and optical images of each selected sensor were collected. With the spring constant and the reference frequency, the measured frequencies were converted to the mass of individual sensors, with and without attached hydrogels, ultimately allowing for the mass of individual hydrogel microstructures to be extracted, using the following equation:

$$m_{gel} = \frac{k}{4\pi^2}\left(f_{wetgel}^{-2} - f_{wetempty}^{-2}\right) \tag{4.4}$$

where f_{wetgel} is the resonance frequency of the sensor with the gel in liquid, $f_{wetempty}$ is the resonance frequency of the empty sensor, k is the spring constant of the sensor, and m_{gel} is the mass of the gel.

4.2.5 Estimation of Mechanical Properties using Resonant Sensors

The 2DOF model of the resonant sensor system with attached Kelvin-Voigt solid can be described by the following equations of motion:

$$\begin{bmatrix} m_1 & 0 \\ 0 & m_2 \end{bmatrix} \begin{pmatrix} x_1 \\ x_2 \end{pmatrix} + \begin{bmatrix} c_1 + c_2 & -c_2 \\ -c_2 & c_2 \end{bmatrix} \begin{pmatrix} x_1 \\ x_2 \end{pmatrix} + \begin{vmatrix} k_1 + k_2 & -k_2 \\ -k_2 & k_2 \end{vmatrix} \begin{pmatrix} x_1 \\ x_2 \end{pmatrix} = \begin{pmatrix} F_0 \\ 0 \end{pmatrix} e^{i\omega t} \tag{4.5}$$

For each sensor, the spring constant k_1 and resonant frequency ω_1 are measured (approximately 20 N·m^{-1} and 4.0×10^5 radians·s^{-1}, respectively), and together are used to calculate the mass of the sensor, $m_1 = k_1/\omega_1^2$ (approximately 125 ng). The coefficient of viscous damping for each sensor, c_1, is estimated to be approximately 9.5×10^{-6} N·s·m^{-1}. Given non-dimensional parameters $\Omega = \omega_2/\omega_1$ and $M = m_2/m_1$, Eq. 4.6 describes the resonance condition of the 2DOF system ($\omega = \omega_2$):

$$D_1 k_2^2 + D_2 k_2 + D_3 + D_4 c_2^2 = 0, \tag{4.6}$$

where the coefficients are described by:

$$\begin{aligned} D_1 = \frac{1 - \Omega^2(1 + M)}{k_1^2}, D_2 = \frac{\Omega^2 M (2\Omega^2 - 2 + \Omega^2 M)}{k_1}, \\ D_3 = \Omega^4 M^2 (1 - \Omega^2), D_4 = \frac{\Omega^2 (1 - \Omega^2 - \Omega^2 M)}{k_1 m_1}. \end{aligned} \tag{4.7}$$

The structural parameters of the hydrogel in the 2DOF model, k_2 and c_2, are related to the mechanical properties, E and η. For an axially-loaded member of uniform cross-section, this relationship is defined by a shape factor $g = 2A/L$, where A is cross-sectional area and L is height [27]. However, the hydrogel structures used here are dome-shaped and have varying cross-sectional area, thus we cannot use g alone. To determine an effective shape, the hydrogel was modeled as a series of N thin members arranged in parallel. The number of members used for each sample was determined by the number of slices captured by confocal microscopy, with the height of each equal to the slice thickness, and the cross-sectional area calculated using Amira during volume reconstruction. Each thin member has a shape factor, g_n, which leads to an effective shape factor, g_e:

$$g_e = \left(\sum_{n=1}^{N} \frac{1}{g_n} \right)^{-1} \tag{4.8}$$

In principle, g_e will be different for each hydrogel structure, and can be used to calculate the effective stiffness, k_2, and damping coefficient, c_2:

$$k_2 = g_e \cdot E; c_2 = g_e \cdot \eta. \tag{4.9}$$

In effect, the mechanical properties of each hydrogel can be estimated using Eq. 4.6 with appropriate shape factor. However, estimating two unknowns in a nonlinear equation is challenging given a single measurement. Instead, by measuring a number of different hydrogel structures varying in concentration, and assuming the elasticity and viscosity of all samples obey a power-law dependence on concentration, the power-law behavior can be estimated using all samples. For each sample, Eq. 4.6 can be reformulated as an error term for each sample, y:

For each sample, Eqn. 4.6 can be reformulated to as an error term for each sample, y:

$$y\left(E_0, \eta_0, a, b\right) = D_1 g_e^2 E_0^2 C_h^{2a} + D_2 g_e E_0 C_h^a + D_3 + D_4 g_e^2 E_0^2 C_h^{2b}. \tag{4.10}$$

where E_0 and η_0 are the power-law coefficients for elasticity and viscosity, a and b are the respective power-law exponents, and C_h is the hydrogel concentration. The exponents and coefficients can be found as the parameters that minimize the error term across the entire population of observations, P:

$$\hat{E}_0, \hat{\eta_0}, \hat{a}, \hat{b} = \underset{E_0, \eta_0, a, b}{\arg\min} \sum_{p=1}^{P} y_p^2 \left(E_0, \eta_0, a, b\right) \tag{4.11}$$

The minimum error was found by iteratively updating each parameter based on the gradient of its error dependence. Solutions were restricted based on the requirement of having vibrations in-phase at resonance.

4.3 Results and Discussion

The MEMS resonant sensor used in this study consists of a 60×60 µm^2 platform suspended by four micro beam-springs to provide uniform mass sensitivity across the sensor [18, 28]. Figure 4.1 shows an overview of the typical mass measurement with the sensor. Our measurement uses electromagnetic actuation and a laser Doppler vibrometer (LDV) system to measure the velocity of the vibrating platform in conjunction with a feedback loop and a lock-in amplifier to iteratively determine the resonant frequency (fig. 4.1A). Measurement of the resonant frequency of the sensor with an adhered material, and comparison with that of an empty sensor, allows for the mass of the material to be calculated. The resonance condition is also dependent on the viscoelastic properties of the adhered material, which becomes significant with soft materials and skews the apparent measured mass. By treating the model as a Kelvin-Voigt viscoelastic solid [29], the sensor with adhered solid was modeled as the 2DOF spring-mass-damper dynamic system shown in figure 4.1B [18]. Figure 4.1C shows predictions using the model of how the ratio of apparent mass to actual mass changes over a range of mechanical properties.

To establish a baseline for the hydrogel properties, we used AFM to measure the elastic and viscous properties of hydrogel samples while submerged in DI water. AFM analysis utilized thin film hydrogel samples with thickness of approximately 70 µm created by cross-linking pre-polymer with a 365 nm UV light source. We used a silicon nitride cantilever with a spring constant of 0.06 $\mathrm{N{\cdot}m^{-1}}$ and a 2.5 µm silica spherical-tip. Force-indentation curves coupled with the Hertz contact mechanics model determined the elastic moduli of hydrogels at each PEGDA concentration (figure 4.2A). Fitting used the linear elastic deformation region of the curve, and a low loading rate was selected to minimize viscous effects in this

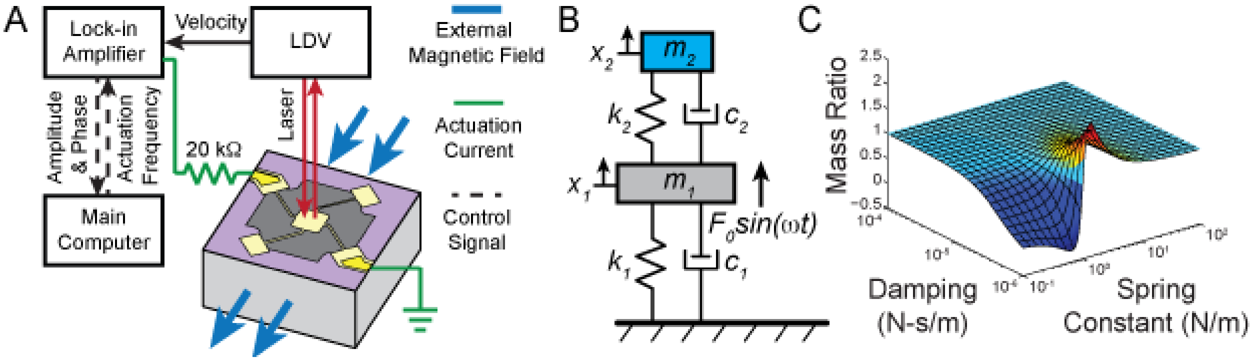

Figure 4.1: Overview of the measurement approach. (A) Schematic summarizing the frequency measurement setup. (B) Schematic of the free body diagram of two-degree-of-freedom (2DOF) dynamic model, where m_1, k_1, c_1, and x_1 are the mass, spring constant, damping, and displacement of the sensor, and m_2, k_2, c_2, and x_2 are the mass, spring constant, damping, and displacement of the adhered object. (C) Three-dimensional model plot summarizing how the spring constant and damping of the object influence mass measurement (mass ratio is apparent mass divided by actual mass).

region [30–33]. For each sample, we measured approximately ten locations across the surface and averaged, with the resulting elastic modulus ranging from 2.84 to 228.94 kPa, for 5% to 20% concentration (table 4.1).

Polymer Solution Concentration (%)	**Density (g/mL)**	**Elastic Modulus (kPa)**	**Viscosity (mPa-s)**
5	1.0062	2.8	0.2
10	1.0124	44.6	2.1
15	1.0186	137.0	3.7
20	1.0248	228.9	5.1

Table 4.1: AFM data of viscoelastic measurements of all polymer solution concentrations. Note that the measured viscosity of the 5% concentration samples are unreliable as it is less than water.

AFM also determined the viscosity of the hydrogel structures through creep experiments, where we applied an instantaneous load and then held for ten seconds, while monitoring the deformation (figure 4.2B). Utilizing a Kelvin-Voigt viscoelastic model we can extract the viscosity for each sample [34], again averaged over ten measurements, with the resulting

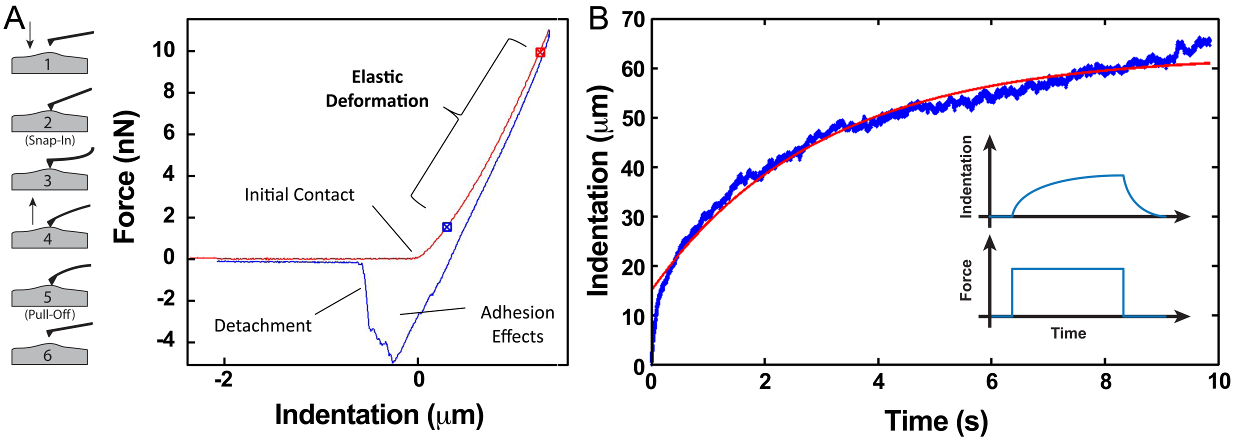

Figure 4.2: Overview of the atomic force microscopy mechanical property measurements. (A) Force-indentation measurement cartoon, where the cantilever probe is brought down into contact, and pushed into the surface to a set force and the retracted from the surface until the cantilever is fully detached. Example raw data of the force-indentation curve depicting the elastic deformation region. (B) Creep measurement inset shows the applied load vs. time and the indentation response vs. time. Example raw data of the indentation-time curve depicting the curve fit for the data set.

viscosity ranging from 0.2 to 5.1 mPa·s (table 4.1). The measurement of the viscosity of the 5% hydrogel was problematic due to the challenges of performing AFM creep measurements on low viscosity materials. For analysis and display we assumed a viscosity value of 1.0 mPa·s for the 5% hydrogel corresponding to water at 20 °C. Note that this value does not alter the findings using the resonant sensor as described later.

The measured elastic modulus, E, and viscosity, η, of a hydrogel solid exhibit a power-law dependence on hydrogel concentration. Previous work has indicated that the elasticity of hydrogels is proportional to the square of the concentration, while other studies have shown the power-law exponent to vary depending on the type of hydrogel [35, 36]. To determine the power-law behavior of both E and η for the PEGDA hydrogels, the experimental AFM data was fitted in a least-squares fashion for a range of exponents. Coefficient of determination (R^2) was used to determine goodness of fit, and the exponent with maximum goodness of fit was chosen and the corresponding coefficient was recorded. For E, the values found were: $a = 2.16$ and $E_0 = 7.54MPa$ ($R^2 = 0.9904$). For η, the values found were: $b = 2.01$ and

$\eta_0 = 108.74$ mPa·s ($R^2 = 0.9883$).

Nanogram-scale hydrogel samples were integrated onto the resonant microsensors using e-jet printing, which is advantageous in its superior resolution to conventional printing techniques [22, 37]. Figure 4.3A shows the e-jet printing procedure, which uses electric fields to print small volumes of liquid onto a substrate with precision placement. The electric field causes charge in the hydrogel solution to accumulate at the liquid surface. The Coulombic repulsion of the surface charge balances with surface tension causing the meniscus at the nozzle end to deform into a conical shape, called a Taylor cone. When the electric field exceeds a critical limit, the stress from the surface charge repulsion at the cone apex exceeds the surface tension and a droplet of fluid is emitted towards the grounded substrate. We deposited the pre-polymer as single droplets, with a predefined diameter and position, and immediately photopolymerized and stored the gels in DI water for equilibration. Figure 4.3B shows a differential interference contrast microscopy image of a deposited hydrogel structure on a sensor.

In order to determine the volume of the deposited hydrogel samples, we used confocal microscopy to image the fluorescently-coated (fluorescein isothiocyanate-conjugated poly-L-lysine) surface of the gel in water. Figure 4.3C shows an example of confocal images of the hydrogels, from which we estimated the volume of each structure using Amira 5.4.1 (Visualization Sciences Group; Mrignac, France). Figure 4.3D shows the gel volume reconstruction, which was performed by manually selecting the dark voxels on each slice and combining all processed slices to render the hydrogel volume. Multiplying the reconstructed volumes with the hydrogel density returned the volumetric mass for each hydrogel sample.

Following the deposition of hydrogels on the sensor platform, we measured the apparent mass of each structure with the resonant sensors and LDV system. This apparent mass is compared with the volumetric mass calculated using confocal microscopy, which we refer to as “actual” mass. Figure 4.4A shows the apparent mass and the actual mass for 5% and 10% gels with fitted slope lines, which describes the apparent mass ratio. As expected, the

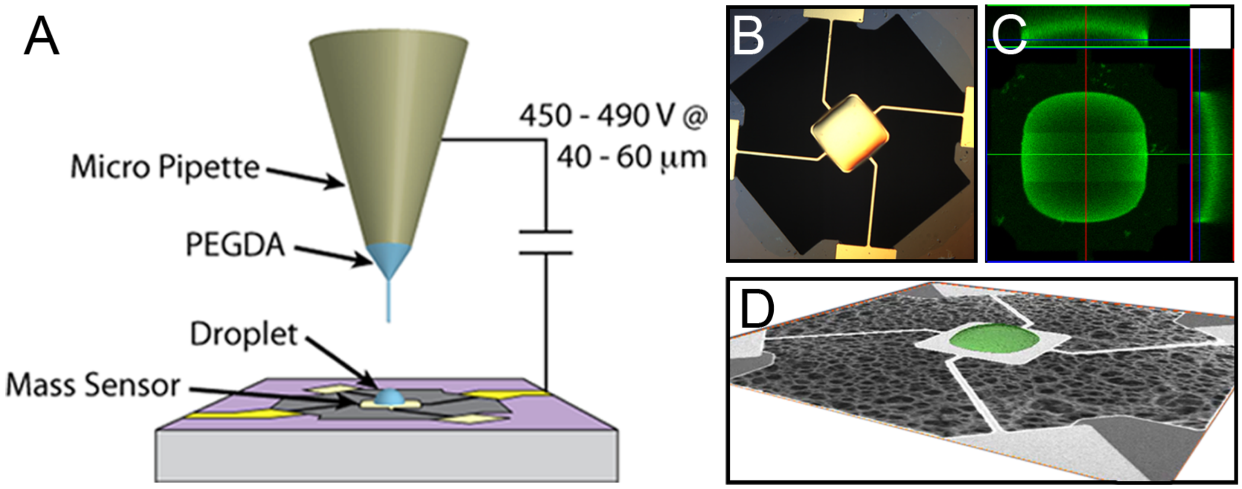

Figure 4.3: (A) Schematic of the electrohydrodynamic jet printing setup consisting of a micropipette coated with gold-palladium attached to a syringe with a variable back-pressure input. PEGDA hydrogels were deposited at a separation distance of 40-60 µm with base and peak voltages of 450V and 490V, respectively, and a 0.1% duty cycle. (B) Confocal image of the PEGDA structure on a sensor coated with poly-L-lysine. (C) Differential interference contrast image of PEGDA on a sensor. (D) Hydrogel volume reconstruction using Amira overlaid on SEM image of sensor.

apparent mass is not equal to the actual mass, with the 5% gels appearing less than actual and 10% gels appearing greater than actual. For hydrogels of higher concentration, the mass ratio was close to 1. The apparent mass ratio for each hydrogel concentration was 0.765, 1.112, 0.993, and 1.018 for the 5%, 10%, 15%, and 20% gels, respectively. These ratios highlight the strong dependence of apparent mass as measured by resonant sensors on the mechanical properties of the material, which is especially true for soft materials. As elastic modulus increases, the adhered sample behaves more like a point mass and the coupled oscillator effect is minimized, thus the resonant sensor returns the true mass.

Figure 4.4B shows a 2D contour view of the mass ratio predicted by the model for a range of elastic moduli and viscosities, with the locations of each gel percentage indicated by a red dot and a line indicating a cut through the measured points. Figure 4.4C shows the predicted values from the model along this line, as well as the experimental data points, which exhibit strong agreement with the model. These results indicate that the 2DOF model reliably captures the dependence of apparent mass ratio on viscoelastic properties of the material.

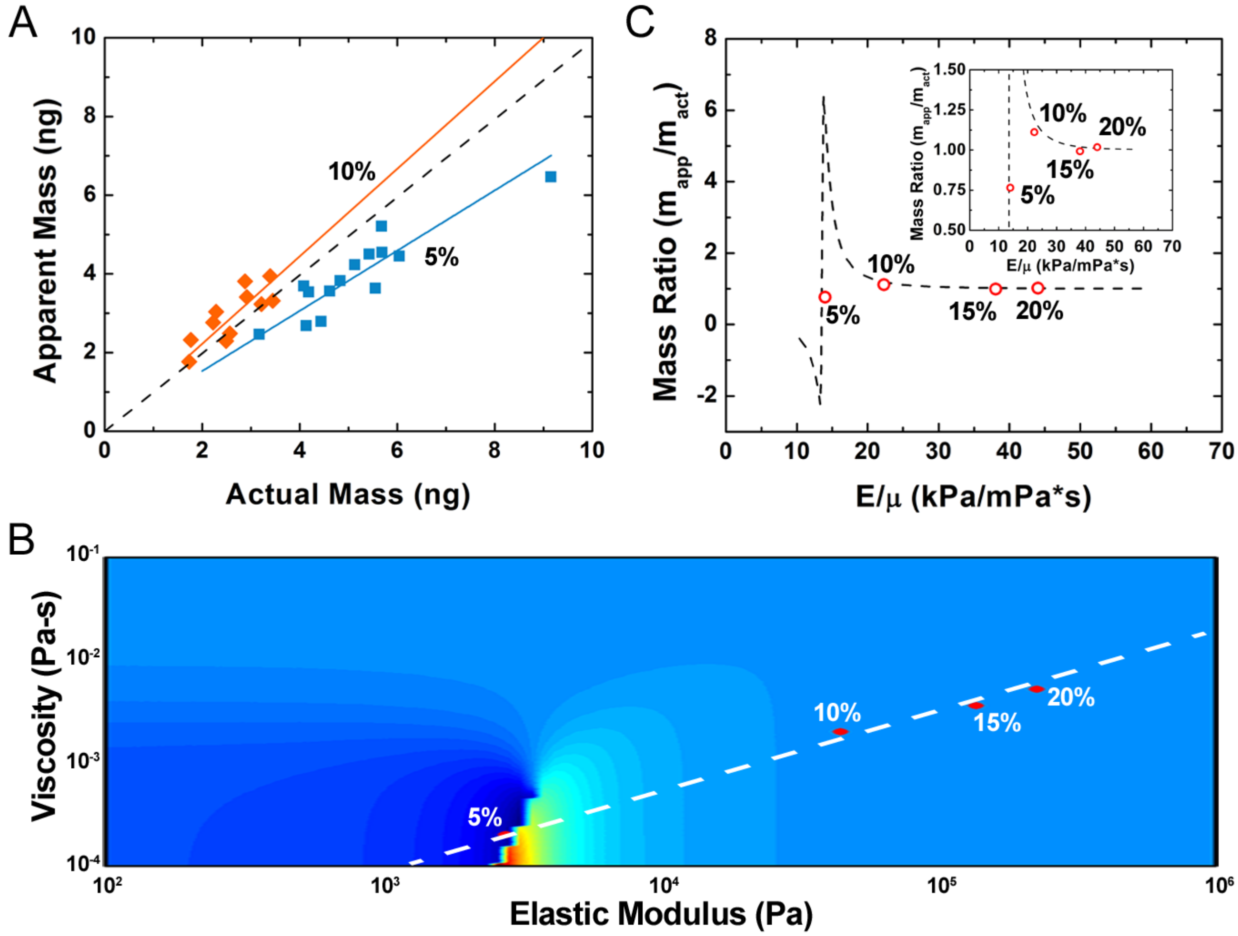

Figure 4.4: Results and comparison of the 2DOF model of a Kelvin-Voigt material adhered to the surface of a resonant sensor with the experimental data for the material viscoelasticity on the forced response of the system. (A) Comparison of the apparent mass as estimated from resonant frequency with the actual mass measured from confocal. (B) Top view of 3D model plot shows the locations of the experimental data (red dots) and the white line depicts the 2D slice chosen for figure (C). (C) Slice through the model plot showing the mass ratio from the model as a dotted line and the red dots as the experimental data, inset shows zoomed in plot showing good agreement of the data to the model.

The validated model can now be used for the inverse calculation of the hydrogel samples mechanical properties from the apparent mass measured from the sensor. The inverse calculation uses the mass ratio data of the apparent mass read by the sensor and the actual mass on the sensor. The calculation procedure uses the model to formulate an error term for each measured structure as a function of unknown elastic modulus and viscosity. By recognizing that the mechanical properties of hydrogels obey a power-law dependence on concentration, we were able to simultaneously solve for power-law coefficients and exponents for both elastic modulus and viscosity using all samples together. These power-law values extracted from AFM data are the initial guesses for the iterative property estimation procedure.

Figure 4.5 presents the elastic moduli and viscosities measured with AFM along with the power-law behavior estimated with the resonant sensors this technique. The estimated power-law exponent is 2.07 and power-law coefficient is 8.37 MPa for elastic modulus. The estimated elastic moduli of the hydrogels are somewhat higher than the values measured with AFM, though they still show very good agreement ($R^2 = 0.7783$) and are consistent with previous work on PEGDA MW 575 g·mol^{-1} hydrogels. [38] For viscosity, the estimated power-law exponent is 1.90 and power-law coefficient is 88.83 mPa·s, and this behavior exhibited excellent agreement with AFM data ($R^2 = 0.9867$).

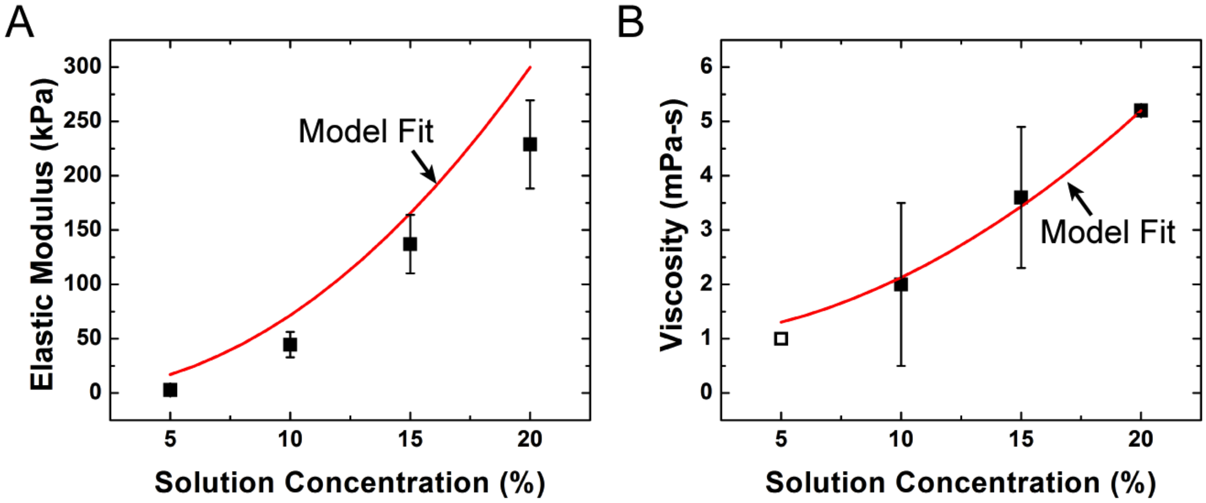

Figure 4.5: The viscoelastic properties of hydrogels generally exhibit a power-law dependence on polymer concentration. (A) The predicted power-law fit is plotted alongside the experimental data for the elastic modulus. (B) The predicted power-law fit is plotted alongside the experimental data for the viscosity.

4.4 Conclusion

In this work, we have demonstrated the feasibility of using MEMS resonant sensors in estimating the viscoelastic properties of hydrogel microstructures. The technique described here exploits the dependence of the resonance condition of resonant sensors on the mechanical properties of the adhered material. We modeled this dependence through the use of a Kelvin-Voigt 2DOF model, which was shown to accurately predict the experimental behavior. By examining hydrogel microstructures with micromechanical properties varied through polymer concentration, we were able to calculate the power-law behavior of both elasticity and viscosity. These calculated values exhibited excellent agreement with independent measurements using AFM techniques. Ultimately, we have presented a new technique for quantifying the viscoelasticity of nanogram-scale hydrogel structures. This technique was performed in an aqueous environment and may overcome limitations of other techniques, such as dependence on AFM probe characteristics and QCM electrode size. The microscopic lab-on-chip format allows us to explore hydrogel samples on the scale of individual cells, and this technique may be expanded in the future to study the mechanical properties of other biological materials.

4.5 References

[1] Y. Liang, J. Jeong, R. J. DeVolder, C. Cha, and F. Wang. ScienceDirect.com - Biomaterials - A cell-instructive hydrogel to regulate malignancy of 3D tumor spheroids with matrix rigidity. *Biomaterials*, 2011.

[2] Y. M. Kolambkar, K. M. Dupont, J. D. Boerckel, N. Huebsch, D. J. Mooney, D. W. Hutmacher, and R. E. Guldberg. An alginate-based hybrid system for growth factor delivery in the functional repair of large bone defects. *Biomaterials*, 32(1):65–74, 2011.

[3] G. D. Nicodemus and S. J. Bryant. Cell Encapsulation in Biodegradable Hydrogels for Tissue Engineering Applications. *Tissue Engineering Part B: Reviews*, 14(2):149–165, 2008.

[4] J. L. Drury and D. J. Mooney. Hydrogels for tissue engineering: scaffold design variables and applications. *Biomaterials*, 24(24):4337–4351, 2003.

[5] K. S. Anseth, C. N. Bowman, and L. Brannon-Peppas. Mechanical properties of hydrogels and their experimental determination. *Biomaterials*, 17(17):1647–1657, 1996.

[6] N. A. Peppas, J. Z. Hilt, A. Khademhosseini, and R. Langer. Hydrogels in Biology and Medicine: From Molecular Principles to Bionanotechnology. *Advanced Materials*, 18(11):1345–1360, 2006.

[7] D. H. Kim, P. K. Wong, J. Park, A. Levchenko, and Y. Sun. Microengineered Platforms for Cell Mechanobiology. *Annual Review of Biomedical Engineering*, 11(1):203–233, 2009.

[8] J. Yoon, S. Cai, Z. Suo, and R. C. Hayward. Poroelastic swelling kinetics of thin hydrogel layers: comparison of theory and experiment. *Soft Matter*, 6(23):6004, 2010.

[9] J. H. Jeong, V. Chan, C. Cha, P. Zorlutuna, C. Dyck, K. Hsia, R. Bashir, and H. Kong. “Living” microvascular stamp for patterning of functional neovessels; orchestrated control of matrix property and geometry. *Advanced Materials*, 24(1):58–+, 2012.

[10] V. Chan, P. Zorlutuna, J. H. Jeong, H. Kong, and R. Bashir. Three-dimensional photopatterning of hydrogels using stereolithography for long-term cell encapsulation. *Lab On A Chip*, 10(16):2062, 2010.

[11] E. A. Phelps, N. Landazuri, P. M. Thule, W. R. Taylor, and A. J. Garcia. Bioartificial matrices for therapeutic vascularization. *Proceedings of the National Academy of Sciences USA*, 107(8):3323–3328, 2010.

[12] B. V. Slaughter, S. S. Khurshid, O. Z. Fisher, A. Khademhosseini, and N. A Peppas. Hydrogels in Regenerative Medicine. *Advanced Materials*, 21(32-33):3307–3329, 2009.

[13] T. A. Ulrich, E. M. de Juan Pardo, and S. Kumar. The Mechanical Rigidity of the Extracellular Matrix Regulates the Structure, Motility, and Proliferation of Glioma Cells. *Cancer Research*, 2009.

[14] I. Sack, G. Buntkowsky, J. Bernarding, and J. Braun. Magnetic Resonance Elastography: A Method for the Noninvasive and Spatially Resolved Observation of Phase Transitions in Gels. *Journal of the American Chemical Society*, 123(44):11087–11088, 2001.

[15] N. E. Kurland, Z. Drira, and V. K. Yadavalli. Measurement of nanomechanical properties of biomolecules using atomic force microscopy. *Micron*, 43(2-3):116–128, 2012.

[16] J. Lee, J. Jang, D. Akin, C. A. Savran, and R. Bashir. Real-time detection of airborne viruses on a mass-sensitive device. *Applied Physics Letters*, 93(1):013901, 2008.

[17] A. Gupta, D. Akin, and R. Bashir. Detection of bacterial cells and antibodies using surface micromachined thin silicon cantilever resonators. *Journal of Vacuum Science & Technology B*, 22(6):2785–2791, 2004.

[18] K. Park, L. J. Millet, N. Kim, H. Li, X. Jin, G. Popescu, N. R. Aluru, K. Hsia, and R. Bashir. Measurement of adherent cell mass and growth. *Proceedings of the National Academy of Sciences USA*, 107(48):20691–20696, 2010.

[19] T. P. Burg, M. Godin, S. M. Knudsen, W. Shen, G. Carlson, J. S. Foster, K. Babcock, and S. R. Manalis. Weighing of biomolecules, single cells and single nanoparticles in fluid. *Nature*, 446(7139):1066–1069, 2007.

[20] K. Park, J. Jang, D. Irimia, J. Sturgis, J. Lee, J. P. Robinson, M. Toner, and Rashid Bashir. 'Living cantilever arrays' for characterization of mass of single live cells in fluids. *Lab On A Chip*, 8(7):1034–1041, 2008.

[21] L. J. Millet, E. A. Corbin, R. Free, K. Park, H. Kong, W. P. King, and R. Bashir. Characterization of Mass and Swelling of Hydrogel Microstructures using MEMS Resonant Mass Sensor Arrays. *Small*, 8(16):2555–2562, 2012.

[22] J. Park, M. Hardy, S. J. Kang, K. Barton, K. Adair, D. K. Mukhopadhyay, C. Y. Lee, M. S. Strano, A. G. Alleyne, J. G. Georgiadis, P. M. Ferreira, and J. A. Rogers. High-resolution electrohydrodynamic jet printing. *Nature Materials*, 6(10):782–789, 2007.

[23] S. Nemir, H. N. Hayenga, and J. L. West. PEGDA hydrogels with patterned elasticity: Novel tools for the study of cell response to substrate rigidity. *Biotechnology and Bioengineering*, 105(3):636–644, 2010.

[24] B. Dorvel, B. Reddy, I. Block, P. Mathias, S. E. Clare, B. Cunningham, D. E. Bergstrom, and R. Bashir. Vapor-Phase Deposition of Monofunctional Alkoxysilanes for Sub-Nanometer-Level Biointerfacing on Silicon Oxide Surfaces. *Advanced Functional Materials*, 20(1):87–95, 2010.

[25] H. Jo and F. D. Blum. Structure and Adsorption of 3-acryloxypropyltrimethoxysilane. *Langmuir*, 15(7):2444–2449, 1999.

[26] U. Chippada. Non-Intrusive Characterization of Properties of Hydrogels. *PhD Dissertation*, pages 1–174, 2009.

[27] J. M. Gere. *Mechanics of Materials*. PWS Pub Co., Boston, MA, 1997.

[28] K. Park, N. Kim, D. T. Morisette, N. R. Aluru, and R. Bashir. Resonant MEMS Mass Sensors for Measurement of Microdroplet Evaporation. *Journal of Microelectromechanical Systems*, 21(3):702–711, 2012.

[29] Y. C. Fung. *Biomechanics: Mechanical Properties of Living Tissues*. Springer-Verlag, New York City, NY, 1981.

[30] A. J. Engler, F. Rehfeldt, S. Sen, and D. E. Discher. Microtissue elasticity: measurements by atomic force microscopy and its influence on cell differentiation. *Methods in Cell Biology*, 83:521–545, 2007.

[31] Q. S. Li, G. Y. H. Lee, C. N. Ong, and C. T. Lim. AFM indentation study of breast cancer cells. *Biochemical and Biophysical Research Communications*, 374:609–613, 2008.

[32] S. Nawaz, P. Sánchez, K. Bodensiek, S. Li, and M. Simons. PLOS ONE: Cell Visco-Elasticity Measured with AFM and Optical Trapping at Sub-Micrometer Deformations. *PLoS ONE*, 2012.

[33] E. A-Hassan, W. F. Heinz, M. D. Antonik, N. P. D'costa, S. Nageswaran, C. A. Schoenenberger, and J. H. Hoh. Relative Microelastic Mapping of Living Cells by Atomic Force Microscopy. *Biophysical Journal*, 74(3):1564–1578, 2008.

[34] V. Vadillo-Rodriguez, S. R. Schooling, and J. R. Dutcher. In Situ Characterization of Differences in the Viscoelastic Response of Individual Gram-Negative and Gram-Positive Bacterial Cells. *Journal of Bacteriology*, 191(17):5518–5525, 2009.

[35] H. J. Kong, E. Wong, and D. J. Mooney. Independent Control of Rigidity and Toughness of Polymeric Hydrogels - Macromolecules (ACS Publications). *Macromolecules*, 2003.

[36] V. Normand, D. L. Lootens, E. Amici, K. P. Plucknett, and P. Aymard. New Insight into Agarose Gel Mechanical Properties. *Biomacromolecules*, 1(4):730–738, 2000.

[37] J. Pikul, P. Graf, S. Mishra, K. Barton, Y. Kim, J. Rogers, A. Alleyne, P. Ferreira, and W. King. High precision electrohydrodynamic printing of polymer onto microcantilever sensors. *Sensors Journal, IEEE*, (99):1–1.

[38] T. Keim and K. Gall. Synthesis, characterization, and cyclic stress-influenced degradation of a poly(ethylene glycol)-based poly(beta-amino ester). *Journal of Biomedical Materials Research*, 92A(2):702–711, 2010.

Chapter 5

Measuring Physical Properties of Neuronal and Glial Cells with Resonant Microsensors

Microelectromechanical systems (MEMS) resonant sensors provide a high degree of accuracy for measuring the mass of physical, chemical, and biological samples. These sensors enable the investigation of cellular mass and growth rate, though previous sensor designs have been limited to the study of homogeneous cell populations. This paper presents a MEMS resonant pedestal sensor array having backside pores compatible with vertical flow fields to increase measurement versatility (e.g. fluidic manipulation and throughput) and allow for the measurement of heterogeneous cell populations. Overall, the improved sensor increases capture by 100% at flow rate of 2 µL/min, as characterized through micro-bead experiments, while maintaining measurement accuracy. Measurement of the mass of primary mouse hippocampal neurons *in vitro*, in the range of 0.1-0.9 ng, demonstrates the ability to investigate neuronal mass and changes in mass over time.

5.1 Introduction

Microelectromechanical systems (MEMS) can accelerate biological and medical research by introducing quantitative measurement devices capable of simultaneously handling, manipulating, and characterizing individual cells [1]. The desire to study the growth of individual cells has driven the development of cantilever [2], suspended micro-channel [3–5], and pedestal [6, 7] resonant sensors, which measure the mass of captured objects through the shift in device resonant frequency. Studies of yeast [4], human colon cancer cells (HT29) [6], cervical cancer cells (HeLa) [2], and bacterial cells [8] demonstrated that MEMS resonant mass sensors are effective tools for measuring cellular growth rates. Recently, we extended the use of MEMS resonant sensors for the characterization of micro-scale hydrogel structures for tissue engineering applications [9, 10].

While cell lines are the population of choice for many cell biology studies, tissue-derived (primary source) cultures are a mainstay for post-mitotic cell populations. The process of generating primary, post-mitotic neurons in culture yields a highly mixed cellular population, which presents additional challenges for single-cell studies. While microfluidic systems can be used to enrich some primary cellular populations of interest [11], neuronal cells are enriched through chemical means during the culture process using defined media formulations. For over a century, numerous culture devices and methods have provided ideal microenvironments to glean insights into neuronal development [12, 13]; MEMS sensor arrays [6, 14] potentially provide a unique advantage for measuring the growth of neurons, if neurons can be isolated from the heterogeneous population. By minimizing the inherent limitations associated with selecting few cells out of large heterogeneous populations, MEMS resonant sensors may further aid the understanding of cellular developmental processes by measuring the mass and growth dynamics of individual neuron cells.

The reduced measurement yield of the defined-media selection process is exacerbated by the potential for capturing cells on the beam springs of the pedestal sensors. The presence of objects on the springs alters the effective spring constant of the sensor and invalidates the measurement. The stochastic process of random cell seeding in static fluid domains provides a finite limit to the yield; we define sensor yield as the number of functional sensors with appropriately captured objects that provide accurate and reliable measurements. To improve the efficiency of our MEMS mass sensor array for heterogeneous populations, we redesigned the fabrication process to incorporate vertical flow fields and on-chip microfluidic channels that remove cells from the sensor springs to increase sensor yield and enable high throughput growth studies.

This paper reports the design, fabrication, and characterization of a MEMS resonant mass sensor array where each sensor is suspended over a vertical microfluidic channel etched through the entire silicon wafer. An additional PDMS-based microfluidic perfusion chamber and a backside drainage chamber constitute an on-chip microfluidic system and provide increased functionality. We demonstrate the feasibility of improved capture efficiency through finite element flow simulations and micro-bead capture experiments. We show that the vertical flow pedestal sensors retain the native functionality of the original, non-flow sensors, and use them to measure the mass and growth of mouse primary hippocampal neurons *in vitro*.

5.2 Materials and Methods

5.2.1 Fabrication of Vertical Flow MEMS Resonant Sensor arrays

Figure 5.1 illustrates the key steps of the fabrication process, which are outlined here. The starting material was a silicon-on-insulator (SOI) wafer with a 2 µm thick silicon device layer, a 0.6 µm buried oxide (BOX) layer, and a 500 µm silicon handle layer as depicted in Figure 5.1A. First, we grew a passivation layer of silicon dioxide (25 nm) using thermal oxidation. After deposition of the passivation layer (Figure 5.1B), a photolithography process patterned the square pedestals and beam springs. Then, 10 nm of chromium and 50 nm of gold were deposited using thermal evaporation and patterned with a liftoff process. Figure 5.1C shows the device after the first liftoff process. Once the devices are defined, a photoresist etch mask is patterned by photolithography along with the first metal layer to create the sensor areas. An inductively coupled plasma (ICP) etcher formed the springs and the platform using the Bosch process, which etched the exposed silicon until it stops at the BOX layer (Figure 5.1D). A second photolithography patterned the electrodes for connecting the finished devices to printed circuit boards. E-beam evaporation deposited another 100 nm of chromium and 900 nm of gold, which were also patterned through liftoff. Figure 5.1E shows the resulting metallization of the electrodes, which allows the bias current to flow through a single row of devices at one time.

Fabrication of the backside pore began after metallization. Photolithographic patterning of the wafer backside followed by an ICP etch, again using the Bosch process, removed the 500 µm silicon handle layer from beneath the platform sensor (Figure 5.1F). As a result, microfluidic pores with smooth vertical sidewalls were formed in the wafer beneath the sensor structure to permit fluid transport. Next, a buffered oxide etch (BOE) removed the BOX layer, suspending the devices over the backside pore (Figures 5.1G-J). The final fabrication step deposited a 100 nm silicon dioxide layer for insulation using plasma enhanced chemical vapor deposition (PECVD) process. Prior to wire-bonding the resulting chip to a printed circuit board, we selectively etched the PECVD oxide on the bonding pads with BOE.

5.2.2 Perfusion Chamber Fabrication and Assembly

Figure 5.2A depicts the on-chip microfluidic system that includes a microfluidic perfusion layer made of Poly(dimethylsiloxane) (PDMS) that receives flow from a syringe pump at a controlled rate during cell capture. The perfusion layer divides the applied fluid through bilaterally symmetric branching channels to the sensor array, and Figure 5.2B presents the design of the microfluidic channels.

Fabrication of the microfluidic distributive channel perfusion layer started with creation of a negative mold of the desired channels using SU-8 50 photoresist (Microchem; Newton, MA). SU-8 50 was spun on a 4 inch silicon wafer to a height of 50 µm, and was pre-baked in two steps: 10 min at 65 °C and then 30 min at 95 °C. The wafer was exposed to a mask defining the fluidic channels, creating the negative mold, followed by a two-step post-exposure bake: 1 min at 65 °C and then 10 min at 95 °C. The resulting mold is developed in SU-8 developer for 2 min at room temperature, rinsed with isopropyl alcohol, and hard-

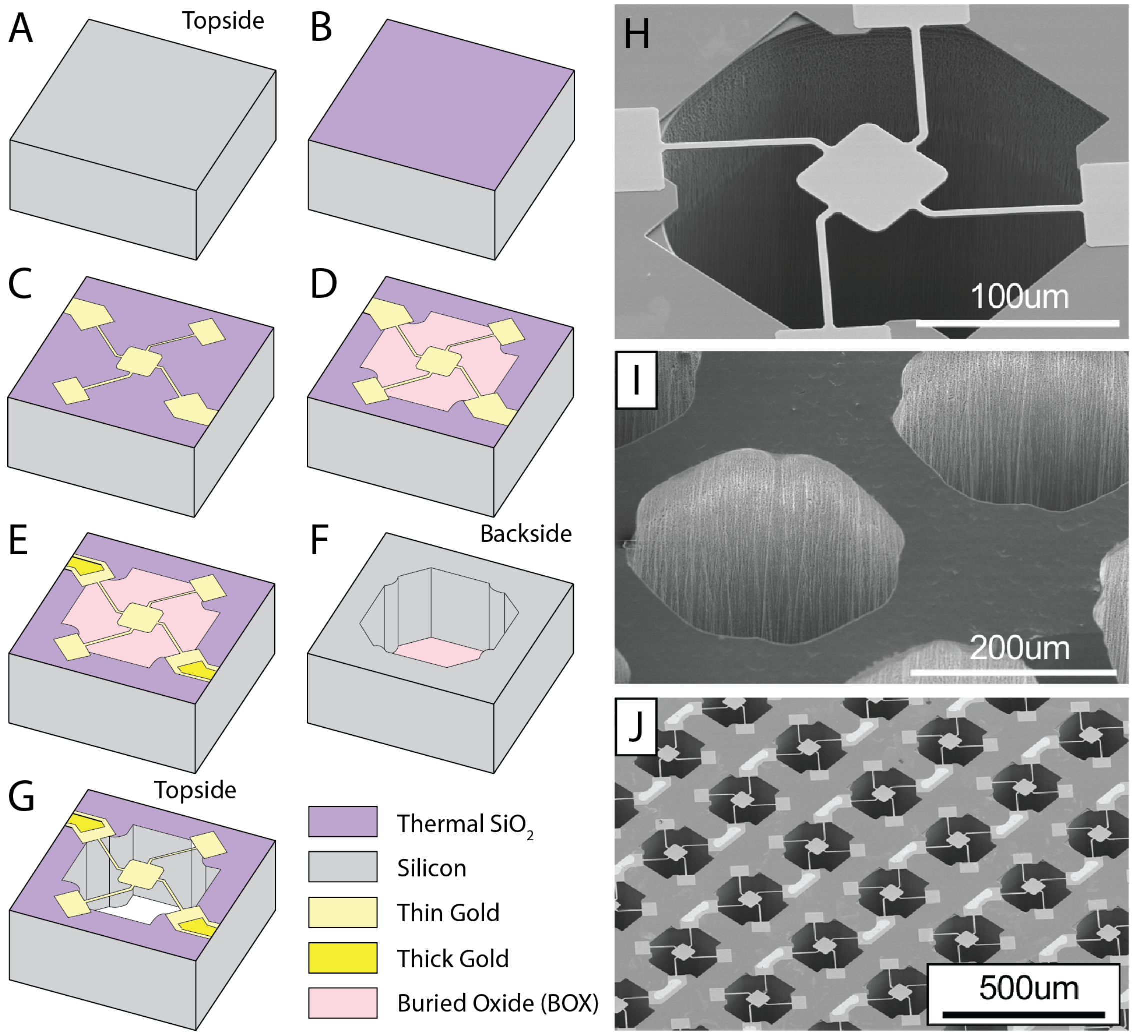

Figure 5.1: Fabrication process for vertical flow MEMS mass sensor with backside pore. (A) Silicon-on-insulator (SOI) wafer (2 μm silicon device layer with 0.6 μm buried oxide (BOX) layer). (B) 25 nm silicon dioxide layer for electrical passivation. (C) Patterned metallization (Cr and Au) of sensor pedestals and beam springs. (D) Photoresist etch mask for etching silicon through the device layer down to the BOX. (E) Second metallization (Cr and Au) to define the electrodes. (F) Backside photolithography and subsequent etching BOX produces backside pores with smooth vertical sidewalls. (G) Etch for oxide removal to release the devices and suspend them over the backside pore. Scanning electron microscope (SEM) images of the resonant mass sensor array: (H) single sensor with a backside pore to permit vertical fluid flow; (I) backside view of the pore; (J) array of 81 sensors.

baked at 125 °C for 15 min. PDMS, at a ratio of 1:10 curing agent to base, was poured over the negative mold, degassed, and allowed to cure overnight at 70 °C. Individual perfusion layers were cut from the polymerized PDMS, and a “corner punch” technique created all inlets and outlets.

Figure 5.2C depicts the corner punch used to anchor the microfluidic tubing and supply fluid through the microchannels. The microfluidic perfusion layer was first punctured from the patterned side with a 1 mm dermal biopsy punch, creating a vertical channel at the patterned inlet with a depth of half the PDMS thickness. The second channel is created in a single, angle-changing motion that starts from the side to meet the vertical channel using the same 1 mm biopsy punch while slightly deforming the PDMS to expel the material punched from both channels. A PDMS thin film is covalently bonded to the patterned piece thus creating a sealed, embedded channel. The PDMS layers are bonded through oxygen plasma activation in a barrel etcher followed by placement on a hot plate at 70 °C for 15 min. A 6 mm dermal biopsy punch is then pressed through the 4 mm thick PDMS microfluidic system to define the culture chamber and open the microfluidics into the culture well (Figure 5.2D). Finally, the PDMS-based wellwith embedded microfluidicsis sealed to the MEMS sensor array following oxygen plasma activation, alignment, and heating (Figure 5.2E-F). PTFE ultramicrobore tubing (Cole-Parmer; Vernon Hills, IL) makes fluidic connections between the chip and syringe pumps; the curvature of the corner punch assists in retaining the tubing in place while providing a good seal (Figure 5.2E-F). A Harvard Apparatus PicoPlus syringe pump (Holliston, MA) delivers constant stream of fluid into the system through a T-connector to split the flow for equal distribution to both fluidic inlets.

5.2.3 Fluid Flow Modeling

We modeled the velocity characteristics of the flow around the sensor and through the backside pore using the finite element method (FEM). Simulation of steady-state incompressible flow in the system used the Navier-Stokes equations and the geometry of a single sensor and

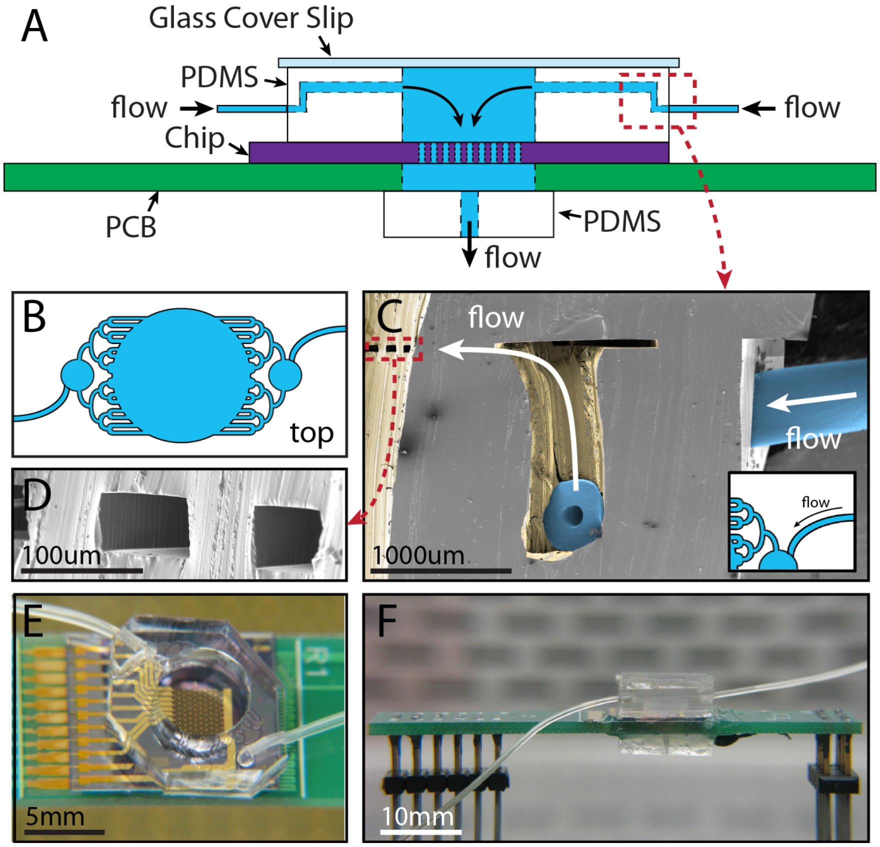

Figure 5.2: Complete chip assembly with microfluidics and fluidic flow description. (A) Schematic of assembled chip showing the PDMS-based microfluidic perfusion layer on chip containing sensor arrays that allow vertical flow through backside pore. The microfluidic perfusion layer includes distributed microfluidic channels that deliver fluid to the 6 mm culture well and the MEMS sensor array to remove cells from springs and increase capture efficiency and sensor yield. (B) Schematic of channel architecture for PDMS-based microfluidic perfusion layer (top-down view) designed to distribute incoming fluid from a syringe pump across the sensor array. (C) Scanning electron microscope (SEM) image of the microfluidic-tubing interface and channel openings into the culture well for the section of perfusion layer highlighted in the inset. Due to physical space requirements between the optics and temperature control chamber, a tri-axial hole is made with the “corner punch” technique to interface the tubing (blue) with the of PDMS-bilayer microfluidics; fluid cavities are colored yellow. (D) Magnified SEM image of microfluidic channel openings for fluid infusion into the culture well from the tubing and syringe pump. (E) Top view and (F) side view images of the fully assembled chip with the microfluidic layer, perfusion tubing, and PDMS-based outlet drain beneath the PCB.

channel in COMSOL Multiphysics 3.5a (COMSOL; Burlington, MA). Boundary conditions for the incompressible Navier-Stokes equations included: no slip at the interface with pore walls and the sensor, a set velocity uniform across the inlet, and a zero pressure condition at the outlet with no viscous stress. We computed velocity fields for three flow rates: 2, 4, and 8 µL/min. This rate of total flow delivered to all sensors was converted to velocity at the inlet of each individual channel, assuming even distribution between sensors and a uniform velocity at the inlet.

5.2.4 Capture Efficiency Characterization

We characterized the capture efficiency of the vertical flow sensor and compared with the previous generation of sensor design, which included platforms suspended over shallow pits without microfluidics for cell measurements in a 100 µL static well. We will refer to these older sensors as "pit" sensors throughout the rest of the text. Aqueous solutions of 15 µm polystyrene beads in phosphate buffered saline (PBS) with bead densities of 9,000 and 18,000 beads per 28 mm^2 area were evenly mixed and dispersed onto the sensor array. Beads in solution settled for 10 min prior to sealing the chamber with a glass coverslip. For each bead density, the syringe pump forced PBS through the PDMS microfluidic channel system for 30 min at the specified rate (2, 4, and 8 µL/min). For pit sensors, which receive no flow, beads settled in a static bath for 30 min. We monitored bead capture through images acquired with a Spot flex monochrome camera (Diagnostic Instruments; Sterling Heights, MI) attached to an Olympus BX51 upright fluorescent microscope (Olympus America Inc.; Center Valley, PA) at an acquisition rate of one image per minute for a 30 min capture period. We repeated the experiments three times for each flow rate and bead density, for a total of 24 experiments.

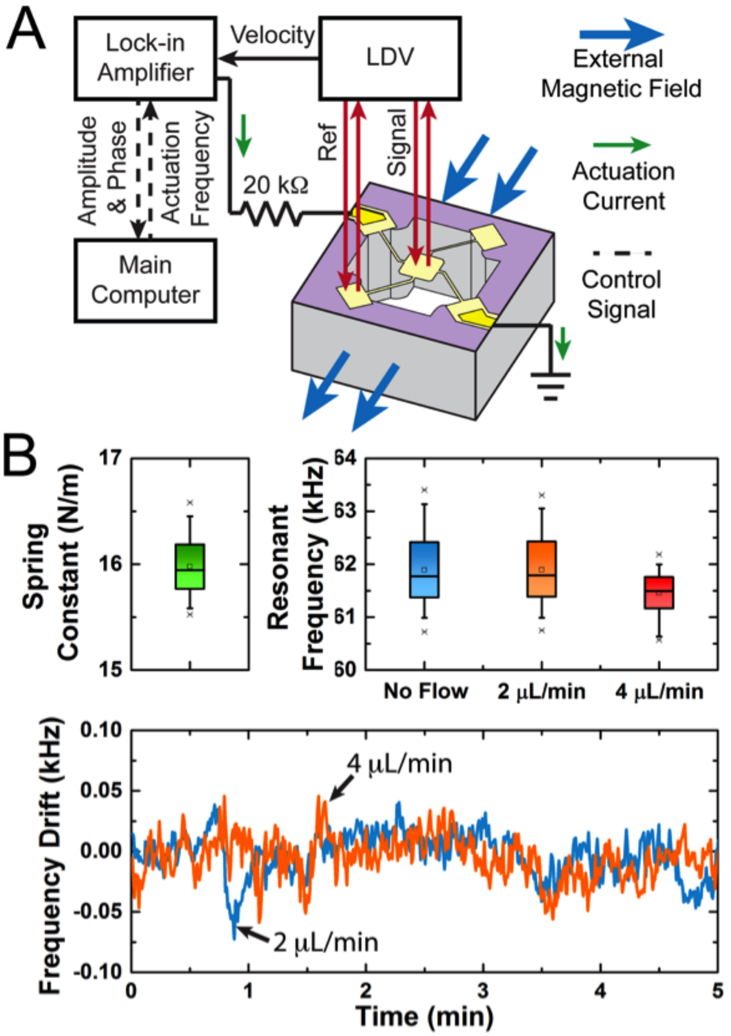

Figure 5.3: Operation and characterization of vertical flow resonant sensor array. (A) Overview of the mass measurement setup. The sensors are actuated using a bias current in a static magnetic field and a laser Doppler vibrometer system measures the relative phase between the input signal (current) and the platform response. Through iterative measurements, the resonant frequency of the platform is identified when the sensor vibration is in-phase with the current. In conjunction with the principle of frequency shift, this method permits the extraction of the mass on the platform. (B) Distribution of the sensor spring constant a sensor array fabricated with vertical flow channels; distribution of the sensor resonant frequency while submerged in fluid and subject to different applied flow rates; and the variation in sensor resonant frequency with flow applied. The tight spring constant range shows little variation in sensor characteristics over the chip array indicative of a high-precision microfabrication process. The sensor resonant frequency shows minimal change with the changing flow condition, and is very stable over time. These results demonstrate that the presence of applied flow will not affect the sensor performance for mass measurements.

5.2.5 Cell Culture and Mass Measurements

Following previously established protocols [15], we isolated cells from the enzymatically digested hippocampus of EGFP-actin mice (C57BL/6-Tg(CAG-EGFP)1Osb/J), Jackson Labs; Bar Harbor, ME). Mice were used in accordance with protocols established by the University of Illinois Institutional Animal Care and Use Committee and in accordance with all state and federal regulations. Cells were maintained in supplemented Hibernate-A or Neurobasal-A (Invitrogen; Carlsbad, CA) supplemented with 0.5 mM L-glutamine, Gem21 NeuroPlex ^{TM}(Gemini Bio-Products; West Sacramento, CA), 100 U/mL penicillin and 0.1 mg/mL streptomycin under standard culture conditions at 37 °C during growth measurements. Neurobasal and Hibernate are defined media formulations optimized for enriching neuronal growth at low densities and selecting against most mitotic cells [16, 17].

Mass measurement of cells relies on estimating the resonant frequency shift between empty and loaded sensors, a process that is well characterized [6, 7] and will only be briefly described here (Figure 5.3). Resonant frequency is determined through electromagnetic actuation of the sensors and concurrent velocity measurements with a laser Doppler vibrometer (LDV) system housed on a Zeiss Axiotech Vario upright microscope (Carl Zeiss AG; Jena, Germany). Prior to seeding the sensors with cells, two measurements are made on the empty sensors. First, the resonant frequency of each sensor in air is measured to determine the effective spring constant for each device, assuming negligible damping. Second, the resonant frequency of the sensors in cell culture media is measured to account for the change in resonant frequency from damping and hydrodynamic loading [18]. Finally, dissociated cells are seeded and captured onto the sensor array, and the resulting resonant frequencies of the sensors loaded with cells are measured. Measuring these frequencies allows for the extraction of the adhered mass of the cells on the platform from the final measured resonant frequency of the loaded sensors.

5.2.6 Volume Measurements and Immunocytochemistry

Following mass measurement, cells were fixed (4% paraformaldehyde in PBS, 30 min) for volume estimation with confocal microscopy and cellular identification through immunocytochemistry. The volume of measured cells was obtained using a Zeiss LSM 700 laser scanning confocal microscope using an Argon laser (488 nm) and a Plan-Apochromat 20x/0.8 objective (Carl Zeiss Microscopy GmbH; Jena, Germany). Confocal image stacks (Z-stacks) with a 0.63×0.63×0.65 μm^3 voxel size were acquired for cell volume calculations using Amira 5.4.1 (Visualization Sciences Group; Mrignac, France).

Cellular identities of neurons were achieved using immunocytochemistry. Cells on sensors were permeabilized with 0.25% Triton-X 100 in PBS for at least 5 min. Samples were blocked from non-specific antibody binding with 5% bovine serum albumin in PBS, followed by rabbit polyclonal primary antibody incubation for the neuronal marker microtubule associated protein-2 (MAP2) (1 hr, room temperature). Secondary antibody incubation (goat-anti rabbit, Alexa 568) was performed (1 hr, room temperature) prior to imaging with the Spot Flex camera on upright microscope.

5.3 Results and Discussion

We fabricated MEMS resonant pedestal mass sensors with vertical flow microfluidic pores etched through the wafer. This sensor array enables fluid exchange during mass measurements without interruption, thereby enabling a greater variety of studies. The on-chip microfluidic system allows for delivery of cells, culture media, and chemical agents to the cells on sensors, while providing a method for removing unwanted cells from the sensor springs to improve sensor measurement yield. Figure 5.1 shows scanning electron microscope (SEM) images of the fabricated sensor with a backside pore designed to accommodate constant fluid flow. Figure 5.1H shows a single sensor, which consists of a pedestal suspended by four beam springs over the backside pore. Etching completely through the wafer backside produces the pores (figure 5.1I) that constitute an on-chip microfluidic system when combined with a horizontal PDMS-based microfluidic perfusion layer (Figure 5.2). Each chip contains 81 sensors (arranged in a 9×9 array) for high measurement throughput (Figure 5.1J).

Cell mass measurements require operation of the sensors in the first resonance mode where the average platform vibrates vertically at 167.01 ± 10.21 kHz in-air and 67.70 ± 5.29 kHz in-liquid owing to an average spring constant of 18.47 ± 2.26 N/m (Figure 5.3). These values compare well with those of the previous generation "pit" sensor, which exhibited 152.44 ± 7.09 and 62.61 ± 3.37 kHz in-air and in-liquid resonant frequencies, respectively. The difference in resonant frequency between the vertical flow field sensors introduced here and the pit sensors is due to the variation in wafer and sensor layer thicknesses during manufacturing and microfabrication.

It is critical that the incorporation of flow exchange capabilities (sensor structure and flow fields) do not affect the sensor measurements. Mass is estimated through measurement of the device resonant frequency using an LDV system (Figure 5.3A). Figure 5.3B shows the range in spring constants of all mass sensors on a typical chip and their resonant frequencies at different flow rates. Essentially, there is no deviation (less than 1%) in the resonant frequency with applied flow rates of 2 and 4 µL/min compared with no flow resonant frequency. In comparison to our previous sensor arrays (frequency drift = 100-200 Hz/day) [6], Figure 5.3B shows that resonant frequency drift of the new sensor is similar (slope of drift is 80 Hz over 24 hr) in the presence of media flow at both 2 and 4 µL/min.

We performed simulations using finite element analysis to calculate and visualize the flow velocity profiles through the channel (Figure 5.4A). The fluid velocity around the sensor pedestal and springs is of particular interest since it will govern the cell capture characteristics. Modeling data shows a low velocity field above the pedestal sensor, which is also the cell attachment area, and this low velocity field appears to remain unaffected by media flow. In contrast, high velocity fields exist around the springs to deter cell attachment.

To understand the improvements in bead capture efficiency over the previous sensor

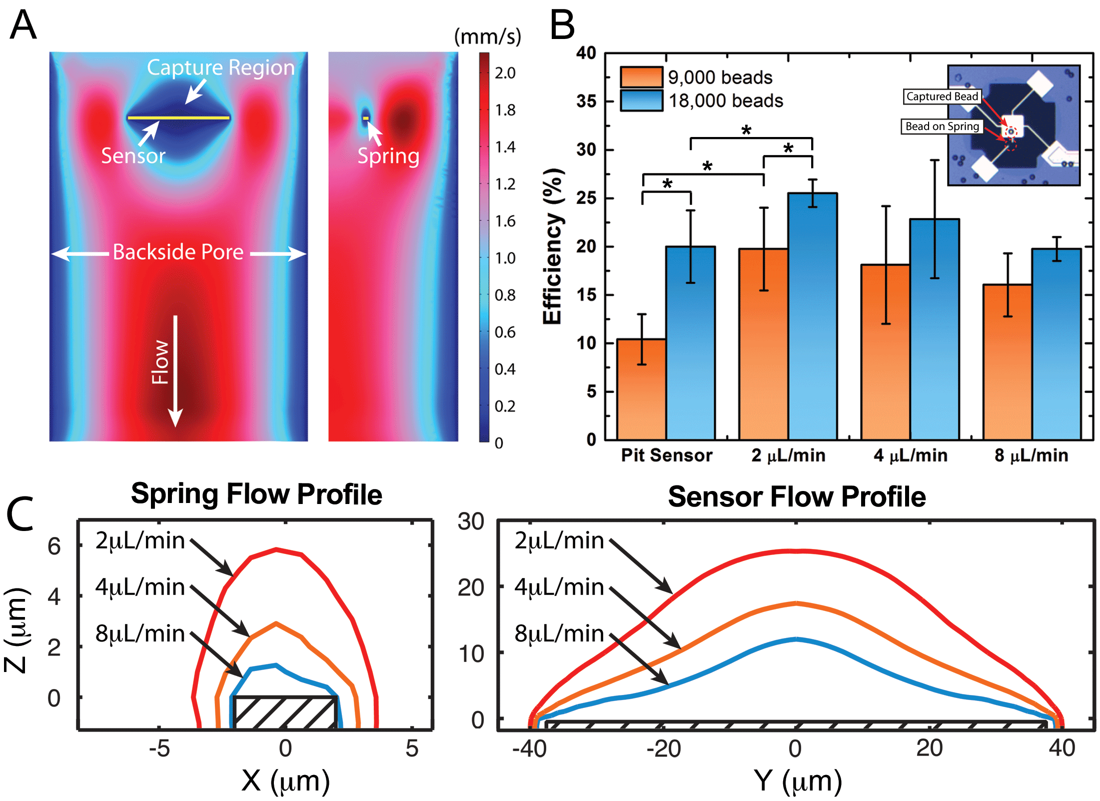

Figure 5.4: Fluidic modeling and experimental sensor capture efficiency. (A) Simulation of the microfluidic vertical flow field comprising the fluid-filled space and the MEMS sensor platform or spring (top of image). Flow direction is down through the backside pore. Images depict the fluid velocity field calculated for the 4 μL/min flow rate; low velocity areas (dark blue) around the sensor identify the targeted "capture region" above the pedestal where cells can be retained. (B) Experimental capture efficiency comparison of the no flow pit sensor with the vertical flow sensor, which show approximately 100% increase in capture efficiency; inset shows an example of beads captured on platforms and springs. (C) Simulation results of the capture region area/volume for the different applied flow rates from 2-8 μL/min on the springs (left) and the sensor (right). Tradeoffs exist between maximizing the capture region on the sensor and minimizing the capture region on the springs.

technology, we seeded beads on both new vertical flow sensors and on the pit sensor array (an array without flow capabilities). Figure 5.4B shows the capture efficiency of the beads on the pit sensor versus the flow sensor with various flow rates, along with an example image of a captured bead. Two-way ANOVA tested the dependence of capture efficiency on both seed density and flow rate. We found capture efficiency exhibits a statistical dependence on flow rate ($p = 0.016$), with a maximum occurring at 2 µL/min. There is also dependence on seed density ($p = 0.001$), with maximum capture efficiency at 18,000 beads per 28 mm^2 diameter.

Figure 5.4C shows "capture regions" around the springs and sensor defined by thresholding the simulated velocity field at 5 µm/s. These regions help explain why the maximum efficiency occurs at 2 µL/min and not at higher flow rates. The capture zone around the spring for the 2 µL/min suggests that an object larger than approximately 5 µm will be affected and prevented from settling on the springs. While the capture zone shrinks with higher flow rate, this will have no additional effect on the beads used in this experiment, which are 15 µm in diameter. However, the increased flow rate also reduces the capture region around the sensors. This will have the effect of dragging beads off the sensors, especially those not captured near the center.

In practice, the number of useable sensors with viable neurons is further reduced from the stochastic capture rate due to the presence of other cells in the sample. While the hippocampus is a structurally defined region of brain tissue that is easy to excise and dissociate for developmental studies of neuronal cells in vitro [19], the process of cellular extraction yields a mixed population of neurons, glial cells, microglia, and endothelial cells [17]. Defined media formulations have been produced to sustain neurons in culture, while selecting against non-neuronal and mitotic cell types [17]. In addition to a media-dependent population selection, neurons in culture develop at different rates dependent upon the stage of in situ cell development at the time of neuronal isolation [20]. Therefore, different maturation rates, or durations of 'time-to-polarization,' will also be observed.

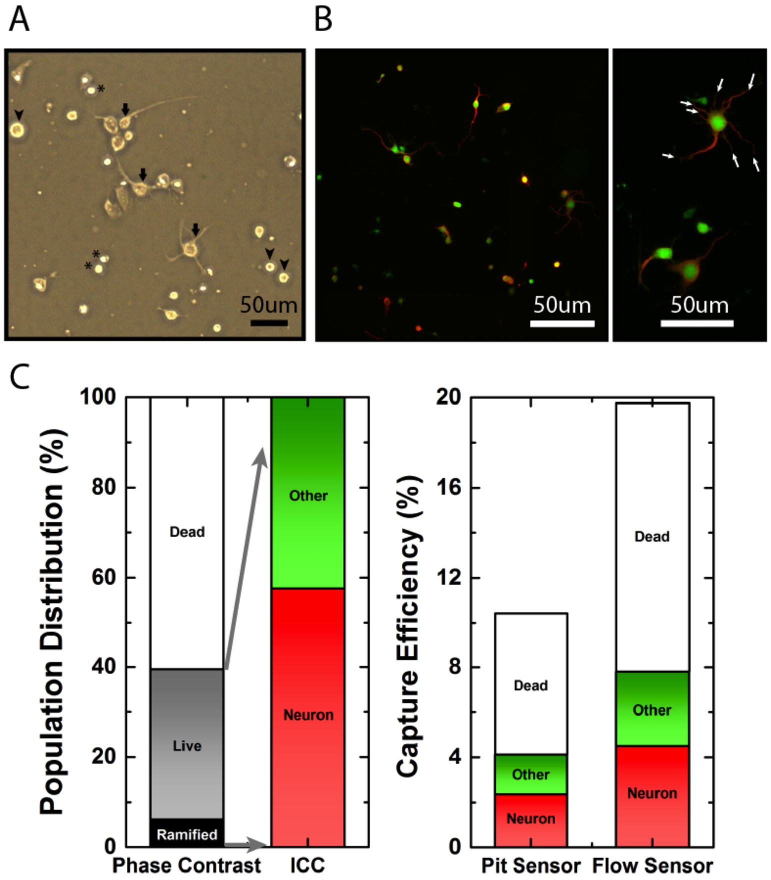

Figure 5.5: Cell capture analysis for heterogeneous populations of primary EGFP-transgenic mouse brain cells on MEMS resonant mass sensor arrays. (A) Phase contrast microscopy and (B) fluorescence microscopy images of fifteen-hour, age-matched cultures of EGFP-actin transgenic mouse primary hippocampal neurons in flasks and on silicon chips for population analysis. (C) Conditions provided by defined media formulations select for primary neurons, thus yielding a large portion of non-viable, non-neuronal cells [17]. Morphological analysis suggests that ∼60% of all captured cells will be shrunken dead cells, while ∼20% of the living cells (8% of total cells) will have ramified processes reminiscent of neuronal outgrowths (A). Characterization of the living cell population used immunocytochemistry since all brain cells express EGFP (green) under the actin promoter, though neurons are identified with MAP2 (red). After 15 hr in culture, ∼60% of the cells in the population are identified as neurons (MAP2, red), while non-neuronal cells (EGFP+, MAP2-) make-up the remaining ∼40% of the population (B). Multiplying primary neuron population characteristics with expected capture efficiency from microbead experiments, we predict that ∼7.5 sensors in vertical flow array will capture living cells, while only 3.2 sensors will have neuronal cells (C). By comparison, we predict that pit sensor arrays will capture a neuron on only 1.6 sensors corresponding to a 2% capture efficiency, half that of the 4% predicted capture efficiency of the flow sensors. In general, there is a very small chance of capturing a ramified neuron.

To better understand the probability of capturing neurons, particularly differentiating neurons, and their non-neuronal cellular counterparts, we performed morphometric and immunocytochemical analyses of age-matched cultures to characterize the cellular populations present in our experiments (Figure 5.5). From phase contrast imaging of the cell population in culture, we predict that living adherent cells (spherical or ramified) will be approximately 40% of all cells captured on the sensors in our studies, while approximately 20% of the living cells (8% of total cells) will have ramified processes reminiscent of neuronal growth after 15 hr in culture (Figure 5.5A). Further, immuno-cytochemical staining of the culture population revealed that neurons account for 60% of the living cells in culture, while the remaining 40% non-neuronal cells are expected to die off or remain quiescent before expanding in culture (Figure 5.5B) [21].

Figure 5.5C presents the predicted capture efficiency of neurons on the platform sensors, derived by multiplying the results from the observations in culture with the capture efficiency from the micro-bead experiments. The capture efficiency of neurons on pit sensors is estimated at ∼2%, while flow sensors appear to exhibit ∼4% capture efficiency. The micro-bead experiments simulated cell capture by substituting beads of similar size (15 µm diameter); however, cells have different geometry, buoyancy, adhesion, and viscoelasticity that can influence the efficiency of cellular retention on the sensors. For example, cell adhesiveness, a topic of intense research for decades [22–24], is cell and substrate dependent [25], therefore, cell capture dynamics will vary depending on the population under investigation. Flow modulation could also improve the enrichment of cells from mixed cell populations [26]. Experimental flow parameters will need to be optimized for adherent cells, with cell-type dependence, bearing in mind that flow velocity regions scale appropriately.

Dissociated cells from the mouse hippocampus were seeded on sensor arrays for mass measurements at a single time point. Cells were then fixed for immunolabeling and confocal microscopy to estimate cell volume. Figure 5.6A plots the cell mass and volume of each cell measured and marked by identified cell type. The slope of the linear fit indicates the density of the cells to be approximately 1.15 g/mL, which is similar to reported ranges for non-adherent murine lymphocytes and human erythrocytes [5].

We also repeated each mass measurement after fixation, and Figure 5.6B shows the comparison of measured mass before and after fixation. This type of fixation measurement was previously used to demonstrate how the apparent measured mass is a function of the viscoelasticity of the measured cell [6], with the measured mass of soft materials deviating from the actual mass. This apparent mass difference is explained by a two-degree-of-freedom (2DOF) dynamic system modeling the cell mass oscillating out-of-phase with the platform sensor (Figure 5.6C) [10]. This oscillation causes an additional resonant frequency shift and Figure 5.6D depicts how this changes the apparent mass based on material properties. Since fixation causes a significant stiffening of tissue [27, 28], it is expected that the apparent mass measured before and after fixation should not be the same. However, from the slope of the fit line in Figure 5.6B we observed an apparent mass ratio of approximately 1.05, which is lower than described in our previous study on a different cell type (human cancer cell line) [6]. While the previously reported neuron stiffness of 1 kPa [29] could produce a more significant deviation, it should be noted that the effective stiffness and damping ratio in Figures 5.6C-D depend not only on the material properties but also the shape of the object. Treating the cell as a cylinder and using the elastic modulus of 1 kPa and assuming a viscosity of 1 mPa-s, we explored how the low profile of the brain cells (Figure 5.6E) greatly affects the apparent mass ratio estimated from the fixation measurement (Figure 5.6F). As a cell gets shorter and wider, the apparent mass ratio approaches unity. The adherent cells investigated had a very high radius to height ratio (> 5), and thus the apparent mass exhibited only a small deviation from actual mass.

The prototypical neuronal marker MAP2 identifies somatodendritic structures of neurons. MAP2 immunolabeling is used to characterize hippocampal neurons of EGFP transgenic mice following mass measurement. Immature neurons differentiate by extending primary neurites, which then differentiate into an axon (longest process) and dendrites. While

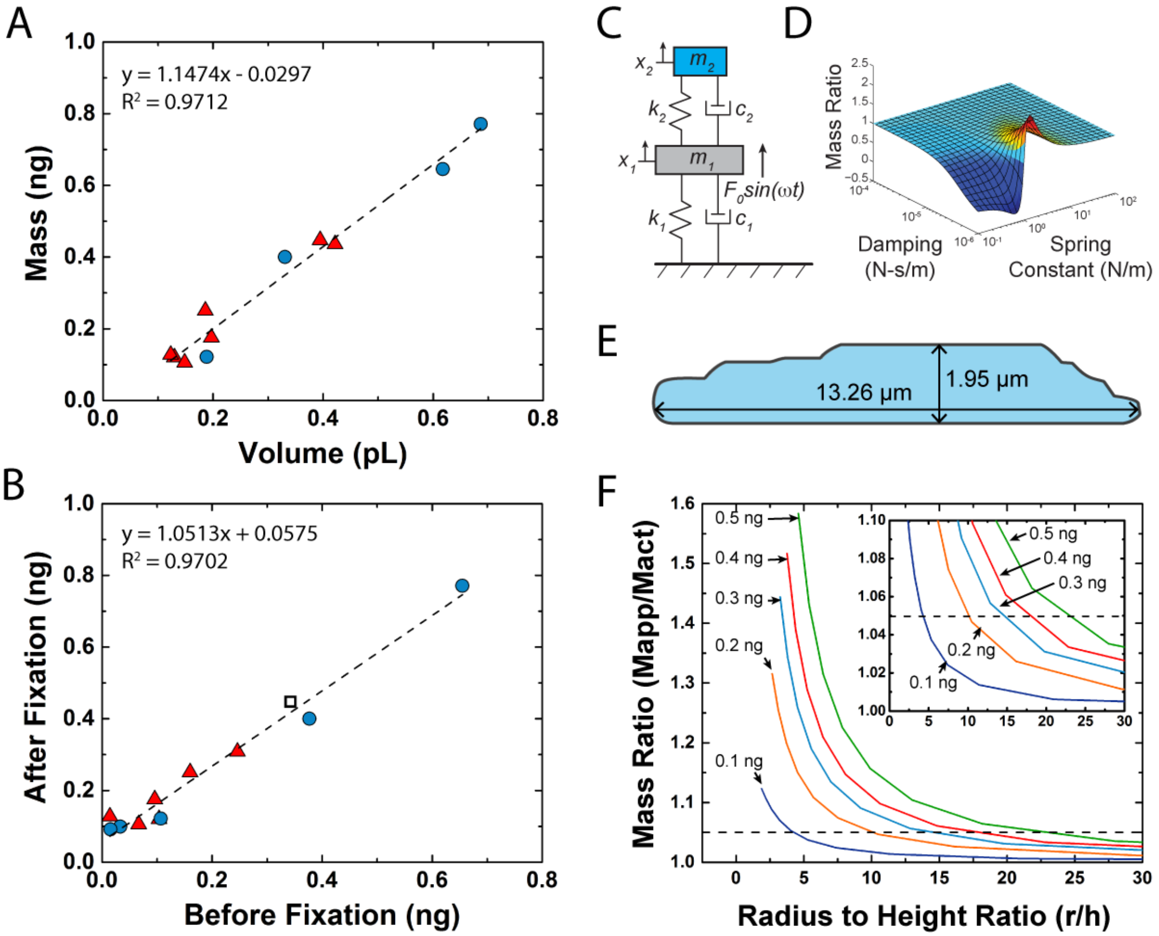

Figure 5.6: (A) The apparent mass of brain cells after fixation is 1.05 times greater than before fixation. (B) Mass of cells estimated with resonant sensors shows a strong linear relationship with estimates of cell volume obtained through confocal microscopy. Immature hippocampal neurons of EGFP transgenic mice on MEMS sensors can be identified by the prototypical early cellular morphology and immunochemistry for MAP2. Red triangles mark neuronal cells and blue circles mark non-neuronal cells, while an unidentifiable cell is indicated by an open square. (C) Schematic of dynamic model demonstrating the two-degree-of-freedom (2DOF) mass-spring-damper system. (D) An overview three-dimensional plot showing how stiffness and viscosity affect the result of the 2DOF system. (E) Cross-section of a neuron indicating the height and width values, which was reconstructed in Amira, a software package for 3D data visualization and analysis. (F) Shows the apparent mass from the sensor to the actual mass ratio and how that ratio is directly affected by the shape of the cell.

conventional culture protocols implement cell adhesion molecules for neuronal attachment, neurons show prototypical growth, differentiation, and adhesion on native silicon oxide surfaces. Figure 5.7A-I demonstrates that all stages of neuronal development are present on our chips and sensors. Even disconnected dendrites are observable in culture adhering to the sensor surface.

Finally, to demonstrate the functionality of this MEMS mass sensor array for investigating neuronal cell growth, we performed preliminary growth measurements of primary, dissociated postnatal mouse cells from the hippocampus of the EGFP-expressing transgenic mouse. Methods for culturing primary neurons in defined media render nearly pure neuronal populations at about 4 days in culture. Figure 5.7J shows a schematic representation of early prototypical neuronal growth and differentiation in vitro. Figure 5.7K shows growth profiles for 4 cells captured on the vertical flow MEMS sensor array. After initial seeding, non-neuronal mitotic cellswhich are abundant in primary culturesbegin to die off as neurons grow and differentiate. Two of the cells exhibit growth, while the remaining two cells show an abrupt mass decrease without recovery as early as seven hr in vitro, and may mark the death of non-neuronal cells. In Figure 5.7K, solid lines mark the growth of putative neuronal cells, whereas the dashed lines are representative of dying and detaching cells.

Mass growth profiles of primary neurons in culture have received little attention; our preliminary data shows an increase in mass growth followed by a plateau, which could be reminiscent of the internal commitment to axonal specification of neurons. The establishment of neuronal polarity (i.e. the extension and differentiation of neurites into axons and dendrites) is very well defined [30]. Dissociated neurons in vitro begin to send out immature neurites (typically 3-5 neurites), which remain approximately equal in length until one of the processes becomes committed to form an axon. After axonal specification, the axon exhibits robust growth to become the longest process and while the remaining processes commit to a dendritic fate and exhibit a slower growth rate. Our mass sensor provides an aggregate measurement of neuronal growth, or non-neuronal death, and is not capable of measuring

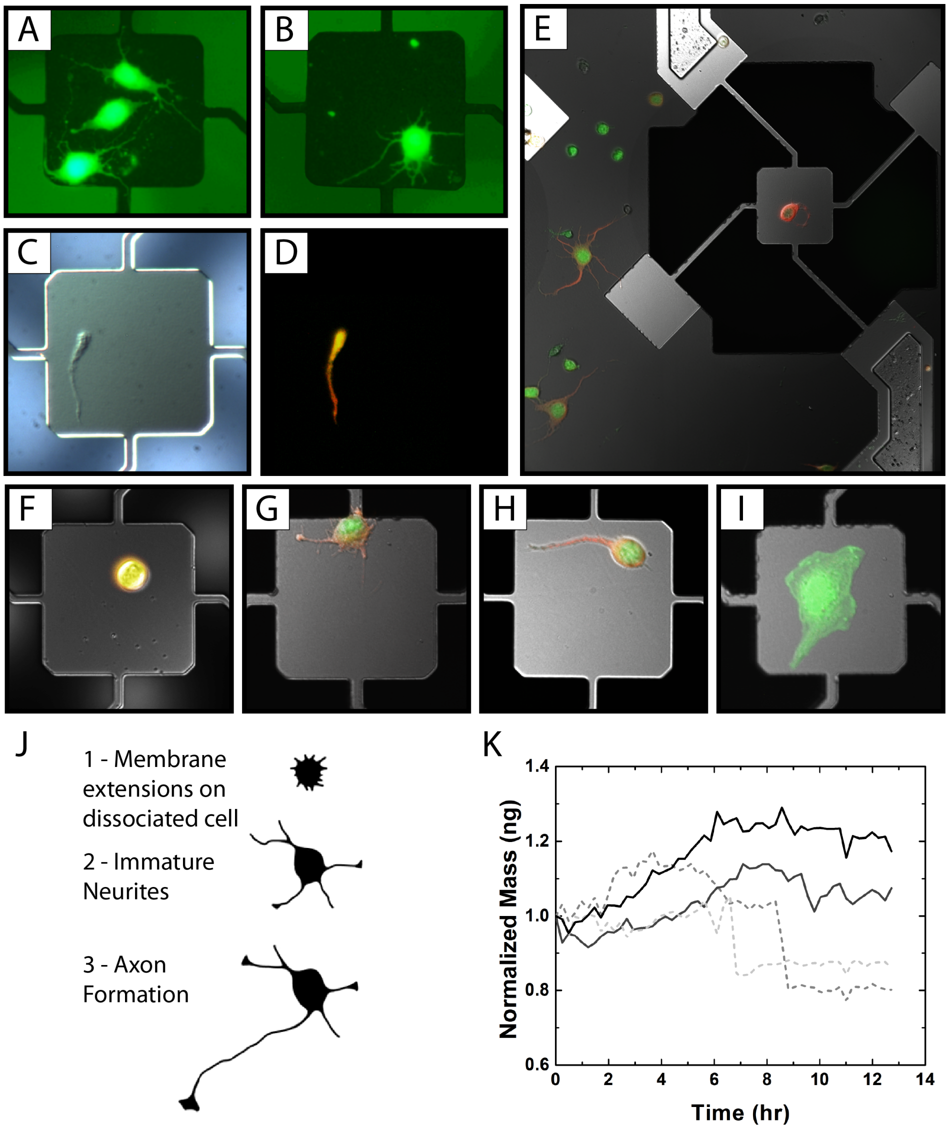

Figure 5.7: Mass and growth of neurons and glial cells measured by MEMS resonant mass sensors. The heterogeneous population of seeded cells leads to the capture of neuronal clusters or individual neurons captured on sensors (A-B) or even subcellular fragments, such as dendrites identified by size and high MAP2 expression (C-D). The captured neurons vary in development and differentiation states ranging from undifferentiated to polarized morphologies (E-H), and are easily distinguished from suspected glial cells (I). (J) Pictographic summary characteristic of early neuronal growth and differentiation, redrawn and modeled after previous descriptions [30]. Immature neurons differentiate by extending primary neurites, which then differentiate into an axon (longest process) and dendrites. (K) Mass of four individual cells measured with vertical flow resonant sensors. Neuronal growth and cell selection is prevalent in low-density primary neuronal cultures [17], whereas most non-neuronal cells die from the selectivity of defined media formulations. Putative neuronal growth (solid lines) and cell selection and death (dashed lines) are observable from measured growth profiles.

the growth of each process. Reconciling neuronal mass growth and differentiation will be a subject of instrumentation upgrades and future studies.

5.4 Conclusion

To overcome the challenges associated with investigating neuronal cell populations with MEMS mass sensors, we designed and fabricated a platform resonant sensor array with backside pore and integrated microfluidics. The on-chip microfluidic system allows for the constant supply of cellular growth media and also provides the means to increase removal of objects captured on sensor springs to improve capture efficiency and measurement yield. Characterization of device capture efficiency demonstrated a twofold increase over the previous generation sensor that did not allow for fluid flow. We measured the mass of dissociated cells harvested from the mouse hippocampus with the resonant sensor with vertical flow field. The measured mass, ranging from 0.1-0.9 ng, shows strong agreement with independent measurements of cell volume from confocal microscopy and reveals cells density to be approximately 1.15 g/mL. Growth profiles of immature neurons correspond with the characteristic developmental process of neuronal development, while growth profiles of non-neuronal cells reveal death in defined media as early as seven hours in vitro. Further studies of neuronal growth dynamics with this MEMS resonant sensor array may allow for the study of neuronal differentiation and selection with high measurement yield.

5.5 References

[1] S. Lindström and H. Andersson-Svahn. Overview of single-cell analyses: microdevices and applications. *Lab On A Chip*, 10(24):3363–3372, 2010.

[2] K. Park, J. Jang, D. Irimia, J. Sturgis, J. Lee, J. P. Robinson, M. Toner, and R. Bashir. ‘Living cantilever arrays’ for characterization of mass of single live cells in fluids. *Lab On A Chip*, 8(7):1034–1041, 2008.

[3] Y. Weng, F. F. Delgado, S. Son, T. P. Burg, S. C. Wasserman, and S. R. Manalis. Mass

sensors with mechanical traps for weighing single cells in different fluids. *Lab On A Chip*, pages 1–7, 2011.

[4] A. K. Bryan, A. Goranov, A. Amon, and S. R. Manalis. Measurement of mass, density, and volume during the cell cycle of yeast. *Proceedings of the National Academy of Sciences USA*, 107(3):999–1004, January 2010.

[5] W. H. Grover, A. K. Bryan, M. Diez-Silva, S. Suresh, J. M. Higgins, and S. R. Manalis. Measuring single-cell density. *Proceedings of the National Academy of Sciences USA*, 108(27):10992–10996, 2011.

[6] K. Park, L. J. Millet, N. Kim, H. Li, X. Jin, G. Popescu, N. R. Aluru, K. Hsia, and R. Bashir. Measurement of adherent cell mass and growth. *Proceedings of the National Academy of Sciences USA*, 107(48):20691–20696, 2010.

[7] K. Park, N. Kim, D. T. Morisette, N. R. Aluru, and R. Bashir. Resonant MEMS Mass Sensors for Measurement of Microdroplet Evaporation. *Journal of Microelectromechanical Systems*, 21(3):702–711, 2012.

[8] M. Godin, F. F. Delgado, S. Son, W. H. Grover, A. K. Bryan, A. Tzur, P. Jorgensen, K. Payer, A. D. Grossman, M. W. Kirschner, et al. Using buoyant mass to measure the growth of single cells. *Nature Methods*, 7(5):387–390, 2010.

[9] L. J. Millet, E. A. Corbin, R. Free, K. Park, H. Kong, W. P. King, and R. Bashir. Characterization of Mass and Swelling of Hydrogel Microstructures using MEMS Resonant Mass Sensor Arrays. *Small*, 8(16):2555–2562, 2012.

[10] E. A. Corbin, L. J. Millet, J. H. Pikul, C. L. Johnson, J. G. Georgiadis, W. P. King, and R. Bashir. Micromechanical properties of hydrogels measured with mems resonant sensors. *Biomedical Microdevices*, pages 1–9, 2013.

[11] N. N. Watkins, S. Sridhar, X. Cheng, G. D. Chen, M. Toner, W. Rodriguez, and R. Bashir. A microfabricated electrical differential counter for the selective enumeration of CD4+ T lymphocytes. *Lab On A Chip*, 11(8):1437, 2011.

[12] L. J. Millet and M. U. Gillette. over a century of neuron culture: From the hanging drop to microfluidic devices. *The Yale Journal of Biology and Medicine*, 85(4):501, 2012.

[13] L. J. Millet and M. U. Gillette. New perspectives on neuronal development via microfluidic environments. *Trends in Neurosciences*, 2012.

[14] K. Park and R. Bashir. Mems-based resonant sensor with uniform mass sensitivity. In *Solid-State Sensors, Actuators and Microsystems Conference, 2009. TRANSDUCERS 2009. International*, pages 1956–1958. IEEE, 2009.

[15] L. J. Millet, M. B. Collens, G. L. W. Perry, and R. Bashir. Pattern analysis and spatial distribution of neurons in culture. *Integrative Biology*, 3(12):1167–1178, 2011.

[16] L. J. Millet, M. E. Stewart, J. V. Sweedler, R. G. Nuzzo, and M. U. Gillette. Microfluidic devices for culturing primary mammalian neurons at low densities. *Lab On A Chip*, 7(8):987–994, 2007.

[17] G. J. Brewer, J. R. Torricelli, EK Evege, and P. J. Price. Optimized survival of hippocampal neurons in b27-supplemented neurobasal, a new serum-free medium combination. *Journal of Neuroscience Research*, 35(5):567–576, 1993.

[18] K. Park, J. Shim, V. Solovyeva, E. Corbin, S. Banerjee, and R. Bashir. Hydrodynamic loading and viscous damping of patterned perforations on microfabricated resonant structures. *Applied Physics Letters*, 100(15):154107–154107, 2012.

[19] S. Kaech and G. Banker. Culturing hippocampal neurons. *Nature Protocols*, 1(5):2406–2415, 2007.

[20] T. L. Fletcher and G. A. Banker. The establishment of polarity by hippocampal neurons: The relationship between the stage of a cell's development¡ i¿ in situ¡/i¿ and its subsequent development in culture. *Developmental Biology*, 136(2):446–454, 1989.

[21] J. C. Chang, G. J. Brewer, and B. C. Wheeler. Neuronal network structuring induces greater neuronal activity through enhanced astroglial development. *Journal of Neural Engineering*, 3(3):217, 2006.

[22] A. D. Bangham and B. A. Pethica. The adhesiveness of cells and the nature of the chemical groups at their surfaces. In *Proc. Roy. Phys. Soc. Edinburgh*, volume 28, pages 43–50, 1960.

[23] A. S. G. Curtis. Timing mechanisms in the specific adhesion of cells. *Experimental Cell Research*, 8:107–122, 1961.

[24] A. Pierres, A. M. Benoliel, D. Touchard, and P. Bongrand. How cells tiptoe on adhesive surfaces before sticking. *Biophysical Journal*, 94(10):4114–4122, 2008.

[25] K. D. McCarthy and L. M. Partlow. Preparation of pure neuronal and non-neuronal cultures from embryonic chick sympathetic ganglia: a new method based on both differential cell adhesiveness and the formation of homotypic neuronal aggregates. *Brain Research*, 114(3):391–414, 1976.

[26] M. J. Humphries. Cell adhesion assays. In *Extracellular Matrix Protocols*, pages 203–210. Springer, 2009.

[27] J. L. Hutter, J. Chen, W. K. Wan, S. Uniyal, and M. Leabu. Atomic force microscopy investigation of the dependence of cellular elastic moduli on glutaraldehyde fixation. *Journal of Microscopy*, 219(2):61–68, 2005.

[28] F. Braet, C. Rotsch, E. Wisse, and M. Radmacher. Comparison of fixed and living liver endothelial cells by atomic force microscopy. *Applied Physics A: Materials Science & Processing*, 66:S575–S578, 1998.

[29] Y. Lu, K. Franze, G. Seifert, C. Steinhäuser, F. Kirchhoff, H. Wolburg, J. Guck, P. Janmey, E. Wei, J. Käs, et al. Viscoelastic properties of individual glial cells and neurons in the cns. *Proceedings of the National Academy of Sciences USA*, 103(47):17759–17764, 2006.

[30] C. G. Dotti, C. A. Sullivan, and G. A. Banker. The establishment of polarity by hippocampal neurons in culture. *The Journal of Neuroscience*, 8(4):1454–1468, 1988.

Chapter 6

Micro-patterning of Mammalian Cells on MEMS Mass Sensors for Long-Term Growth Measurements

MEMS resonant mass sensors can measure the mass of individual cells, though long-term growth measurements are limited by the movement of cells off the sensor area. Micro-patterning techniques are a powerful approach to control the placement of individual cells in an arrayed format. In this work we present a method for micro-patterning cells on fully suspended resonant sensors through select functionalization and passivation of the chip surface. This method combines high-resolution photolithography with a blanket transfer technique for applying photoresist to avoid damaging the sensors. Cells are constrained to the patterned collagen area on the resonant sensor by pluronic acting as a cell adhesion blocker. This micro-patterning method enables long-term growth measurements, which is demonstrated by a measurement of the change in mass of a human breast cancer cell over 18 h.

6.1 Introduction

The use of microelectromechanical systems (MEMS) resonant sensors to study the growth of individual cells is a developing area of research [1–5]. Investigations of growth over the cell cycle require long-term measurements over many hours and are challenged by the movement of cells during the experiment. Cells that are highly motile, such as metastatic cancer cells, will move off the sensor thus ending the measurement. Even cells that are considered non-motile remain active, exhibiting spatial movements that permit cells to escape from the sensor [6]. Previous studies have used fluidic traps [3–5] and dielectrophoresis (DEP) [1] to control the positioning of cells on MEMS resonant sensors, though these methods require complicated on-chip systems and do not trap the cells for long periods of time. Methods for improving the retention of cells on MEMS resonant sensors for hours, or days, are needed to enable studies into the long-term growth dynamics of cancer cells.

Micro-patterned surfaces enable the capture and confinement of single cells or large populations [7–12]. Cell micro-patterning is an extremely powerful tool that promotes selective attachment and confinement of single cells through surface chemistry [13, 14]. Microcontact printing is one of the most popular laboratory techniques for the fabrication of chemical or protein micro-patterns [13]. The printing approach easily transfers protein patterns from a substrate acting as a stamp onto a surface; however, this technique is ideal for surfaces that can withstand the necessary stamping pressure and peeling force. Because MEMS resonant sensors have micron-scale features that are fragile they are incompatible with microcontact stamping process. A micro-patterning technique that can be integrated with suspended MEMS resonant devices offers an attractive solution for long-term measurement, while improving cell retention.

In this Chapter, we demonstrate a robust technique for selective surface micro-patterning on fully-suspended MEMS resonant mass sensors that overcomes the challenge of patterning on suspended devices by implementing a photoresist blanket transfer technique combined with high-resolution photolithography [15]. Patterning proteins against a background of cell adhesion blocker constrains cells to the viable sensor area of pedestal devices. This improves cell retention and enables growth measurements of even motile cells. We use the micro-patterned sensors to measure the change in mass of a human breast adenocarcinoma cell over eighteen hours, demonstrating the ability to study the long-term growth dynamics of cancer cells.

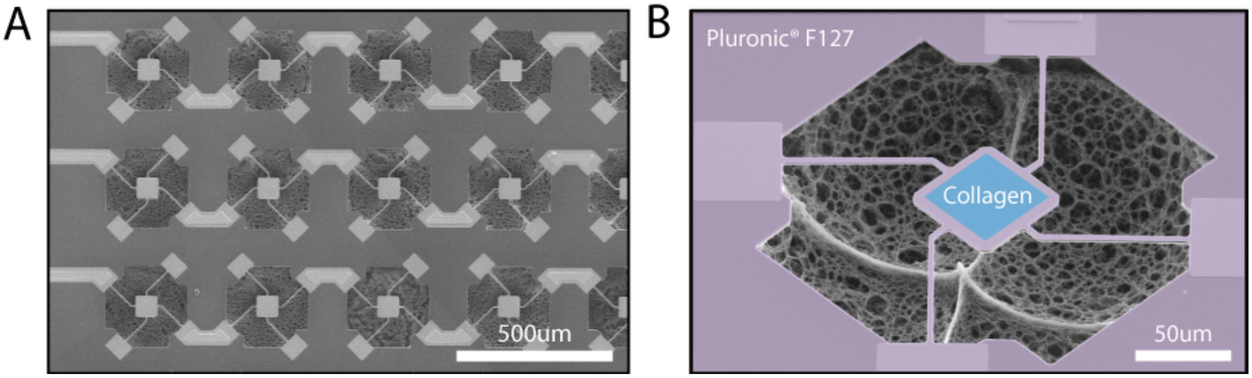

Figure 6.1: (A) Scanning electron micrograph (SEM) of a MEMS mass resonant sensor array. The chip design consists of 81 sensors fabricated in a 9 × 9 array. (B) SEM of a single sensor with an overlaid schematic of the selective functionalization and passivation technique where the center of the mass sensor is coated with collagen type I and the rest of the sensor area is backfilled with pluronic as a protein and cell blocker.

6.2 Materials and Methods

The MEMS resonant sensors used in this work consist of 60×60 μm^2 pedestals suspended by four beam springs over a shallow pit [2]. The sensor array consists of 81 individual sensors arrayed in a 9 × 9 format and is fabricated from a silicon-on-insulator wafer with the final step depositing a silicon oxide insulation layer. Figure 6.1A shows the device architecture, and full details of sensor fabrication are provided in previous works [2, 16]. The remainder of this section describes the procedure for micro-patterning of collagen onto the pedestal sensors following the schematic presented in Figure 6.1B.

6.2.1 Hydrophobic Surface Modification

The chip surfaces were treated by oxygen plasma exposure for 5 mins at 200 W. The chips were then placed in small groups in 100 mL glass jars. Hexamethyldisilizane (HMDS) was pipetted into each jar and the jars were sealed and heated at 80 °C for 1 h [17]. After vapor deposition of HMDS on the surface, the samples were gently rinsed with acetone, isopropanol, and DI water and allowed to dry. Figure 6.2A depicts the vaporization and self-assembly of the silane that caused pendant methyl groups to form a hydrophobic surface. We verified surface modification by observing water droplets easily rolling off.

6.2.2 Blanket Transfer and Lithography

Figure 6.2B depicts the process of transferring photoresist to the chip as a blanket for lithography [15]. Photoresist AZ 9260 (AZ Electronic Materials) was spin-coated onto a flat polydimethylsiloxane (PDMS) stamp and baked for 2 min at 50 °C. Next, the resist is brought into conformal contact with the chip and baked at 50 °C for another 2 min. The chip was then rapidly cooled to 4 °C and the PDMS was quickly peeled off the chip leaving the photoresist behind as a membrane over the sensors and the pit below [15]. After baking the photoresist-coated chip at 50 °C for 2 h to avoid bubble formation, the photoresist was patterned in a Karl Suss i-line mask aligner (SUSS MicroTec Group) with 10 mW/cm^2 intensity to open the area above each pedestal sensor (Figure 6.2C).

6.2.3 Collagen Functionalization and Pluronic Passivation

Following patterning, the chip was exposed to oxygen plasma at 300 W for 10 min to remove HMDS from the regions unprotected by photoresist. We then placed a PDMS chamber over the sensor area for functionalizing with a type I collagen solution in PBS (100 µg/mL) for 1 h at 37 °C. Following collagen deposition, the chip was rinsed with PBS and dried with a stream of nitrogen. This resulted in collagen deposition over both the patterned hole and the remaining photoresist surface. After removing the PDMS chamber, the chip was soaked in acetone upside down to lift-off the remaining photoresist from the surface. The lift-off procedure leaves geometrically defined collagen patterns selectively deposited on the sensor pedestals, while retaining a background of HMDS on the remaining surfaces.

After rinsing with DI water and drying with nitrogen, the chip was attached to a printed circuit board and wire-bonded at room temperature. Finally, Pluronic® F127 (Sigma

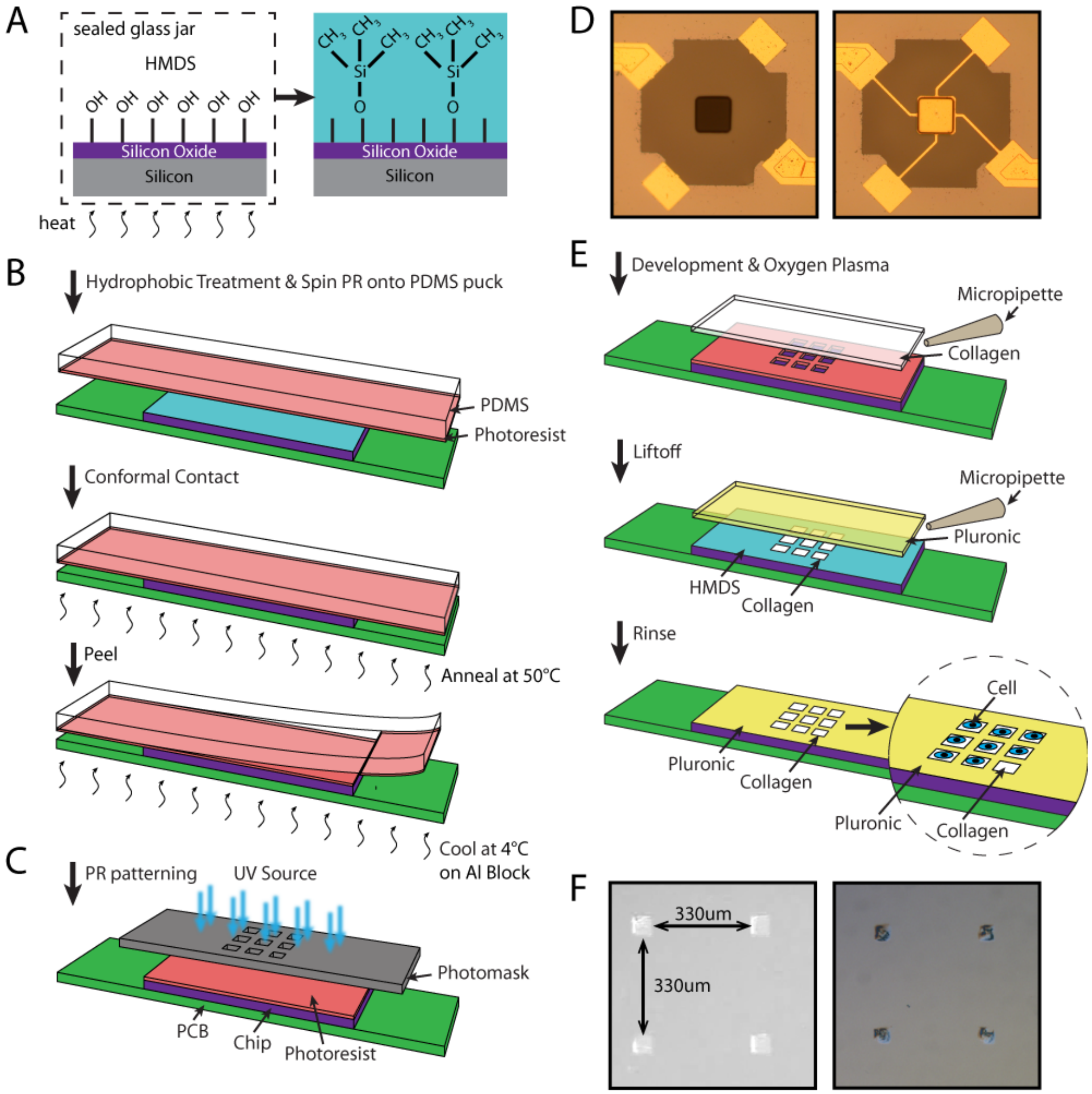

Figure 6.2: Overview of micro-patterning process for selective functionalization and passivation on MEMS resonant pedestal sensors. (A) First, the surface is treated with HMDS to promote hydrophobicity for easy attachment of the pluronic at the end of the entire process. (B) Photoresist is spun on a PDMS puck that is larger than the chip and baked, then stamped onto the chip and annealed. Finally, the chip and PDMS are rapidly cooled and the PDMS is peeled off, leaving the PR on the surface in a blanket coat. (C) The PR can then be patterned using a typical UV mask aligner and developed. (D) The square patterns on a broken sensor (left) and functional sensor (right), clearly showing the blanketing of the photoresist and the opening after development. (E) The developed pattern is treated in an oxygen plasma system to remove the HMDS selectively on the surface. After collagen functionalization, the photoresist is removed along with the excess collagen above in a liftoff process. Finally, pluronic is backfilled onto the exposed HMDS to act as a cell adhesion blocker. (F) DIC images of micro-patterned collagen on a plain silicon surface (left) and with cells attached (right).

Aldrich) was deposited by backfilling the chip with a 1% solution in PBS at room temperature for 2 h. Figure 6.2E presents the entire functionalization and passivation procedure.

6.2.4 Cell Culture and Preparation

Human breast adenocarcinoma cells (MCF-7 ATCC # HTB-22) were cultured in Dubecco's Modified Eagle Medium (Gibco) with 10% fetal bovine serum and 1% penicillin-streptomycin. Human breast cells (MCF-10A ATCC # CRL-10317) were cultured in Dulbecco's Modified Eagle Medium/Ham's F-12 (Gibco) with 5% horse serum, 20 ng/mL EGF, 0.5 mg/mL hydrocortisone, 100 ng/mL cholera toxin, 10 µg/mL insulin, and 1% penicillin streptomycin. Cells were treated with 0.05% trypsinEDTA (Gibco) for seeding on the sensor through a 100 µL well at a density of 9,000 cells per 100 µL.

6.3 Results and Discussion

Figure 6.1 shows an overview of the MEMS resonant sensors and the selective functionalization and passivation process. As a result, this process produces micro-patterned proteins on pedestal surfaces and deposits a protein and cell blocker on all other surfaces. The procedure for fabrication of these micro-patterns is summarized in Figure 6.2 and includes surface modification through vapor deposition of a self-assembled HMDS monolayer; blanket transfer of photoresist and high-resolution photolithography to define the pattern for collagen; and collagen deposition and backfilling of pluronic. To our knowledge, this is the first report of a method for micro-patterning cells on fully-suspended MEMS resonant sensors.

The challenge in patterning collagen on the surface of MEMS resonant sensors with lithography is the need for a method to consistently, and uniformly, deposit photoresist on the suspended devices. The devices are fully suspended by four beam springs, thus making them too fragile for spinning photoresist across the surface. To yield a more uniform and consistent photoresist deposition, we employed a transfer technique where photoresist is applied as a membrane, or blanket, covering both the sensors and pits beneath the sensors. Blanket lithography uses a PDMS substrate to spin a flat piece of photoresist for transfer to the chip. After soft baking the photoresist in contact with the chip, the chip is rapidly cooled. This heating-cooling process changes the fracture energy of the photoresist layer and allows for the PDMS substrate to be easily removed, leaving a uniform blanket of photoresist on the chip [15].

Once the photoresist is blanketed on the surface, standard photoresist patterning techniques maybe used (Fig. 6.2C), with the note that soft or separation contact would be ideal for delicate samples like this. In this case, we exposed 50×50 µm^2 square holes centered on each pedestal according to the pattern represented in Figure 6.1B. Figure 6.2D clearly shows the blanketing of the PR and the developed patterns over a pit with a removed sensor (left) and an intact sensor (right). In general, the size and shape of this pattern can be adjusted depending on sensor type and application. Oxygen plasma removes HMDS from the surface at the patterned openings in the photoresist to allow for functionalization with collagen. Figure 6.2F shows results of the patterning and blocking process, the square collagen deposits retain adherent cells that conform to the printed pattern.

Pluronic is a tri-block copolymer consisting of two polyethylene oxide (PEO) groups and a polypropylene oxide (PPO), and has been shown to be an effective blocking agent to deter protein adsorption [18] and cell adhesion [19–21]. The longevity of the pluronic non-adhesive coating has been characterized and cell are retained in clean patterns for approximately 3 days [20]. Pluronic can be applied to a surface in two ways: pancake or brush-like. The brush-like configuration is ideal for effectively blocking protein and cell adhesion. To achieve this conformation, devices are silanized with HMDS in order to achieve a highly hydrophobic surface with contact angles of about 80°. The PPO portion of the copolymer anchors to the surface and the PEO portions are dangling in a brush-like formation [22].

Figure 6.3A presents examples of captured MCF-10A cells on the platform sensor within the patterned area and not on the springs or around the sensor. Our MEMS sensors have

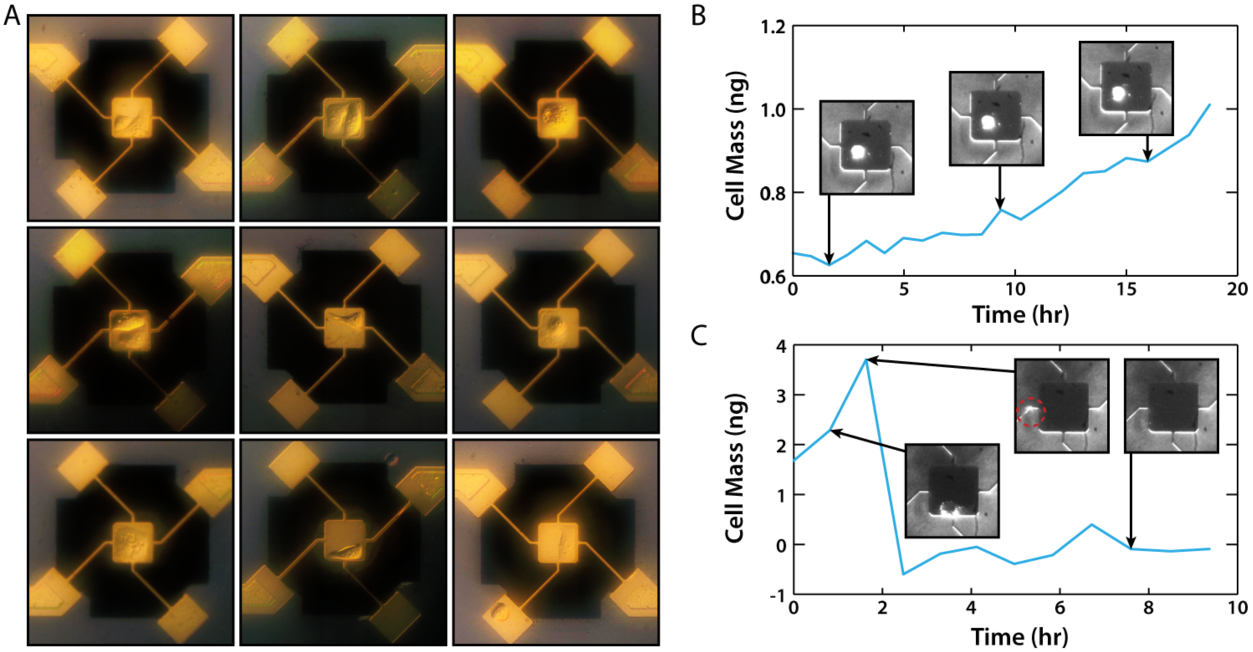

Figure 6.3: (A) DIC images of MCF-10A cells attached to the sensor area after collagen patterning and pluronic backfilling, with all adhered cells being within the patterned area. (B) Cell growth of an MCF-7 human breast cancer cell over 18 h, demonstrating the ability to capture and retain cells on the sensor surface for long-term growth measurements.

been previously used for applications of mass sensing [16, 23], including cell growth measurements [2]. Mass measurements with these resonant sensors use a previously published method that utilizes the change in resonant frequency shift of the sensor after a mass is added [2, 23]. Cellular growth measurements require the monitoring of changes in sensor resonant frequency over time. Integrating this micro-patterning technique further enables long-term growth measurements of dynamic and migratory cells. Figure 6.3B shows the measured mass of an MCF-7 cell over the course of 18 h. This cell is confined to the pedestal surface as a result of the selective functionalization and passivation process, thus allowing for a long-term growth measurement. This is in contrast to a measurement on an MCF-7 cell using a sensor without patterning seen in Figure 6.3C. The cell remained on the sensor platform for only two measurement covering less than an hour before migrating onto the spring thus invalidating the measurement and finally disappearing entirely from the sensor.

6.4 Conclusion

Here we present a novel method for micro-patterning of single cells directly on MEMS resonant platform sensors to enable long-term growth measurements of motile cells. We describe the use of a blanket photoresist transfer technique with standard photolithographic practices to achieve the basic patterning of proteins on the surface of the sensor. This selective functionalization, along with passivation of the remaining chip surface with pluronic, an effective cell and protein adhesion blocker, traps captured cells to the pedestal sensor area. The ability for long-term growth measurements with MEMS resonant sensors and micro-patterned surfaces is demonstrated by mass measurement of a human breast cancer cell over an eighteen-hour period. Future studies can use this technique to investigate metastatic cancer cells and other highly motile cell lines.

6.5 References

[1] K. Park, J. Jang, D. Irimia, J. Sturgis, J. Lee, J. P. Robinson, M. Toner, and R. Bashir. 'Living cantilever arrays' for characterization of mass of single live cells in fluids. *Lab On A Chip*, 8(7):1034–1041, 2008.

[2] K. Park, L. J. Millet, N. Kim, H. Li, X. Jin, G. Popescu, N. R. Aluru, K. J. Hsia, and R. Bashir. Measurement of adherent cell mass and growth. *Proceedings of the National Academy of Sciences USA*, 107(48):20691–20696, 2010.

[3] W. H. Grover, A. K. Bryan, M. Diez-Silva, S. Suresh, J. M. Higgins, and S. R. Manalis. Measuring single-cell density. *Proceedings of the National Academy of Sciences USA*, 108(27):10992–10996, 2011.

[4] T. P. Burg, M. Godin, S. M. Knudsen, W. Shen, G. Carlson, J. S. Foster, K. Babcock, and S. R. Manalis. Weighing of biomolecules, single cells and single nanoparticles in fluid. *Nature*, 446(7139):1066–1069, 2007.

[5] A. K. Bryan, A. Goranov, A. Amon, and S. R. Manalis. Measurement of mass, density, and volume during the cell cycle of yeast. *Proceedings of the National Academy of Sciences USA*, 107(3):999–1004, 2010.

[6] T. T. Rajah, S. M. Abbas Abidi, D. J. Rambo, J. J. Dmytryk, and J. T. Pento. The motile behavior of human breast cancer cells characterized by time-lapse videomicroscopy. *In Vitro Cellular & Developmental Biology-Animal*, 34(8):626–628, 1998.

[7] L. J. Millet, M. E. Stewart, R. G. Nuzzo, and M. U. Gillette. Guiding neuron development with planar surface gradients of substrate cues deposited using microfluidic devices. *Lab On A Chip*, 10(12):1525–1535, 2010.

[8] L. J. Millet, M. B. Collens, G. L. W. Perry, and R. Bashir. Pattern analysis and spatial distribution of neurons in culture. *Integrative Biology*, 3(12):1167–1178, 2011.

[9] C. S. Chen. Geometric Control of Cell Life and Death. *Science*, 276(5317):1425–1428, 1997.

[10] M. Théry, A. Pépin, E. Dressaire, Y. Chen, and M. Bornens. Cell distribution of stress fibres in response to the geometry of the adhesive environment. *Cell Motility and the Cytoskeleton*, 63(6):341–355, 2006.

[11] M. Théry, V. Racine, A. Pépin, M. Piel, Y. Chen, J. Sibarita, and M. Bornens. The extracellular matrix guides the orientation of the cell division axis. *Nature*, 7(10):947–953, 2005.

[12] M. Théry, V. Racine, M. Piel, A. Pépin, A. Dimitrov, Y. Chen, J. Sibarita, and M. Bornens. Anisotropy of cell adhesive microenvironment governs cell internal organization and orientation of polarity. *Proceedings of the National Academy of Sciences USA*, 103(52):19771–19776, 2006.

[13] J. Fink, M. Th Ry, A. Azioune, R. Dupont, F. O. Chatelain, M. Bornens, and M. Piel. Comparative study and improvement of current cell micro-patterning techniques. *Lab On A Chip*, 7(6):672, 2007.

[14] G. Csucs, T. Künzler, K. Feldman, F. Robin, and N. D. Spencer. Microcontact printing of macromolecules with submicrometer resolution by means of polyolefin stamps. *Langmuir*, 19(15):6104–6109, 2003.

[15] J. Yeom and M. A. Shannon. Detachment Lithography of Photosensitive Polymers: A Route to Fabricating Three-Dimensional Structures. *Advanced Functional Materials*, 20(2):289–295, 2010.

[16] L. J. Millet, E. A. Corbin, R. Free, K. Park, H. Kong, W. P. King, and R. Bashir. Characterization of Mass and Swelling of Hydrogel Microstructures using MEMS Resonant Mass Sensor Arrays. *Small*, 8(16):2555–2562, 2012.

[17] B. Dorvel, B. Reddy, I. Block, P. Mathias, S. E. Clare, B. Cunningham, D. E. Bergstrom, and R. Bashir. Vapor-Phase Deposition of Monofunctional Alkoxysilanes for Sub-Nanometer-Level Biointerfacing on Silicon Oxide Surfaces. *Advanced Functional Materials*, 20(1):87–95, 2010.

[18] M. Amiji and K. Park. Prevention of protein adsorption and platelet adhesion on surfaces by PEO/PPO/PEO triblock copolymers. *Biomaterials*, 13(10):682–692, 1992.

[19] P. Bajaj, B. Reddy, L. Millet, C. Wei, P. Zorlutuna, G. Bao, and R. Bashir. Patterning the differentiation of C2C12 skeletal myoblasts. *Integrative Biology*, 3(9):897–909, 2011.

[20] C. M. Nelson, S. Raghavan, J. L. Tan, and C. S. Chen. Degradation of Micropatterned Surfaces by Cell-Dependent and -Independent Processes . *Langmuir*, 19(5):1493–1499, 2003.

[21] V. A. Liu, W. E. Jastromb, and S. N. Bhatia. Engineering protein and cell adhesivity using PEO-terminated triblock polymers. *Journal of Biomedical Materials Research*, 60(1):126–134, 2002.

[22] M. R. Nejadnik, A. L. J. Olsson, P. K. Sharma, H. C. van der Mei, W. Norde, and H. J. Busscher. Adsorption of Pluronic F-127 on Surfaces with Different Hydrophobicities Probed by Quartz Crystal Microbalance with Dissipation. *Langmuir*, 25(11):6245–6249, 2009.

[23] E. A. Corbin, L. J. Millet, J. H. Pikul, C. L. Johnson, J. G. Georgiadis, W. P. King, and R. Bashir. Micromechanical properties of hydrogels measured with mems resonant sensors. *Biomedical Microdevices*, pages 1–9, 2013.

Chapter 7

Measuring Physical Properties of Normal and Cancerous Human Breast Cells: Initial Results

Investigating the growth signatures of single cells will determine how cell growth is regulated and size is maintained. Here we measure the mass, growth rate, and stiffness of individual benign (MCF-10A), low metastatic (MCF-7), and high metastatic (MDA-MB-231) breast cancer cells. Micro-patterning that was introduced in chapter 6 will allow for the long-term growth of motile cells. Preliminary results show growth rates of 4.8%, 1.6%, and 2.8% for MCF-10A, MCF-7, and MDA-MB-231. This demonstrates that normal cells have a higher growth rate than cancerous cells, while growth rates are higher with greater metastatic potential. The mass growth rates are comparable to database doubling times obtained through conventional bulk analysis techniques. As shown previously, this measurement technique is affected by viscoelastic properties of cells. The mechanical properties of cells are measured using indentation with atomic force microscopy and used to interpret measured mass values before and after fixation, which is known to increase stiffness. This reveals a difference in cell shape between cancer lines that may be related to decreased adhesion with high metastatic potential.

7.1 Introduction

Cancer arises from a number of mutations in the genetic makeup of a cell that is transferred to daughter cells and results in the proliferation of cancer [1–3]. Cancerous mutations alter relevant signaling pathways, which in-turn influence the interaction and response of a cell to mechanical stimuli and growth factors and how the cell cycle is regulated. It is widely known that cell cycle checkpoints are broken and unregulated in cancer cells, thus allowing the cell to grow and divide without the proper signaling cues [1–3]. The uncontrolled proliferation and division of cells is a mainstay of cancer; however, studies have not conclusively characterized the coordination of cell growth with the cell cycle. Additional considerations surround metastasis, which occurs when cells break away and move throughout the body, though the physical characteristics determining metastatic potential remain ambiguous.

Measuring cellular growth is very challenging, and there is a debate about the appropriateness of commonly used population-based methods that average the growth of many cells [4–7]. However, when considering time-dependent measurements of growth over the cell cycle, single cell techniques are necessary to coordinate growth with cycle phase and avoid misleading analysis [5, 7]. Single cell growth measurements are limited by many factors, most importantly the poor ability to handle and manipulate individual cells in real time. However, the recent development of microelectromechanical systems (MEMS) resonant mass sensors has provided new measurement and analysis tools for studying growth on the single cell level [8–11]. This work uses a pedestal resonant sensor designed for measuring the mass of adherent cells [8] coupled with the micro-patterning technique I described in Chapter 6.

The cell cycle disruptions in cancer also lead to changes in the physical characteristics of cells, such as stiffness, that affect the environmental behavior of cells including cell-to-cell and cell-to-substrate signaling [12]. These interactions can ultimately determine cellular growth, migration, and apoptosis, thus it is important to consider biophysical properties in the study of cancer and metastasis. For instance, cancer cells are known to be softer than normal cells [13, 14], which can allow for easier transport to other organ systems in metastasis [REF]. By combining growth and stiffness measurements, a more complete understanding of how environmental interactions impact the proliferation of cancer.

In this chapter, I use MEMS resonant mass sensors to compare the long-term growth of normal epithelial cells (MCF-10A) with cancer cells of both high (MDA-MB-231) and low metastatic potential (MCF-7). The growth rate of each cell line is calculated based on mass measurements over time to compare between cancerous and normal cells. Additionally, I measure the stiffness of cells from each line with atomic force microscopy (AFM) and analyze the role of stiffness on the mass measurements through the use of the two-degree-of-freedom model introduced previously. Finally, I begin to explore the changes and influences of cell shape and adhesion on the measurement through fixation experiments and confocal microscopy. Together, these measurements represent the first multimodal investigation into the physical properties of cancer cells and their role in metastasis.

7.2 Materials and Methods

7.2.1 Select Functionalization

In order to micro-pattern cells on the pedestal sensors, a selective functionalization and backfill passivation technique was used. This process is fully described in Chapter 6, but will be briefly summarized here. Prior to initiating cell patterning and subsequent mass measurements, a hydrophobic layer of hexamethyldisilizane (HMDS) was applied to the sensor surface through vapor deposition to promote efficient deposition of Pluronic® F127. [15] Due to the delicate nature of the structure, a photoresist transfer technique [16] was used to provide a uniform layer of photoresist to be patterned. The sample was then developed and exposed to oxygen plasma to remove HMDS from the openings in the photoresist for deposition of collagen type I. After rinsing the surface with PBS, the chip was soaked in acetone to lift-off the photoresist, leaving collagen selectively on the pedestals of the sensors and surrounded by HMDS everywhere else. At this point the chip was attached to a printed circuit board and wire-bonded at room temperature.

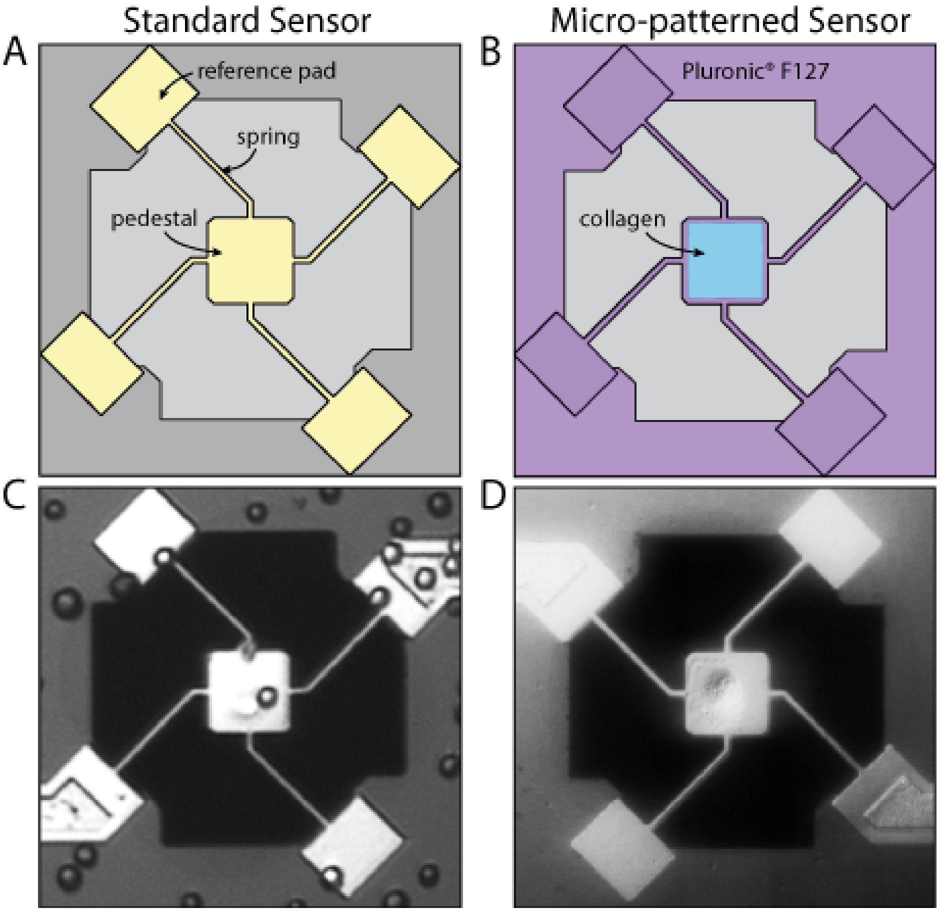

Figure 7.1: Overview of the select functionalization and passivation process. (A) Cartoon of the sensor layout. (B) Cartoon of the desired patterning with collagen or another ECM material selectively patterned in the center of the pedestal and with pluronic backfilled everywhere else. (C) Bright field image of a single released non-patterned pedestal sensor that has been seeded with human colon cancer cells (HT29). It is shown that cells are able to attach to the springs and anywhere else that could ultimate affect the cell measurement. (D) Bright Field image of a single released patterned pedestal sensor seeded with human breast cells (MCF-10A) and then rinsed to remove non-attached cells.

7.2.2 Cell Mass Measurement

The mass measurement compares the resonant frequency of a loaded sensor with its original, unloaded state to determine the mass of the loaded object. This is a well-characterized method described fully in Chapter 2 that will only be briefly introduced here. Calculating object mass requires the measurement of three resonant frequencies, which can be found using a system that combines electromagnetic actuation and a laser Doppler vibrometer (LDV). First, the empty sensor resonant frequency was measured in air to obtain the spring constant. Next, the micro-patterning procedure was completed by backfilling with pluronic to passivate the remaining chip surfaces. The second empty sensor frequency was then measured in liquid to determine the reference frequency, which is reduced from the in-air frequency due to hydrodynamic loading. At this point cells were seeded and allowed to attach for 1 h before being gently rinsed to remove non-adhered cells. Finally, the in-liquid resonant frequency of the mass loaded sensors were measured for comparison with the empty sensor frequency to calculate the attached mass. This measurement of the loaded sensor frequency was repeated over time to produce a growth profile.

7.2.3 Cell Culture and Fixation Protocol

Normal human breast epithelial cells (MCF-10A) were cultured in Dulbecco's Modified Eagle Medium/Ham's F-12 (Gibco) with 5% horse serum, 20 ng/mL EGF, 0.5 mg/mL hydrocortisone, 100 ng/mL cholera toxin, 10 µg/mL insulin, and 1% penicillin streptomycin. Human breast adenocarcinoma cells (MCF-7) were cultured in Dubecco's Modified Eagle Medium (Gibco) with 10% fetal bovine serum and 1% penicillin streptomycin. Highly metastatic human breast adenocarcinoma cells (MDA-MB-231) were cultured in Leibovitz's L-15 Medium (Sigma-Aldrich) with 10% fetal bovine serum and 1% penicillin streptomycin.

Cells were introduced onto the sensors at a total of 9,000 cells per chip and allowed to adhere. The sensors were rinsed with fresh growth media and the culture chamber was sealed with a sterilized glass cover slip for the measurement. Mass measurements were taken approximately every 20 min for up to 24 h. After the cell growth measurements, the cells were fixed with 4% paraformaldehyde for 30 min. The fixative solution was completely flushed and replaced with growth media, and the mass of each fixed cell was measured.

7.2.4 Mechanical Property Characterization

A NanoWizard®3 (JPK Instruments AG; Berlin, Germany) atomic force microscope (AFM) was used to characterize the mechanical properties of MCF-10A, MCF-7, and MDA-MB-231 cells. We used a silicon nitride cantilever with a spring constant of 0.006 N/m and a 4.5 μm silica spherical indenter to extract force-indentation curves. The cells were seeded on collagen type I treated glass coverslip that was attached to the base of a Petri dish with Norland optical adhesive. The adhesive was cured using a BioForce Nanosciences UV/Ozone cleaner for 10 mins, prior to collagen deposition and cell seeding.

Force-distance curves were taken at 64 points (8 × 8) over the entire cell structure. The elastic modulus of the each point on the cell was extracted from the region of elastic deformation using the Hertz model, as described for hydrogels in Chapter 4. In this case, the material properties of the spherical indenter particle, the elastic moduli and Poisson ratio, are 68 GPa and 0.19. The elastic modulus of each cell is reported as the median of all 64 measured points. Three cells from each cell line were measured both live and after fixation with 4% paraformaldehyde, as described above for the mass measurements.

The viscosity of each cell, both before and after fixation, was calculated from creep indentation measurements with AFM using the same cantilever and indenter tip. A step load was applied to the cantilever probe and the resulting applied force was held constant for ten seconds through a feedback loop on the cantilever deflection. While the force was held constant, the cantilever Z-sensor signal was was monitored to collect a creep curve, and extract the material viscosity using the Kelvin-Voigt model, as in Chapter 4. Once the low frequency viscosity is obtained from the creep measurements, we need to adjust the effective viscosity to account for both frequency dependence and the high frequency of oscillation in the experiment.

The Kelvin-Voigt model uses the material viscosity to describe the imaginary part of the complex elastic modulus, $E = E' + iE''$, along with the oscillation frequency, ω:

$$E = E' + i\omega\eta. \tag{7.1}$$

However, the imaginary elastic modulus is also frequency-dependent and generally obeys a power-law relationship:

$$E''(\omega) = E''_0\omega^{\alpha}. \tag{7.2}$$

Combining the two equations, and assuming an α of 0.2 [REF], we derive an expression for the effective viscosity at a frequency of 60 kHz, relative to the nominal viscosity, η_0:

$$\eta_{60kHz} = \frac{\eta_0}{2\pi(60kHz)^{\alpha}} \tag{7.3}$$

7.2.5 Confocal Measurements

I used confocal microscopy to determine volume, height, and shape ratio of a population of patterned single cells labeled with lipophilic fluorescent dye DiOC6(3) (3 µL/mL) and immersed in PBS. Confocal image stacks (Z-stacks) were acquired with a Zeiss 710 laser scanning confocal microscope using an Argon laser (488 nm) and a 40x water immersion objective (Carl Zeiss Microscopy GmbH; Jena, Germany). To ensure that the Z-stacks represented the cell dimensions accurately in three-dimensions, XYZ voxel size (X=0.69 µm, Y=0.69 µm, Z=0.48 µm) was set based on Nyquist criteria (two pixels per actual unit resolution in XYZ).

7.3 Results and Discussion

Direct, long-term growth profiles of breast epithelial cell lines are measured using MEMS resonant pedestal sensors with micro-patterned surfaces for selective functionalization and passivation described in Chapter 6 (Figure 7.1). The cell lines studied include MDA-MB-231 and MCF-7, which are cancerous with high and low metastatic potential, respectively, and a normal cell line, MCF-10A, for comparison. Repeated mass measurements of single cells captured on the mass sensor the mass reveal the increase of cellular mass due to growth over the cell cycle. Figure 7.2A-C gives examples of individual cell growth that continues until the cell division where a temporary decrease in mass is detected. During mitosis the dividing cell will partially detach from the platform, thus decreasing the contact area and altering the shape of the cell. [8] This affects the mass reading according to the two-degree-of-freedom model described in previous chapters, and will be investigated in more detail below.

The growth dynamics of these different single epithelial cells were analyzed using the individual temporal mass profiles, such as those shown in figure 7.2A-C, and the derivative of the mass in time gives the instantaneous mass change rate. For a given cell line there is a large number of time data points from all the measured cells, and figure 7.2D-F shows histograms of the instantaneous mass change rate data for each cell line after binning into four groups based on instantaneous mass. Taking derivatives of noisy cell mass data can lead to negative instantaneous mass change rates as shown in figure 7.2D-F. This noise can arise from a combination of short-term variations in cell stiffness, viscosity, density, or adhesion of the cell over the cell cycle. However, over long periods of time there is a clearly identifiable increase in cell mass, confirmed by simultaneous optical imaging.

Figure 7.2G translates the distributions found in figure 7.2D-F to find the cell mass growth rate indicated by the linear trends of the bin max peaks. These trends suggest that cells with greater mass also have an increased rate of mass accumulation, regardless of cell line. However, the cell lines do have different exponential growth rates, which is

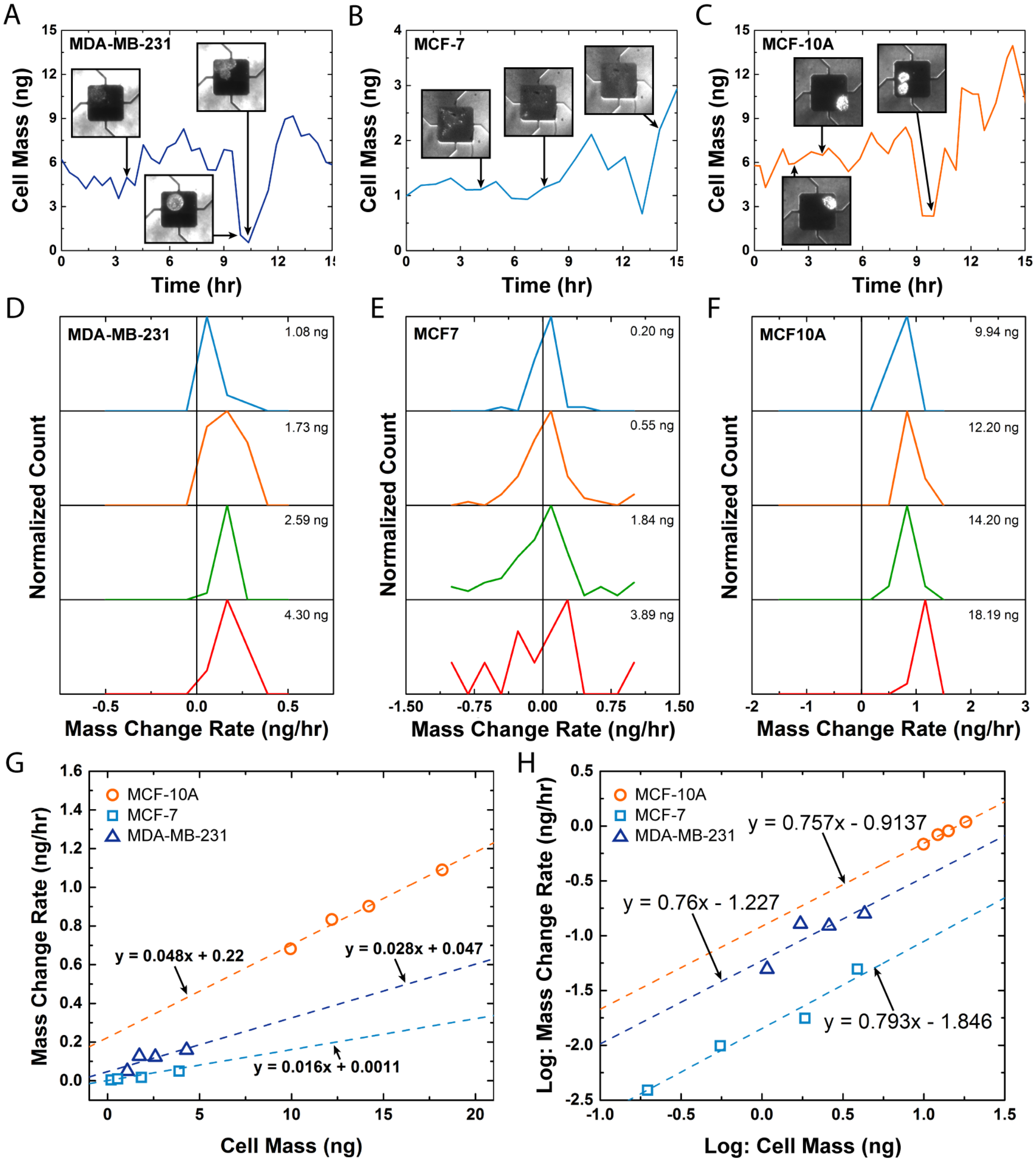

Figure 7.2: Mass measurement of adherent cells versus time for each cell line. Each growth profile shows an increase of a single adherent cell, then will go through a cell division that is marked by a sudden decrease in cell mass, once division has completed the growth profile continues. (A) MDA-MB-231. (B) MCF-7. (C) MCF-10A. Analysis of cell growth rate and mass change rate versus mass. Four histograms accounting for the mass accumulation at specific mass values. (D) MDA-MB-231. (E) MCF-7. (F) MCF10-A. (G-H) Analysis of mass change rate per unit mass of individual cells. A five point moving average of changes in mass from all culture data points of individual breast cells. (G) Average cells acquire 1.6%, 2.8%, 4.8% additional mass every hour for MCF-7, MDA-MB-231, and MCF-10A, respectively. (H) Log-log plot shows a power law of the different cell lines where the slopes are less than unity verifying consistency with scaling rules of energy consumption versus size of an organism.

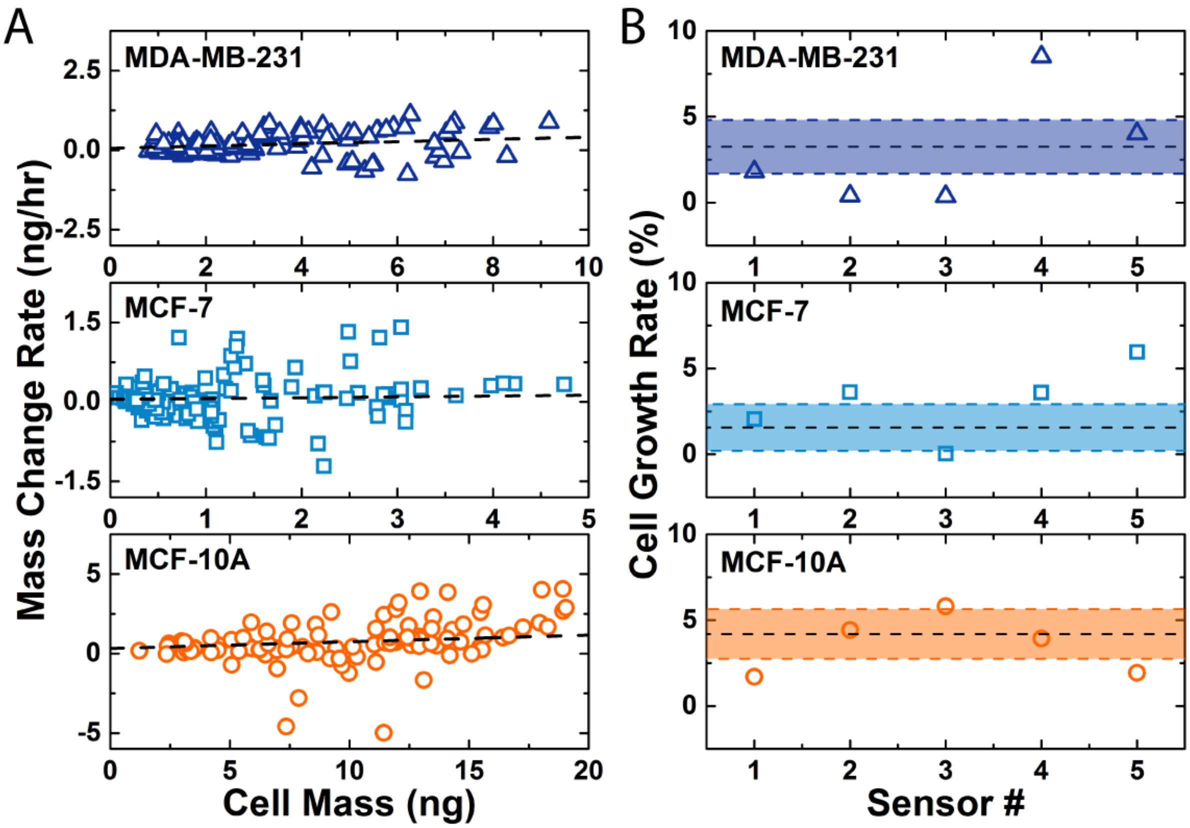

Figure 7.3: (A) Bulk growth rate measure approach. (B) Individual sensor/cell approach. We begin to see heterogeneity of the mass measurements. When looking at the bulk lots of the variation disappears, and we miss maybe some of the important time dependent changes.

the slope of the mass change rate against mass. Figure 7.2G shows that MCF-10A, MCF-7, and MDA-MB-231 on average accumulate 4.8%, 1.6%, and 2.8% of their mass every hour. The growth rates translate to mass doubling times of 14.8, 43.7, and 25.1 hours (=log(2)/log(1+rate)). Five growth curves for each of the cell lines were taken, however, more curves will be necessary in the future for a complete study. Finally, figure 7.2H presents a log-log plot comparing mass change rate with cell mass. The growth follows the rules of scaling energy consumption by having a slope less than unity. [17]

The American Type Culture Collection biological resource center (ATCC) provides doubling times based on the time for culture to double in size. For MCF-10A cells, this doubling time is 16 hours, while it is 38 hours for both MCF-7 and MDA-MB-231 cells. The value for mass doubling time of MCF-10A obtained with the mass sensor is close to that of the ATCC calculation. However, between the MCF-7 and the MDA-MB-231, which are the low and high metastatic cancer cell lines, there are deviations from the ATCC doubling times and the measured mass doubling times. The high metastatic cells appear to grow faster, while the low metastatic cells grow slower than the ATCC estimates. These mass growth rate values may converge toward the ATCC doubling times with more measurements, though they provide an interesting view of the heterogeneity of cell behavior within a homogeneous population. A major challenge has been the difference in cell size between cell lines, which has made this analysis far more difficult.

Proper analysis is imperative to understanding and interpreting the growth measurements. Figure 7.2 shows a growth rate analysis where all mass change rates are binned together based on instantaneous mass, though this analysis is more akin to studies on the bulk scale. Since we cannot determine the point of the cell cycle for proper comparison we are likely obscuring subtle events due to differences in cycle phase. Heterogeneity exists within a homogeneous population implying that cells are not created equal, and yielding differences between cells such as size or mass. Expression of subtle signature differences in growth among individual cells can help explain why one cell may grow differently or lead to metastasis. It is reassuring that we achieve results similar to ATCC, however, other options for measuring the growth of individual cells is necessary to ensure that we are capturing all elements of the cell cycle. Figure 7.3A shows a bulk approach for calculating growth rate without binning, which can cause bias due to distribution of cell masses. Comparatively, figure 7.3B shows the growth rates of individual cells overlaid on the average growth rate found in figure 7.3A. Individual cells show growth rates that fall outside the bounds of the bulk analysis, and without knowing the phase of the cycle bulk analysis and averaging will ruin the resolution of the measurement. Additionally, there is the need for the analysis to include individual cell shape and adhesion for further understanding of variations in the growth measurements.

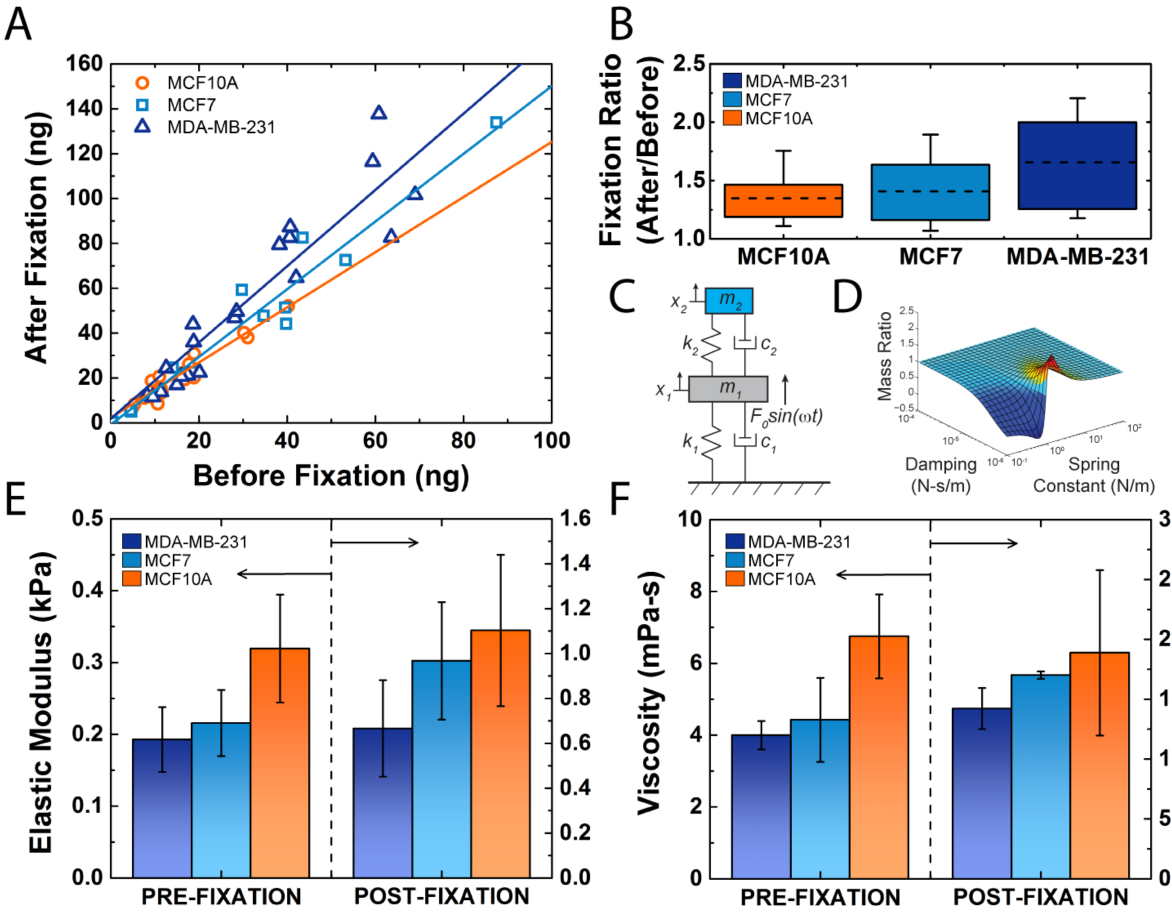

Figure 7.4: The apparent mass after to before ratio. (A) The apparent mass of MDA-MB-231, MCF-7, and MCF-10A cells after fixation are 1.7, 1.5, and 1.2, times greater than before fixation, respectively. (B) Variation of the fixation ratio versus mass for each cell line with the mean fixation ratio indicated as a solid black line. (C) Overview of the two-degree-of-freedom system model. (C) An example of a result from the 2DOF model. (E-F) AFM mechanical measurements both before and after fixation performed on MDA-MB-231, MCF-7, and MCF-10A. (E) Elastic Modulus values that were extracted through force measurements. (F) Viscosity values that were extracted through force measurements with a dwell period on the surface performing a creep measurement.

I investigated the role of individual cell shape on mass measurements by comparing the measured cell mass before and after fixation. Figure 7.4A shows the relation between fixed and live apparent mass for each measured cell, where there is a clear discrepancy between the two values. As explained previously, soft materials will vibrate out of phase with the pedestal,

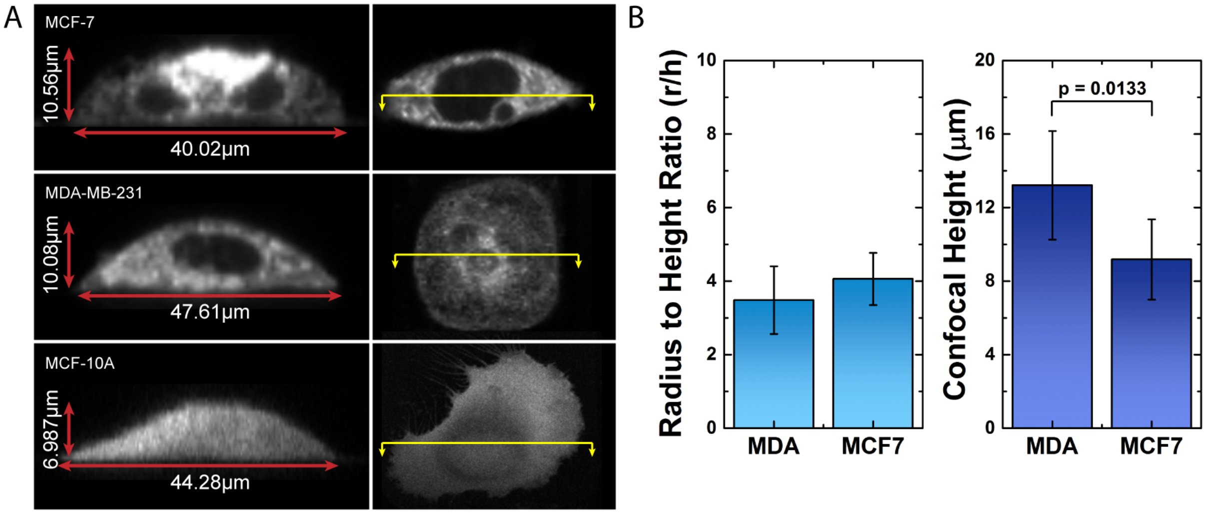

Figure 7.5: (A) Lateral and axial confocal images of MCF-7, MDA-MB-231, and MCF-10A showing the height and contact area diameter of each cell type. (B) Radius to height ratios for MCF-7 and MDA-MB-231 found through the forward 2DOF problem. The values are then verified through confocal, showing that there is not much variation in the contact area radius; however, there is a change in the heights.

thus causing a shift in resonant frequency and skewing the measurement. Figure 7.4A shows fitted trendlines for each cell line with the slope representing the ratio between fixed mass and live mass. MDA-MB-231 has the largest discrepancy between the two measurements with a slope of 1.7, followed by MCF-7 with a slope of 1.5 and MCF-10A with a slope of 1.2. This phenomenon can be explained through the two-degree-of-freedom system of a cell attached the vibrating platform (figure 7.4C). We model the cell as a Kelvin-Voigt material, which consists of a mass attached to a spring and damper in parallel, and is accepted as an appropriate model for cellular behavior. [18–21] Figure 7.4D shows the general shape of apparent mass ratio predicted by the model, where at low viscosity and low stiffness there will be a discrepancy between the mass measurements.

I used AFM to measure cellular mechanical properties, stiffness and viscosity, both before and after fixation. Figure 7.4E-F shows the results of these measurements, where the elastic modulus ranges from 200 Pa to 320 Pa before fixation to 700 Pa to 1100 Pa after fixation. I found that MDA-MB-231 was the softest of the cell lines followed by MCF-7 and then

MCF-10A. This trend remained the same both before and after fixation. Viscosity values exhibited the same trends as elastic modulus. Viscosity before fixation ranged between 4.5 mPa-s to 7 mPa-s, while viscosity after fixation ranged between 14 mPa-s to 19 mPa-s.

These mechanical property values are used to predict the apparent mass ratios of Figure 7.4A, however there are other considerations necessary in using the model. The model is not only affected by cell stiffness and viscosity, but the shape of the cell can also influence results. This can explain why the two cancerous cell lines, MCF-7 and MDA-MB-231, have very between apparent mass ratios from the fixation experiment though the mechanical properties are very similar. It is known that as cancer cells become more metastatic, there can be a loss of adhesion to the extracellular matrix [22] that can cause cells to have a taller profile. Figure 7.5A shows lateral and axial confocal images of cells from each cell line that have different ratios of cell height and base radius. The data from the fixation experiments combined with properties from AFM allow for the radius to height ratio to be predicted using the two-degree-of-freedom model. Figure 7.5B displays the differences in predicted radius to height ratio of the cancer cell lines. The MCF-7 cells remain flatter to the surface, whereas the MDA-MB-231 cells appear to have a taller profile or have a smaller footprint on the surface of the sensor. This result is verified through the use of confocal measurements.

7.4 Conclusion

The mechanisms underlying the growth of cancer cells over the cell cycle remains an important area of investigation, though our knowledge is limited due to the inability to measure the growth of individual cells reliably. This chapter presents the first use of MEMS resonant sensors to investigate the differences in growth between normal and cancer cells through long-term mass measurements. Reliable placement and retention of cells on the sensors through the use of micro-patterning for selective functionalization and passivation allowed for the study of both motile and non-motile adherent cells for at least fifteen hours. Cells from each investigated cell line show an increase in mass change rate with respect to mass; therefore, the heavier cells accumulate more mass more quickly. Preliminary results suggest that normal cells grow faster than cancer cells, and that cancer cell growth also increases with metastatic potential. While the measured growth rates show good agreement with independent doubling time estimates, there are growth variations between individual cells within the same population that must be considered in future studies. Additionally, the monitoring of cell cycle status through optical verification with fluorescence will allow for better correlation of the growth profiles of individual cells, and potentially the identification of growth rates during specific cycle phases.

7.5 References

[1] R. A. Weinberg. *The biology of cancer*, volume 255. Garland Science New York, 2007.

[2] B. Alberts, A. Johnson, J. Lewis, M. Raff, and K. Roberts. *Molecular biology of the cell, 5th edition.* National Center for Biotechnology InformationÕs Bookshelf, 2002.

[3] H. Lodish. *Molecular cell biology 5th edition.* Macmillan, 2008.

[4] J. M. Mitchison. Growth during the cell cycle. *International Review Of Cytology - A Survey Of Cell Biology, Vol 226*, 226:165–258, 2003.

[5] D. Di Carlo and L. P. Lee. Dynamic single-cell analysis for quantitative biology. *Analytical Chemistry*, 78(23):7918–7925, 2006.

[6] S. Cooper. Distinguishing between linear and exponential cell growth during the division cycle: Single-cell studies, cell-culture studies, and the object of cell-cycle research. *Theoretical Biology and Medical Modelling*, 3:10, 2006.

[7] D. Di Carlo, H. T. K. Tse, and D. R. Gossett. Introduction: why analyze single cells? *Methods in Molecular Biology*, 853:1–10, 2012.

[8] K. Park, L. J. Millet, N. Kim, H. Li, X. Jin, G. Popescu, N. R. Aluru, K. J. Hsia, and R. Bashir. Measurement of adherent cell mass and growth. *Proceedings of the National Academy of Sciences USA*, 107(48):20691–20696, 2010.

[9] Y. Weng, F. F. Delgado, S. Son, T. P. Burg, S. C. Wasserman, and S. R. Manalis. Mass sensors with mechanical traps for weighing single cells in different fluids. *Lab On A Chip*, pages 1–7, 2011.

[10] A. K. Bryan, A. Goranov, A. Amon, and S. R. Manalis. Measurement of mass, density, and volume during the cell cycle of yeast. *Proceedings of the National Academy of Sciences USA*, 107(3):999–1004, 2010.

[11] W. H. Grover, A. K. Bryan, M. Diez-Silva, S. Suresh, J. M. Higgins, and S. R. Manalis. Measuring single-cell density. *Proceedings of the National Academy of Sciences USA*, 108(27):10992–10996, 2011.

[12] D. E. Discher. Tissue Cells Feel and Respond to the Stiffness of Their Substrate. *Science*, 310(5751):1139–1143, 2005.

[13] S. E. Cross, Y. S. Jin, J. Rao, and J. K. Gimzewski. Nanomechanical analysis of cells from cancer patients. *Nature Nanotechnology*, 2(12):780–783, 2007.

[14] Q. S. Li, G. Y. H. Lee, C. N. Ong, and C. T. Lim. Afm indentation study of breast cancer cells. *Biochemical and Biophysical Research Communications*, 374(4):609–613, 2008.

[15] B. Dorvel, B. Reddy, I. Block, P. Mathias, S. E. Clare, B. Cunningham, D. E. Bergstrom, and R. Bashir. Vapor-Phase Deposition of Monofunctional Alkoxysilanes for Sub-Nanometer-Level Biointerfacing on Silicon Oxide Surfaces. *Advanced Functional Materials*, 20(1):87–95, 2010.

[16] J. Yeom and M. A. Shannon. Detachment Lithography of Photosensitive Polymers: A Route to Fabricating Three-Dimensional Structures. *Advanced Functional Materials*, 20(2):289–295, 2010.

[17] C. Hou, W. Zuo, M. E. Moses, W. H. Woodruff, J. H. Brown, and G. B. West. Energy uptake and allocation during ontogeny. *Science*, 322(5902):736–739, 2008.

[18] R. Chotard-Ghodsnia and C. Verdier. Rheology of living materials. In *Modeling of Biological Materials*, pages 1–31. Springer, 2007.

[19] A. N. Ketene, E. M. Schmelz, P. C. Roberts, and M. Agah. The effects of cancer progression on the viscoelasticity of ovarian cell cytoskeleton structures. *Nanomedicine: Nanotechnology, Biology, and Medicine*, 8(1):93–102, 2012.

[20] V. Vadillo-Rodriguez, S. R. Schooling, and J. R. Dutcher. In Situ Characterization of Differences in the Viscoelastic Response of Individual Gram-Negative and Gram-Positive Bacterial Cells. *Journal of Bacteriology*, 191(17):5518–5525, 2009.

[21] K. E. Bremmell, A. Evans, and C. A. Prestidge. Deformation and nano-rheology of red blood cells: An AFM investigation. *Colloids And Surfaces B-Biointerfaces*, 50(1):43–48, 2006.

[22] N. E. Reticker-Flynn, D. F. B. Malta, M. M. Winslow, J. M. Lamar, M. J. Xu, G. H. Underhill, R. O. Hynes, T. E. Jacks, and S. N. Bhatia. A combinatorial extracellular matrix platform identifies cell-extracellular matrix interactions that correlate with metastasis. *Nature Communications*, 3:1122, 2012.

Chapter 8

Summary and Future Work

8.1 Dissertation Summary

The use of microelectromechanical systems (MEMS) has begun to bridge the gap between biology and engineering, and has contributed to the study of the physical properties of individual cells and other biological targets [1–4]. The work in this dissertation focused on a previously introduced MEMS resonant sensor for measuring the mass and growth rate at the single cell level [5]. However, this technology, along with other cantilever-style resonant sensors, is plagued by several limitations that inhibit applications of resonant sensors for mass measurement and analysis. These include insufficient cell capture efficiency, media perfusion for long-term growth, cell adhesion and motility, and anomalous resonant frequency measurements from soft objects. This dissertation addressed several issues hindering the progress of MEMS resonant pedestal sensors in the measurement of cellular mass and growth rate. The research focused on four main areas of interest: 1) using MEMS resonant pedestal sensors to measure physical properties of biomaterials, including the micromechanical properties of hydrogels through verification of stiffness effect on mass measurements; 2) incorporation of an on-chip microfluidic system for delivery of fluids, including growth factors, during mass measurements; 3) micro-patterning of sensor surfaces for select functionalization and passivation to enable long-term cell growth measurements; and 4) investigation of the changes in mass of normal and cancerous cells over time.

I first used the MEMS resonant pedestal sensors to measure the swelling properties of hydrogels. By incorporating hydrogel structures onto the sensor surface through a photolithographic technique, I was able to measure the mass of the hydrogels in various conditions. Mass measurements of hydrated and dehydrated structures were used to calculate swelling of the hydrogels, which is an important physical property to be considered in the design of hydrogels for various applications. I also used these hydrogel structures to investigate the influence of the surrounding fluid density on the mass measurement.

Hydrogel microstructures were also used to investigate the effects of material properties on the mass measurement with resonant sensors. Due to the nature of our measurement technique, which uses resonant sensor resonant frequency to estimate mass, the apparent mass reading is influenced by the viscoelastic behavior of soft objects. This effect has been previously described by a two-degree-of-freedom system, which was inverted to extract material properties from mass measurements. I was able to deposit soft hydrogels using electrohydrodynamic jet printing and determine their actual mass from confocal microscopy. The stiffness and viscosity extracted from these measurements agreed well with independent measurements from atomic force microscopy, and verified the accuracy of the model in predicting the system behavior.

Modifications of the sensor were made to enhance the ability to selectively capture or place cells on the sensor surface. These modifications included the addition of a backside pore and on-chip microfluidic system for delivery of flow to the sensors during the measurement. This flow is designed to improve cell capture and retention, and I characterized this improvement through simulation and microbead experiments demonstrating a two-fold capture efficiency increase. The addition of on-chip microfluidics also allows for growth media or other factors to be delivered to the captured cell during the measurement. This is especially useful in studying neurons, which require specific growth media, and I demonstrated the ability to measure the mass and growth of neurons and glial cells from a heterogeneous population with these modified sensors. This is the first example of neurons growth studied with MEMS resonant sensors.

The modified flow sensor greatly improves the capture and retention of relatively non-motile cells, such as neurons and human colon cancer (HT29); however, the ability to study highly motile cells remains challenged. I then introduced a micro-patterning technique that maximizes cell capture and holds the cells on the sensor for long-term growth measurements. In this procedure, the sensor is selectively functionalized with collagen and the rest of the chip is backfilled with pluronic, a highly effective cell and protein blocker. I showed that even motile cells are captured and held on the micro-patterned sensor platform for at least an 18-hour growth measurement. To my knowledge, this is the first report of micro-patterning for selective functionalization and passivation on fully-suspended sensors.

Finally, I used the MEMS resonant sensors, along with the developments described above, to measure the cell mass growth properties of normal and cancerous cells. I explored the differences in growth signature between benign, low metastatic, and high metastatic human breast cells. Based on preliminary findings, normal cells gain have a higher growth rate than cancerous cells, which is supported by doubling times measured through conventional bulk techniques. However, these results also suggest that a greater degree of metastatic potential in different cancer cells lines is reflected in higher growth rates. The two-degree-of-freedom system was used again to examine differences in the apparent mass ratio for each cell line and compared it with the expected values based on measured cell stiffness. This investigation indicated that the highly metastatic cancer cells had a different shape due to reduced adhesion, which is consistent with previous investigations.

8.2 Directions for Future Research

The design, implementation, and characterization of the technological developments described in this work ultimately led to the first comparison of normal and cancerous adherent cell growth rates on the single cell level. While more information can be gleaned from these measurements through an increased number of samples, many avenues for further investigations remain. The following sections describe potential future directions for coordinating growth over the cell cycle, using the microfluidic system for studying drug delivery, and further investigation to the biophysical changes occurring during the mass measurement.

8.2.1 Fluorescent Labeling for Individual Cell Analysis

The preliminary results presented in Chapter 7 demonstrate the ability of MEMS resonant sensors to identify and quantify differences in the growth rate of normal and cancerous cells. However, this data also highlights the need for improvements in the system to better allow for the analysis of individual growth profiles over the cell cycle. For instance, we might expect normal cells to exhibit different growth rates between the different cycle stages, while the disruption of cycle checkpoints in cancer may result in a more uniform growth rate over the entire cycle.

Fluorescent biomarkers, such as cycle reporters, can be used to identify stages of the cell cycle [6]. These biomarkers can be incorporated into the mass measurement and imaged through modification of the existing optical monitoring system. This addition would allow for the growth profile of each individual cell to be related to its specific cell cycle progression. Additionally, group analysis of multiple cells may include binning according to cycle stage, or individual growth curves may be aligned based on a common point in the cycle [7]. These analyses may improve cancer studies and better elucidate differences in cellular growth characteristics.

8.2.2 Effect of Chemotherapeutics on Mass Growth Rate

The ability to study mass changes throughout the cell cycle improves the ability to study cancer and the bases of metastatic potential. It also allows for the study of how cellular growth rate responds to various external stimuli, including growth factors and anti-cancer chemotherapeutics. Being able to monitor changes to growth rate during specific cell cycle stages will allow for tailoring of therapies for a wide range of applications.

These studies will be greatly aided by the on-chip microfluidic system presented in Chapter 5. We will be able to continuously deliver the fluid solution of interest to the cells on the sensor while monitoring in real time. This way the dosage can be controlled through solution concentration and total volume, and can be adjusted as necessary. Beyond cancer, applications in tissue engineering and regenerative medicine may benefit greatly from this technology as the influence of growth factors can be investigated.

8.2.3 Adhesion Sensor

Cells can interact and respond to environmental signals, such as cell adhesion like cell-to-ECM [8]. Many biological processes and cellular activities are influenced by these environmental signals. Some of the biological processes include the regulation of cell growth and differentiation. The development of an adhesion sensor can help defining events in many diseases, including cancer. Our sensor can currently sense changes in adhesion, as seen by when a cell divides, where the cell partially detaches and changes its overall contact area. It is known that the higher the degree of metastatic potential a cell has the lower adhesion characteristics.

There is much interest in understanding the triggers between cell adhesion with behavioral patterns [9–15]. Unlike current techniques for characterizing cell adhesion, which are often destructive and require manipulations [16–20], the objective would be to improve the existing sensor and develop an adhesion sensor for label-free and non-invasive technology. Working along the same line as drug studies, the platform itself will allow for drug screening of molecules to intervene with the cell adhesion process.

8.3 References

[1] R. Bashir. BioMEMS: state-of-the-art in detection, opportunities and prospects. *Advanced Drug Delivery Reviews*, 56(11):1565–1586, 2004.

[2] D. Kim, P. K. Wong, J. Park, A. Levchenko, and Y. Sun. Microengineered Platforms for Cell Mechanobiology. *Annual Review of Biomedical Engineering*, 11(1):203–233, 2009.

[3] S. Lindström and H. Andersson-Svahn. Overview of single-cell analyses: microdevices and applications. *Lab On A Chip*, 10(24):3363, 2010.

[4] J. L. Arlett, E. B. Myers, and M. L. Roukes. Comparative advantages of mechanical biosensors. *Nature Nanotechnology*, 6(4):203–215, 2011.

[5] K. Park, L. J. Millet, N. Kim, H. Li, X. Jin, G. Popescu, N. R. Aluru, K. J. Hsia, and R. Bashir. Measurement of adherent cell mass and growth. *Proceedings of the National Academy of Sciences USA*, 107(48):20691–20696, 2010.

[6] A. C. Zambon. Use of the ki67 promoter to label cell cycle entry in living cells. *Cytometry Part A*, 77(6):564–570, 2010.

[7] F. Ferrezuelo, N. Colomina, A. Palmisano, E. Gari, C. Gallego, A. Csik Csiksz-Nagy, and A. Marti. The critical size is set at a single-cell level by growth rate to attain homeostasis and adaptation. *Nature Communications*, 3:1012–11, 2012.

[8] Y. Fang. Label-free biosensors for cell biology. *International Journal of Electrochemistry*, 2011, 2011.

[9] A. Pierres, A. Benoliel, D. Touchard, and P. Bongrand. How Cells Tiptoe on Adhesive Surfaces before Sticking. *Biophysical Journal*, 94(10):4114–4122, 2008.

[10] G. C. Easty, D. M. Easty, and E. J. Ambrose. Studies of cellular adhesiveness. *Experimental Cell Research*, 19(3):539–548, 1960.

[11] N. Goel, R. D. Campbell, R. Gordon, R. Rosen, H. Martinez, and M. Ycas. Self-sorting of isotropic cells. *Journal of Theoretical Biology*, 28(3):423–468, 1970.

[12] R. D. Lovchik, F. Bianco, N. Tonna, A. Ruiz, M. Matteoli, and E. Delamarche. Overflow Microfluidic Networks for Open and Closed Cell Cultures on Chip. *Analytical Chemistry*, 82(9):3936–3942, 2010.

[13] K. D. McCarthy and L. M. Partlow. Preparation of pure neuronal and non-neuronal cultures from embryonic chick sympathetic ganglia: a new method based on both differential cell adhesiveness and the formation of homotypic neuronal aggregates. *Brain Research*, 114(3):391–414, 1976.

[14] A. S. Curtis. Timing mechanisms in the specific adhesion of cells. *Experimental Cell Research*, Suppl 8:107–122, 1961.

[15] A. Pierres, A. M. Benoliel, and P. Bongrand. Cell fitting to adhesive surfaces: a prerequisite to firm attachment and subsequent events. *Journal of European Cells and Materials*, 3:31–45, 2002.

[16] Y. Fang. Label-free cell-based assays with optical biosensors in drug discovery. *Assay and Drug Development Technologies*, 4(5):583–595, 2006.

[17] Y. Fang. Non-invasive optical biosensor for probing cell signaling. *Sensors*, 7(10):2316–2329, 2007.

[18] Y. Fang. Label-free receptor assays. *Drug Discovery Today: Technologies*, 7(1):e5–e11, 2010.

[19] J. Li, C. Thielemann, U. Reuning, and D. Johannsmann. Monitoring of integrin-mediated adhesion of human ovarian cancer cells to model protein surfaces by quartz crystal resonators: evaluation in the impedance analysis mode. *Biosensors and Bioelectronics*, 20(7):1333–1340, 2005.

[20] I. Giaever and C. R. Keese. A morphological biosensor for mammalian cells. *Nature*, 366(6455):591–592, 1993.

Appendix A

Pit Mass Pedestal Sensor Fabrication Process

1. Wafer Materials

   Wafer specification: SOI Wafer, Diameter: 100mm (or 4 inch)

   Device layer thickness: 2 μm

   BOX layer thickness: 0.3 μm

   Handle layer thickness: 500 μm

2. Define Electrode and Sensor Platform
   - (a) Initial Cleaning
     - i. Recipe: Piranha clean
     - ii. Time: 10 min
   - (b) Dry Oxidation
     - i. Equipment: Oxidation Furnace (MNTL)
     - ii. Recipe:
       - A. Thermal Oxidation/SiO_2 Deposition
       - B. Time: 20 min
       - C. Temperature: 1000 °C
       - D. Deposition Thickness: 25 nm

         Note: Place two dummy wafers front and back of the wafer, to measure the thickness of the SiO_2. To electrically insulate the device layer from the subsequent metal layers.

(c) Dehydration Bake
    i. Equipment: Hotplate
    ii. Recipe: 110 °C for 3min

(d) Spin Photoresist
    i. Equipment: Spinner
    ii. Recipe:
        A. Spin LOR-3A at 3000 rpm for 35 sec
        B. Soft-bake for 5 min at 178 °C
        C. Spin S1508 at 4000 rpm for 40 sec
        D. Soft-bake for 90 sec at 110 °C

           Note: LOR-3A and S1508 is sensitive to the trace of AZ-400K. Use glassware for CD-26 only.

(e) Photolithography of Mask No. 1
    i. Equipment: Quintel Q7000 Aligners (MNTL)
    ii. Recipe:
        A. Expose for 3.7 sec
        B. Develop with CD-26 at 1:30-2:00

(f) O_2 Plasma
    i. Equipment: O_2 Plasma
    ii. Recipe: clean for 30 sec

(g) Metal Deposition No. 1
    i. Equipment: CHA Evaporator (MNTL)
    ii. Recipe:
        A. Cr - 10nm

        B. Au - 50nm (1A/s, work around 50-60% thermal evaporation)
        C. Ni - 10nm (27%, 60mA, 0.5A/s)
        Note: Use thermal evaporation for Au for clean surface. For thin metal, start with power lower than 20%. Otherwise, metal can be over-deposited instantly.
  (h) Lift-off
    i. Equipment: Hotplate
    ii. Recipe: PG-remover at 80 °C for 1hr

3. Define etch mask for Silicon Etching
  (a) Dehydration Bake
    i. Equipment: Hotplate
    ii. Recipe: 110 °C for 3min
  (b) Spin Photoresist
    i. Equipment: Spinner
    ii. Recipe:
        A. Spin HMDS at 5500 rpm for 40 sec
        B. Spin AZ9260 at 5500 rpm for 40 sec
        C. Soft-bake for 210 sec at 110 °C
  (c) Photolithography of Mask No. 2
    i. Equipment: Quintel Q7000 Aligners (MNTL)
    ii. Recipe:
        A. Expose for 35-45 sec
        B. Develop with AZ400k:DI (1:4) for 4min
  (d) O_2 Plasma

        i. Equipment: O_2 Plasma
        ii. Recipe: clean for 30 sec
    (e) BHF Dip
        i. Equipment: Acid Bench
        ii. Recipe: BHF 1:10 for 30 sec
    (f) STS-ICP RIE
        i. Equipment: STS-ICP-RIE (MNTL)
        ii. Recipe: 6 cycle and inspect for the complete etching.

        Note: If not complete do 1 more cycle

4. Define Bond Pads
    (a) Solvent Clean
        i. Equipment: Solvent Hood
        ii. Recipe: Acetone + Methanol + DI
    (b) O_2 Plasma
        i. Equipment: O_2 Plasma
        ii. Recipe: clean for 10 min
    (c) Strip Nickel
        i. Equipment: Acid Hood
        ii. Recipe: Piranha solution for ∼30sec and rinse with DI
    (d) Dehydration Bake
        i. Equipment: Hotplate
        ii. Recipe: 110 °C for 3min
    (e) Spin Photoresist

    1. Equipment: Spinner
    2. Recipe:
        1. Spin LOR-20B at 1000rpm for 40 sec
        2. Soft-bake for 5min at 170 °C
        3. Spin AZ9260 at 5500rpm for 40 sec
        4. Soft-bake for 210 sec at 110 °C

            Note: LOR-20B can go bad quite quickly. If it doesn't coat the groves in the wafer and contain air-bubbles, use a fresh one.

(f) Photolithography of Mask No. 3

- i. Equipment: Quintel Q7000 Aligners (MNTL)
- ii. Recipe:
    - A. Expose 35-45 sec
    - B. Develop AZ400k:DI (1:4) for 4min

(g) O_2 Plasma

- i. Equipment: O_2 Plasma
- ii. Recipe: clean for 3 min

(h) Metal Deposition No. 2

- i. Equipment: CHA Evaporator (MNTL)
- ii. Recipe:
    - A. Cr - 100nm (2.5-3A/s, 23mA/25.5%)
    - B. Au - 900nm (8A/s)

      Note: Use E-beam evaporation for this step.

(i) Lift-off

- i. PG-remover at 80 °C for 1hr

   (j) Solvent clean
      i. Equipment: Solvent Hood
      ii. Recipe: Acetone + Methanol + DI

5. Prepare Etch Window
   (a) O_2 Plasma
      i. Equipment: O_2 Plasma
      ii. Recipe: clean for 5 min
   (b) Dehydration Bake
      i. Equipment: Hotplate
      ii. Recipe: 110 °C for 3min
   (c) Spin Photoresist
      i. Equipment: Spinner
      ii. Recipe:
         A. Spin HMDS at 5500 rpm for 40 sec
         B. Spin AZ9260 at 5500 rpm for 40 sec
         C. Soft-bake for 3.5 min at 110 °C
   (d) Photolithography of Mask No. 4
      i. Equipment: Quintel Q7000 Aligners (MNTL)
      ii. Recipe:
         A. Expose for 35-45 sec
         B. Develop with AZ400K:DI (1:4) for 4 min
6. Wafer Dicing
7. Device Release

(a) Etch BOX

   i. Equipment: Freon RIE (MNTL)

   ii. Recipe: Freon (CF_4) for 50 min to etch through BOX

      Cover metal pads with S1805 with swab.

      After painting, let it dry on open/ flat surface for 30min to dry.

      With a few of the chip, a opening is covered with PR again.

      Note: After RIE XeF_2 etch should be done immediately. Otherwise, native oxide will grow on exposed Si (substrate) and XeF2 etch result will be non-uniform.

(b) Protect Chip with Photoresist

   i. Equipment: cleanroom q-tips (MNTL)

   ii. Recipe: With q-tip apply S1508 PR to the bottom, the side and the alignment mark.

      Note: Wait for 30 min to dry

(c) XeF_2 Etching

   i. Equipment: XeF_2 etcher

   ii. Recipe: 2 Torr, 60 sec, 8 cycles

      Note: Exp chamber pressure should slowly increase after 20 30sec, with 0.01Torr/5sec.

(d) O_2 Plasma

   i. Equipment: O_2 Plasma

   ii. Recipe: clean for 5 min

(e) Solvent clean

   i. Equipment: Solvent Hood

   ii. Recipe: Acetone + Methanol + DI

(f) BHF Dip
  i. Equipment: Acid Bench
  ii. Recipe: BHF 10:1
    A. Time 6 min 15 sec (etching 430 nm)
    B. DI-rinse

    Note: Check through the microscope, while immersed in DI water

(g) Methanol
  i. Equipment: Solvent Hood
  ii. Recipe: Immerse in Methanol
    A. Air-Dry Methanol

    Note: Solvent Clean and BHF can be switched, if there is no atomic layer deposition (ALD) oxide.
    In this case, BHF will etch BOX from beneath the BOX layer, and keep metal layer not exposed to BHF.

(h) O_2 Plasma
  i. Equipment: O_2 Plasma
  ii. Recipe: clean for 10 min

(i) Oxide Deposition
  i. Equipment: Plasma PECVD (MNTL)
  ii. Recipe: Low deposition rate
    A. Oxide thickness: 100 nm
    B. Time: 10 min

(j) BHF Dip - Bonding pad opening
  i. Equipment: Acid Bench

        ii. Recipe: Attach PDMS protective cover (make sure it's fully attached to the device). Dip the device & PDMS cover into the BHF for 2 min. (Immerse only the bonding pad into the BHF)

            A. DI-rinse

            B. Detach PDMS

               Note: Do not recycle PDMS protective cover

    (k) Device final check (SEM)

        i. Equipment: Hitachi SEM S4800 (MNTL)

        ii. Final check

8. Chip Assembly

    (a) Attach Chip to PCB

        i. Equipment: 2 part epoxy

        ii. Recipe: place chip into designated chip area on the PCB

    (b) Wire-Bonding

        i. Equipment: Wire-bonder (King Lab MEB 53)

    (c) Solder Leads

        i. Equipment: Soldering Gun

        ii. Recipe: Heat the base first and then let solder run down

            Note: place PCB into a petri-dish leaning as not break the devices the chip

Appendix B

Flow-Through Mass Pedestal Sensor Fabrication Process

1. Wafer Materials

   Wafer specification: SOI Wafer, Diameter: 100mm (or 4 inch)

   Device layer thickness: 2 μm

   BOX layer thickness: 0.3 μm

   Handle layer thickness: 500 μm

2. Define Electrode and Sensor Platform

   (a) Initial Cleaning

      i. Recipe: Piranha clean

      ii. Time: 10 min

   (b) Dry Oxidation

      i. Equipment: Oxidation Furnace (MNTL)

      ii. Recipe: Thermal Oxidation/SiO_2 Deposition

         A. Time: 20 min

         B. Temperature: 1000 °C

         C. Deposition Thickness: 25 nm

         Note: Place two dummy wafers front and back of the wafer, to measure the thickness of the SiO_2. To electrically insulate the device layer from the subsequent metal layers.

(c) Dehydration Bake
    i. Equipment: Hotplate
    ii. Recipe: 110 °C for 3min

(d) Spin Photoresist
    i. Equipment: Spinner
    ii. Recipe: Spin LOR-3A at 3000 rpm for 35 sec
        A. Soft-bake for 5 min at 178 °C
        B. Spin S1508 at 4000 rpm for 40 sec
        C. Soft-bake for 90 sec at 110 °C

        Note: LOR-3A and S1508 is sensitive to the trace of AZ-400K. Use glassware for CD-26 only.

(e) Photolithography of Mask No. 1
    i. Equipment: Quintel Q7000 Aligners (MNTL)
    ii. Recipe: Expose for 3.7 sec
        A. Develop with CD-26 at 1:30-2:00

(f) O_2 Plasma
    i. Equipment: O_2 Plasma
    ii. Recipe: clean for 30 sec

(g) Metal Deposition No. 1
    i. Equipment: CHA Evaporator (MNTL)
    ii. Recipe:
        A. Cr - 10nm
        B. Au - 50nm (1A/s, work around 50-60% thermal evaporation)
        C. Ni - 10nm (27%, 60mA, 0.5A/s)

        Note: Use thermal evaporation for Au for clean surface. For

thin metal, start with power lower than 20%. Otherwise, metal can be over-deposited instantly.

(h) Lift-off

   i. PG-remover at 80 °C for 1hr

3. Define etch mask for Silicon Etching

   (a) Dehydration Bake

      i. Equipment: Hotplate

      ii. Recipe: 110 °C for 3min

   (b) Spin Photoresist

      i. Equipment: Spinner

      ii. Recipe:

         A. Spin HMDS at 5500 rpm for 40 sec

         B. Spin AZ9260 at 5500 rpm for 40 sec

         C. Soft-bake for 210 sec at 110 °C

   (c) Photolithography of Mask No. 2

      i. Equipment: Quintel Q7000 Aligners (MNTL)

      ii. Recipe:

         A. Expose for 35-45 sec

         B. Develop with AZ400k:DI (1:4) for 4min

   (d) O_2 Plasma

      i. Equipment: O_2 Plasma

      ii. Recipe: clean for 30 sec

   (e) BHF Dip

        i. Equipment: Acid Bench
        ii. Recipe: BHF 1:10
            A. Time: 30 sec
    (f) STS-ICP RIE
        i. Equipment: STS-ICP-RIE (MNTL)
        ii. Recipe: 6 cycle and inspect for the complete etching.

        Note: If not complete do 1 more cycle

4. Define Bond Pads
    (a) Solvent Clean
        i. Equipment: Solvent Hood
        ii. Recipe: Acetone + Methanol + DI
    (b) O_2 Plasma
        i. Equipment: O_2 Plasma
        ii. Recipe: clean for 10 min
    (c) Strip Nickel
        i. Equipment: Acid Hood
        ii. Recipe: Piranha solution for ∼30sec
        iii. Rinse with DI
    (d) Dehydration Bake
        i. Equipment: Hotplate
        ii. Recipe: 110 °C for 3min
    (e) Spin Photoresist
        i. Equipment: Spinner

    ii. Recipe: Spin LOR-20B at 1000rpm for 40 sec
    iii. Soft-bake for 5min at 170 °C
    iv. Spin AZ9260 at 5500rpm for 40 sec
    v. Soft-bake for 210 sec at 110 °C

    Note: LOR-20B can go bad quite quickly. If it doesn't coat the groves in the wafer and contain air-bubbles, use a fresh one.

(f) Photolithography of Mask No. 3
    i. Equipment: Quintel Q7000 Aligners (MNTL)
    ii. Recipe: Expose 35-45 sec
    iii. Develop AZ400k:DI (1:4) for 4min

(g) O_2 Plasma
    i. Equipment: O_2 Plasma
    ii. Recipe: clean for 3 min

(h) Metal Deposition No. 2
    i. Equipment: CHA Evaporator (MNTL)
    ii. Recipe: Cr - 100nm (2.5-3A/s, 23mA/25.5%)
    iii. Au - 900nm (8A/s)

    Note: Use thermal evaporation for Au for clean surface. For thin metal, start with power lower than 20%. Otherwise, metal can be over-deposited instantly.

(i) Lift-off
    i. PG-remover at 80 °C for 1hr

(j) Solvent clean
    i. Equipment: Solvent Hood

    ii. Recipe: Acetone + Methanol + DI

5. Device Release
   (a) Solvent clean
      i. Equipment: Solvent Hood
      ii. Recipe: Acetone + Methanol + DI
   (b) Apply Thick Photoresist (PR) to Topside
      i. Equipment: Spinner (MMS)
      ii. Recipe: dehydration bake
      iii. Spin Shipley 1827 at 3000rpm for 45sec (acceleration 300rpm/sec)
      iv. Softbake: hotplate 120°C for 1.5 min without Al ring, or 2 min with Al ring
      v. Thickness: ~3 μm
   (c) Hard Bake
      i. Equipment: Hot Plate 3.2.5
      ii. Recipe: 110 °C for 10 min
   (d) BOE Dip
      i. Equipment: Acid Bench (MMS)
      ii. Recipe: BOE
      iii. Time: 10 sec, until oxide on the back side is fully removed
   (e) Apply Thick Photoresist (PR) to Bottomside
      i. Equipment: Spinner (MMS)
      ii. Recipe: dehydration bake
      iii. Spin NR5-8000 at 1000rpm for 40sec (acceleration 200rpm/sec)
      iv. Softbake: 150°C for 6min

   v. Thickness: $\sim 17\ \mu$m

      Note: cover the hotplate with aluminum foil to avoid leaving photoresist residue on the hotplate. Cool down on Alphawipe before exposed in EV420

(f) Photolithography of Mask No. 4 (Backside Openings)

   i. Equipment: EV420 (MMS)
   ii. Recipe: Exposure
   iii. Hard Contact Mode or proximity mode (50um of separation)
   iv. Time: 30 sec
   v. Post exposure bake: 100 °C for 2min
   vi. Development: RD-6, around 70 sec
   vii. Rinse with DI Water and dry w/ N-gun

      Note: use default backside alignment lens

(g) Hard Bake

   i. Equipment: Hot Plate (covered with Al foil)
   ii. Recipe: 120 °C for 10 min

(h) Apply Thick Photoresist (PR) to Topside of Carrier Wafer

   i. Equipment: Spinner (MMS)
   ii. Recipe: dehydration bake
   iii. Spin NR5-8000 at 1000rpm for 40sec (acceleration 200rpm/sec)

(i) Attach Wafer (or single device) to Carrier Wafer

   i. Equipment: By Hand
   ii. Recipe: N/A

(j) Hard Bake

   i. Equipment: Hot Plate (MMS)
   ii. Recipe: 120 °C for 10 min, 140 °C for 25 min directly on hotplate

(k) Backside Silicon Etch
   i. Equipment: ICP-DRIE (MMS)
   ii. Recipe: Bosch-1
   iii. Estimated Number of Cycles: 800

   Note: you will see the cantilever structure from the etched trench, the 1 μm um thick box SiO_2 layer is transparent

(l) Soak to Separate Wafers
   i. Equipment: Wet Bench
   ii. Recipe: Photoresist Stripper 1165 at 80 °C
   iii. Time: overnight ($\sim$8 hours)

(m) O_2 Plasma
   i. Equipment: O_2 Plasma
   ii. Recipe: clean for 10 min

   Note: Otherwise, a thin film will appear in the following ACE

(n) Solvent clean
   i. Equipment: Solvent Hood
   ii. Recipe: Acetone + Methanol + DI

(o) BHF Dip
   i. Equipment: Acid Bench
   ii. Recipe: BHF 10:1
   iii. Time: 6 min 15 sec (etching 430nm)
   iv. DI-rinse

   Note: Check through the microscope, while immersed in DI water.

(p) Methanol

   i. Equipment: Solvent Hood
   ii. Recipe: Immerse in Methanol
   iii. Air-dry Methanol

   Note: Solvent clean and BHF can be switched, if there is no atomic layer deposition (ALD) oxide & Al_2O_3 on the surface.

(q) O_2 Plasma

   i. Equipment: O_2 Plasma
   ii. Recipe: clean for 10 min

(r) Oxide Deposition

   i. Equipment: Plasma PECVD (MNTL)
   ii. Recipe: Low deposition rate
   iii. Oxide thickness: 100 nm
   iv. Time: 10 min

(s) BHF Dip - Bonding pad opening

   i. Equipment: Acid Bench
   ii. Recipe: Attach PDMS protective cover (make sure it's fully attached to the device). Dip the device & PDMS cover into the BHF for 2 min. (Immerse only the bonding pad into the BHF)
   iii. DI-rinse
   iv. Detach PDMS

   Note: Do not recycle PDMS protective cover

(t) Device final check (SEM)

   i. Equipment: Hitachi SEM S4800 (MNTL)

    - ii. Recipe: N/A
    - iii. Final check

6. Chip Assembly
    - (a) Attach Chip to PCB
        - i. Equipment: 2 part epoxy
        - ii. Recipe: place chip into designated chip area on the PCB
    - (b) Wire-Bonding
        - i. Equipment: Wire-bonder (King Lab MEB 53)
    - (c) Solder Leads
        - i. Equipment: Soldering Gun
        - ii. Recipe: Heat the base first and then let solder run down

          Note: place PCB into a petri-dish leaning as not break the devices the chip

Appendix C

Passivation Fabrication Process

1. O_2 Plasma
   (a) Equipment: O_2 Plasma
   (b) Recipe: clean for 10 min
2. HMDS Vapor Deposition
   (a) Equipment: Oven
   (b) Recipe:
      i. Place substrates into a jar and pipette 250 μL of HMDS around the edge depression.
      ii. Seal Jar, but do not over tighten.
      iii. Time: 1 hour
      iv. Temperature: 80 °C
3. Solvent Clean
   (a) Equipment: Solvent Hood
   (b) Recipe: Rinse with Acetone, Methanol, DI Water, and N_2 Dry
4. Dehydration Bake
   (a) Equipment: Hotplate

    (b) Recipe: 110 °C for 3min

5. Transfer Print Photoresist
    (a) Equipment: Spinner and PDMS Puck
    (b) Recipe:
        i. Spin AZ9260 at 4000 rpm for 40 sec
        ii. Soft-bake for 2 min at 50 °C
        iii. Stamp PDMS on Chip with rolling motion to minimize air bubbles
        iv. Soft-bake for 2 min at 50 °C
        v. Place on Aluminium block that was cooled in 4 °C fridge for 1 min
        vi. Peel PDMS off the Chip
        vii. Soft-bake Chip for 3 min at 50 °C slowly ramp to 95 °C and hold for 20 min
6. Photolithography of Mask
    (a) Equipment: Karl Suss - 365 nm Aligner (MNTL)
    (b) Recipe:
        i. Expose for 48 sec ($300mJ/cm^2$)
        ii. Develop with AZ 400K:DI (1:4) for 3:30
7. O_2 Plasma
    (a) Equipment: O_2 Plasma
    (b) Recipe: clean for 10 min
8. Collagen Deposition
    (a) Equipment: Incubator
    (b) Recipe:

        i. Deposit collagen type I with 0.1mg/mL in 1xPBS solution for 60 min
        ii. Rinse with WI water and N_2 dry

9. Collagen Lift-off
    (a) Recipe:
        i. Soak in Acetone for 1hr, chips must be flipped upside down and gentle agitation
        ii. Rinse with Ethanol, DI Water, and N_2 dry
10. Epoxy Chip/Wirebonding
    (a) Epoxy chip to PCB
    (b) Wirebond at room temperature, use high Force, Power, and Time settings
11. Pluronic Depostion
    (a) Recipe:
        i. Depositon Pluronic with 1% solution in 1xPBS solution for 120 min
        ii. Rinse with 1xPBS